Element-Selective Ultrafast Magnetization Dynamics with a Tabletop Light Source

by

Chan La-o-vorakiat

B.Sc., Mahidol University, Bangkok, Thailand 2006

A thesis submitted to the

Faculty of the Graduate School of the

University of Colorado in partial fulfillment

of the requirements for the degree of

Doctor of Philosophy

Department of Physics

2011

This thesis entitled:
Element-Selective Ultrafast Magnetization Dynamics with a Tabletop Light Source
written by Chan La-o-vorakiat
has been approved for the Department of Physics

Henry C. Kapteyn

Margaret M. Murnane

Date

The final copy of this thesis has been examined by the signatories, and we find that both the content and the form meet acceptable presentation standards of scholarly work in the above mentioned discipline.

La-o-vorakiat, Chan (Ph.D., Physics)

Element-Selective Ultrafast Magnetization Dynamics with a Tabletop Light Source

Thesis directed by Prof. Henry C. Kapteyn and Prof. Margaret M. Murnane

Next-generation hard-disk drives will require smaller magnetic bits and faster magnetization switching; hence, better understanding of nanoscale magnetic material is one of the key factors in developing of these devices. Here, I present the first ultrafast magnetization dynamics studies by use of extreme ultraviolet radiation from a tabletop high-harmonic generation source. This new probing technique offers three advantages over conventional ones: ultrafast time resolution, element selectivity, and the tabletop size.

I report three experiments showing that high harmonics are a powerful tool for probing magnetization in magnetic materials. First, our group measures simultaneously the magnetizations of Ni and Fe in Permalloy using the transverse magneto-optical Kerr effect. Second, we study laser-induced demagnetization dynamics in two ferromagnetic alloys: Permalloy and Permalloy-Cu. Contrary to a common expectation that the dynamics in strong exchange-coupled alloys would be identical, we discover that the magnetization of Fe decays earlier than that of Ni during the first 60 fs. To explain this delay, we propose a simple model incorporating a finite exchange-time factor into the magnetization rate equations. Finally, to confirm the observed sequence of dynamics in alloys, we conduct the magnetization study of elemental Fe and Ni with identical experimental conditions. The results indicate that the order of demagnetizations in the elemental forms is the same as that in Permalloy: Fe demagnetizes faster than Ni does.

To Aim

Acknowledgements

I have a great fun in the graduate school because of the people around me. I would like to thank my advisors, Margaret Murnane and Henry Kapteyn, for granting me an opportunity to work in their research group. Tom Silva is virtually my third advisor who explained us everything from how to built a magnet to the importance of the error bars. I would like to thank all KM group members: Stefan Mathias, Kathy Hoogeboom-Pot, Luis Miaja-Avila, Carson Teale, Tory Carr, Tenio and Dimitar Popmintchev, Bosheng Zhang, Ethan Townsend, Daisy Raymondson, Ariel Paul, Piotr Matyba, Paul Arpin, Michael Garity, Susannah Brown, Predrag Ranitovic, Craig Hogle, Vandana Sharma, Ellen Keister, Dan Hickstein, Chengyuan Ding, Robin Lock, Xibin Zhou, Alon Bahabad, Betsey Hall, Dominique Gaudyn, Rachael and Matt Tearls, and Kim Reid. Special acknowledgements to Mark Siemens and Richard Sandberg for teaching me everything during my first few years; to Quan Zhang, Qing Li, Ming-chang Chen, and Jing Yin for their friendship; to Emrah Turgut for his bravery to continue the project; to Matt Seaberg and Dan Adams for their help with the laser and Dan's continuous attempts to make us laugh; to Damiano Nardi for his Carbonara recipe; to John and Kate Hoversten, Joseph Mccalley, Kyle and Lisa Lampe, who are always my great friends; to Hans Nembach, Justin Shaw, Martin Aeschlimann, Patrik Grystol, Roman Adams, Claus Schneider, and Erik Hosler for such a fun collaboration.

Finally, the greatest acknowledgment and love should go to my wife, Aimon Tongpenyai, for everything she has done.

Contents

Chapter

Tables

Table

Figures

Figure

Chapter 1

Introduction

1.1 Hard-Disk-Drive Technologies

Former Google chief executive Eric Schmidt estimated that every two days, we create five exabytes of data (1 EB = 10^{12} MB). This is as much information as humankind created from the dawn of civilization until 2003 [22]. If we stored all of this data in floppy disks, the whole United States would be covered with floppy disks within nine years. Clearly, we need more efficient information storage in smaller devices at cheaper prices. This motivation, together with the competition with other storage technologies such as solid state drives, is pushing magnetic-data-storage industries to build hard-disk drives that are faster, denser, and cheaper [23].

The advancement in hard-disk technologies can be quantitatively described in terms of areal density. Areal density is defined as the number of bits in one square inch of hard-drive media (Figure 1.1). In 1956, it was on the order of kbit/in^2, which is now approaching 1 Tbits/in^2. This nine orders-of-magnitude improvement is due to the exponential growth of areal density, which now doubles every two years. The trend is analogous to Moore's law, which predicts that the number of transistors in integrated circuits has doubled every year [24].

To maintain this growth rate, new technologies have been incorporated into hard-disk drives. For example, disk-read heads, which are data readers from storage media, were fabricated from ferrite material, making them too large and insensitive to the

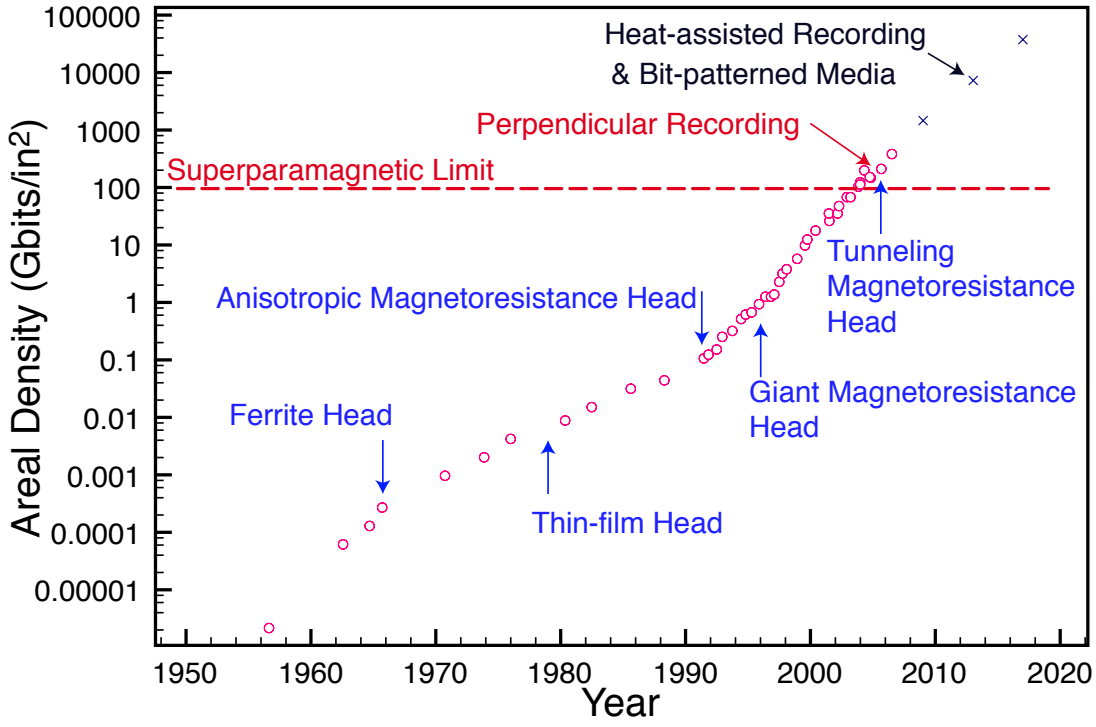

Figure 1.1: Areal density (red circles) has doubled every two years with the introduction of new technologies into hard drives. Read-head technologies (blue) have moved from ferrite heads to thin-film heads in 1980 and to magnetoresistance heads after 1990. The superparamagnetic limit (red dashed line) was once considered as the maximum areal density for the in-plane recording employed in the past. This limit was overcome by perpendicular recording media in 2005. Heat-assisted recording and bit-patterned media have been proposed to continue the growth of areal density (black crosses). Reproduced from References [1, 2, 3].

small magnetic fields required for today's data reading. In 1990, industries turned to magnetoresistance-read heads, which are more compact and sensitive. From then on, the areal density grew at higher rate. The trend continues today as industries shift to giant- and tunneling-magnetoresistance heads (Figure 1.1).

In addition to the advancement in read heads, a breakthrough has also occurred in storage media [25]. As the areal density increases, the size of and the spacing between bits shrink down. As a result, thermal fluctuations can more easily cause data loss. This effect, known as the superparamagnetic effect, limits the maximum areal density to 36 Gbits/in^2 [26, 27] for longitudinal storage media where magnetization is in the plane of the disk surface. To overcome this limit, industries now design hard-disk drives in which the bit magnetization is perpendicular to the media. Industries introduced this perpendicular recording into commercial hard drives in 2005 [28, 29, 30]. This relatively new technology alone should allow the areal density to reach above 1 Tbits/in^2 (Figure 1.1).

To improve the areal density further in the future, industry is developing two leading candidates for hard-disk technologies: (1) bit-patterned media and (2) head-assisted magnetic recording (Figure 1.2). Bit-prepatterned media enhance stability of data storage at high bit density. Unlike conventional recording where each bit occupies several naturally formed grains on the storage material, bit-patterned media are capable of storing one bit on a prepatterned island (of the size as small as tens nanometers) fabricated by nanolithography techniques. The orderliness reduces the superparamagnetic effect on bits, resulting in more magnetically stable hard drives.

However, magnetically stable materials have a drawback; the data writing process requires the stronger switching magnetic field beyond the capability of conventional write heads. Head-assisted magnetic recording solves this problem by using the laser to heat up magnetic bits, so they switch more easily in response to the smaller magnetic field [31, 32, 33, 34]. The combination of bit-patterned media and head-assisted magnetic

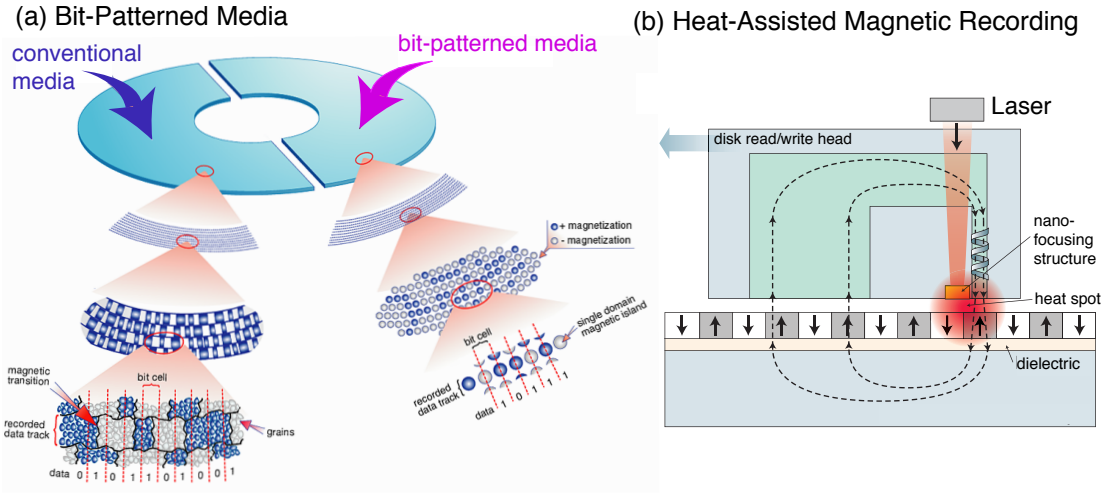

Figure 1.2: Two candidates for future hard-disk technologies. (a) Bit-pattened media require prepatterned pillars of magnetic materials as storage bits (magenta arrow); In contrast, conventional recording bits are made of naturally formed grains (blue arrow). (b) Heat-assisted magnetic recording incorporates lasers into hard-disk heads. Lasers are used to heat up the media, reducing the switching magnetic field to be able to write information with thin-film recording transducers in hard-disk heads. Figure from References [4, 5].

recording may lead to an areal density of 300 Tbits/in^2, which is two orders of magnitude larger than the areal density of the current commercial hard drives [5].

However, before we incorporate bit-patterned media and head-assisted magnetic recording into hard drives, we need to understand more about the physics governing these new technologies. We need an experimental tool that allows us to probe materials with both nanoscale spatial resolution and femtosecond time resolution. The spatial-resolution requirement is set by the size of pillars in bit-patterned media. The time-resolution requirement is fundamental to understand the relationship between light and magnetism that governs head-assisted magnetic recording. Therefore, we need (1) light sources ranging in the extreme ultraviolet or soft x-ray range to probe magnetic nanostructures and (2) short pulses to explore the dynamics on the femtosecond time scale.

1.2 Probing Nanostructures with Extreme Ultraviolet and Soft X-rays

To probe nanoscale magnetic structures, we require light at short wavelengths. The smallest detectable feature (i.e., spatial resolution) is related to wavelength (λ), as

$$\Delta r = \frac{0.5\lambda}{NA}, \tag{1.1}$$

where Δr is spatial resolution, NA is the numerical aperture. It describes the size of the imaging optics (e.g., a lens) used to measure the emitted light from an object. Since the visible range is 400 to 800 nm and the maxmium numerical aperture is close to unity, optical microscopy can only detect objects down to approximately 200 nm in size. This spatial resolution is already larger than the bit size used in commercial hard drives since 2000 (Figure 1.1), the probing wavelength must be shortened beyond the visible range to the extreme ultraviolet and soft x-ray regions.

Extreme ultraviolet light ranges from 30 to 250 eV, and soft x-rays range from

250 eV to several keV. With extreme ultraviolet or soft x-rays, the spatial resolution can be reduced to below a hundred nanometers, enabling such applications as microscopy [35] and lithography [36]. The spatial resolution is small enough to detect structures in hard-drive media up to an areal density of 10 Tbits/in^2 (extreme ultraviolet) and 1000 Tbits/in^2 (soft x-rays) (Figure 1.3).

In additional to the advantage of spatial resolution, many elemental absorption edges exist in the extreme ultraviolet and soft x-ray regions. Across these edges, the absorption of materials drastically changes by a slightly shift of light photon energies because of the excitation of an inner-shell electron to valence levels. The locations of absorption edges are element specific because the atomic energy levels are unique for each element. Such element selectivity is very useful for many scientific applications [37, 38] including magnetism. By taking advantage of the unique absorption, we can probe magnetization in an element-specific manner. The absorption edges of naturally occurring ferromagnetic elements, e.g., iron, cobalt, and nickel, are located in the extreme ultraviolet and soft x-ray regions. The extreme ultraviolet region contains M-shell absorption edges where core 3p electrons are excited to the valence 3d levels. The soft x-ray region contains L-shell absorption edges where deeper core 2p electrons are excited to the same valence 3d levels.

1.3 Probing Laser-Induced Magnetization Dynamics with Short Pulses

In addition, we will require short-pulsed light in the range of extreme ultraviolet or soft x-ray to understand the dynamical behaviors in materials of future hard-disk technologies. Femtosecond pulses are needed because many important magnetization dynamics occur on the femtosecond time scale (Figure 1.4).

Precession dynamics at nanosecond time scales were thought to be the fastest magnetic phenomena. Since 1996, however, the developments of short-pulsed laser tech-

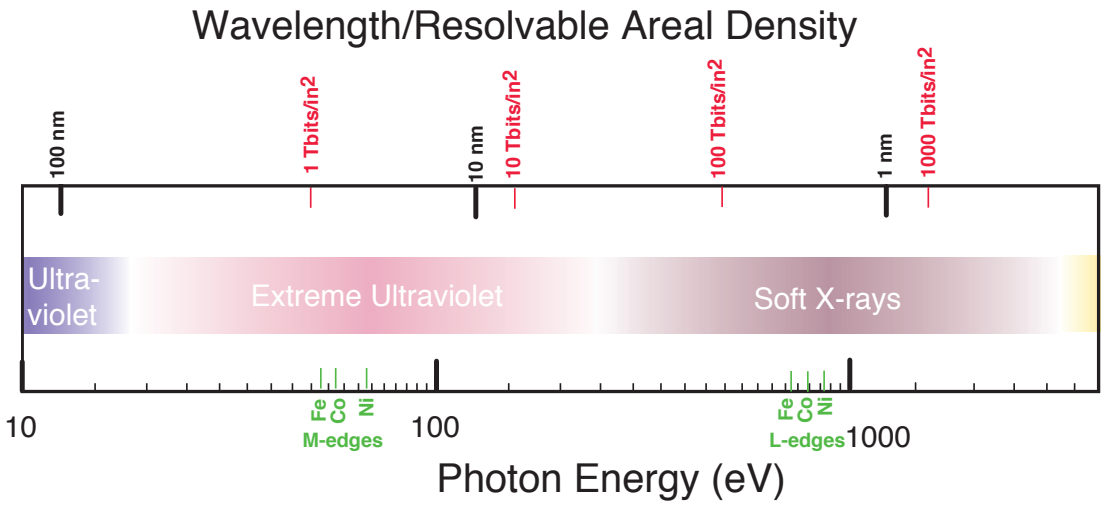

Figure 1.3: Location of extreme ultraviolet and soft x-rays in the electromagnetic spectrum. Because of the short wavelengths (top axis), extreme ultraviolet and soft x-rays provide the spatial resolution needed to study nanoscale magnetic structures. The required wavelengths for probing features in data-storage media at different areal densities (red) are estimated. Additionally, the absorption edges of Fe, Co, and Ni (green) are in the extreme ultraviolet (M-edges) and in soft x-ray region (L-edges). M-edges correspond to he photon energy required to excite a 3p electron into 3d levels. L-edges correspond to the photon energy required to excite a 2p electron into 3d levels.

nologies has enabled studies of dynamics at time scales down to femtoseconds. For example, Beaurepaire et al., discovered that demagnetization by a short-and-intense laser pulse occurs in a few hundreds of femtoseconds [9]. Recently, Bigot et al., discovered that coherent coupling of light and magnetization occurs in attoseconds [10].

Magnetization dynamics in the femtosecond range involve interactions between light and magnetization. In addition to the direct application for heat-assisted magnetic recording, these dynamics are also important for basic physics for three reasons. First, magnetization dynamics at ultrafast time scales are directly involved with the interaction among quantum particles such as laser photons, electrons, and phonons. Second, the time scales of ultrafast dynamics fall into the range where the characteristic times of spin-orbit and exchange interactions, the fundamental magnetic interactions, are both involved [11] (Figure 1.5). It is challenging to explain the observed dynamical behavior with our current theoretical understanding. Third, the first demonstration of ultrafast magnetization dynamics in 1996 [9] brought much attention to understanding these dynamics. Curiosity and new ideas opened up many new research areas such as all-optical switching of magnetization [39], laser-induced ferromagnetic resonance [40], time-resolved x-ray magnetism [41], and terahertz emission during demagnetization [42].

1.4 Extreme Ultraviolet Pulses from High-harmonic Generation

Since the first demonstration of ultrafast magnetization dynamics in 1996 [9], ultrafast lasers have been used to perform various pump-probe studies. Magnetization has been probed via the Kerr effect, the Faraday effect, and surface second-harmonic generation. However, these techniques do not provide element-specific information since the visible photon energy of laser is not large enough to reach any magnetic absorption edges. Extreme ultraviolet or soft x-ray light is required for element-selective probes of magnetic materials.

The most common sources for extreme ultraviolet and soft x-ray light are syn-

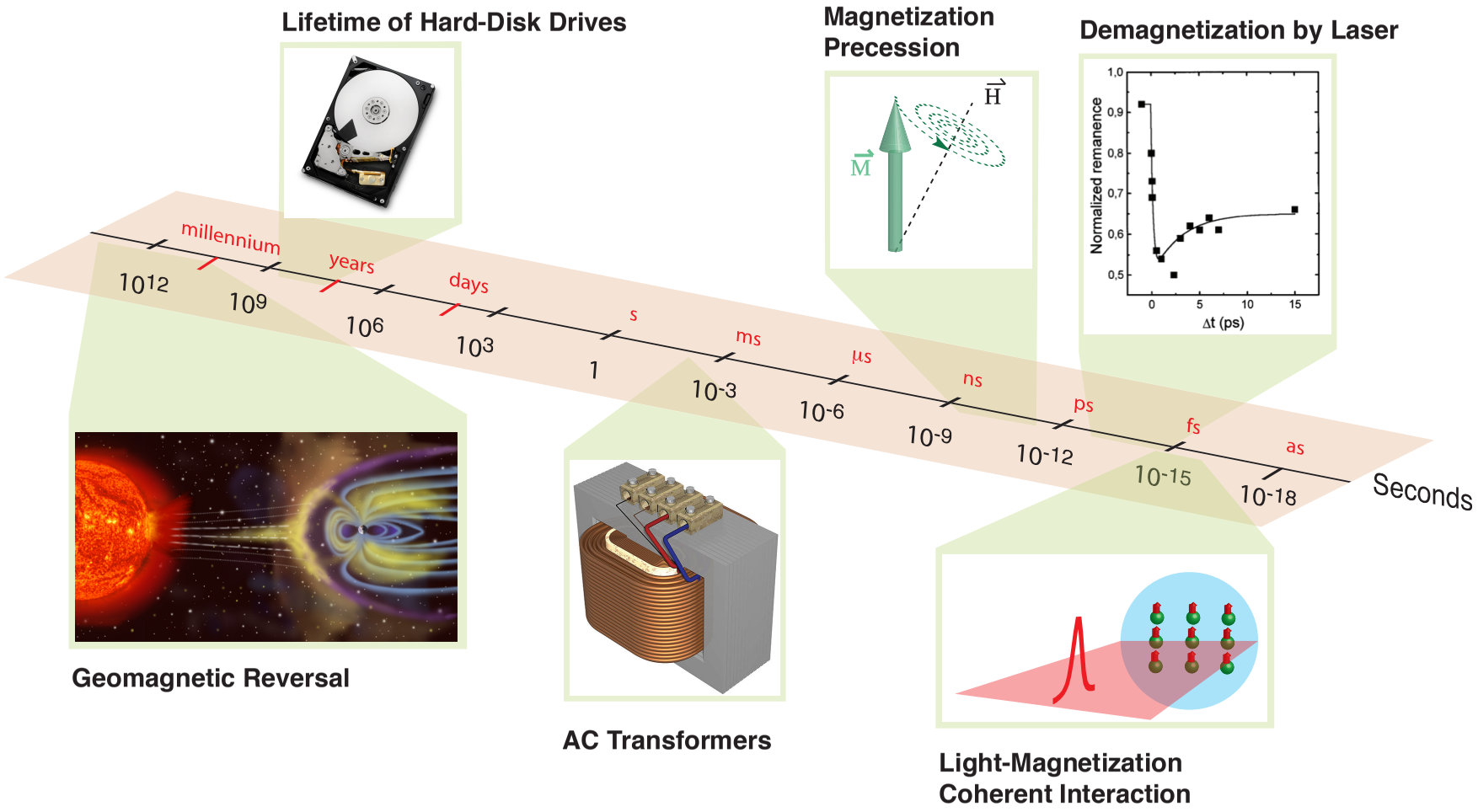

Figure 1.4: Important magnetic time scales from millennia to attoseconds. Figures from References [6, 7, 8, 9, 10]. The time scales are from Reference [11].

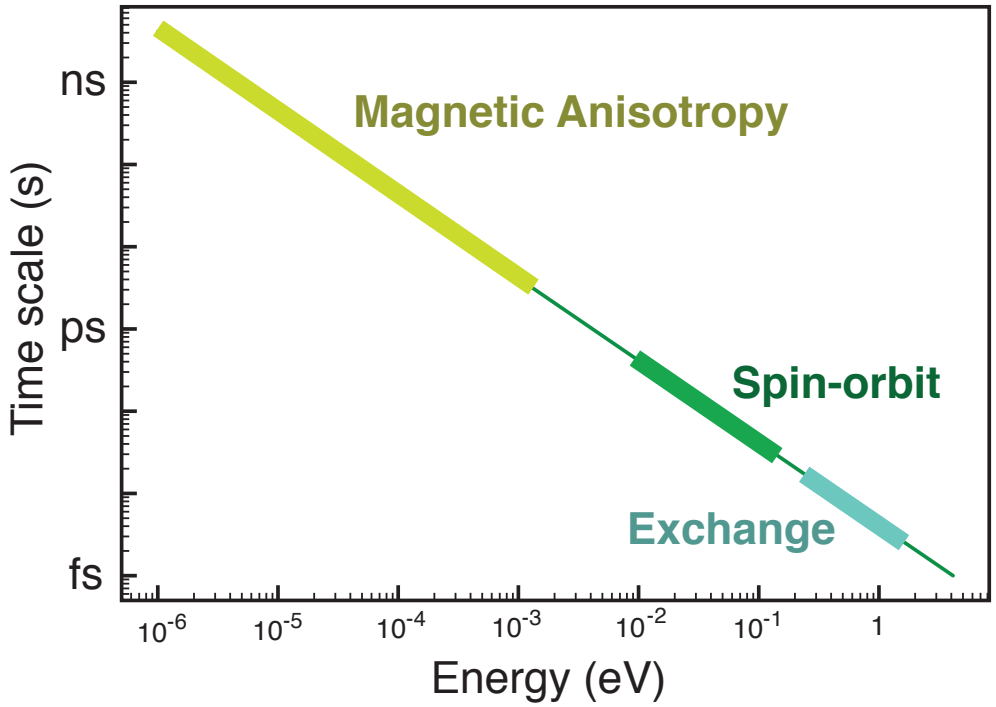

Figure 1.5: Fundamental magnetic time scales and energies of magnetic interactions, exchange, spin-orbit, and anisotropy, of iron, cobalt, and nickel estimated from the time-energy product, $E \times t = h$. Reproduced from Reference [11]

chrotrons and free-electron lasers. Both of these sources meet the nanometer-wavelength and femtosecond-pulse-duration requirements for element-selective studies of ultrafast magnetization dynamics. Synchrotron radiation is generated by accelerating relativistic electron bunches in a circular path. The spectra of light emitted from synchrotrons cover from infrared to x-ray range. The photon flux from synchrotron radiation is often large. However, the pulse duration of synchrotron radiation is dependent on the size of electron bunches, which range from a few hundred picoseconds to nanoseconds. This pulse duration is too broad to capture ultrafast magnetization dynamics. To generate shorter light pulses for ultrafast studies, short bunches of electrons are 'sliced' out from broad electron bunches by femtosecond laser pulses [43, 44]. The synchrotron radiation emitted from these shorter bunches yields short pulses. The soft x-ray pulse duration from this slicing technique is approximately 100 fs [45], which is barely short enough to probe ultrafast magnetization dynamics.

Magnetization dynamics studies can also use free-electron lasers, which provide bright short-pulsed light across the electromagnetic spectrum (infrared [46], ultraviolet [47], soft x-ray [48], and x-ray [49]). The photon flux from free-electron lasers is, in general, very intense, enabling collection of enough statistics with one probe pulse (single-shot experiment, e.g Reference [50]). A drawback of these large-scale light sources, such as synchrotrons and free-electron lasers, is the limited uses accessibility because of the cost ($\sim$ \$1B [51]) and scale of the facilities ($\sim$ a few km [52]).

More accessible light sources for extreme ultraviolet and soft x-rays are based on high-harmonic generation. These light source are referred as 'tabletop' because they fit on one optical table and do not require any special infrastructure. Using laser pulses from a standard laser-amplifier system, high-harmonic generation routinely produces photons in the extreme ultraviolet region with a useful photon flux (10^{12} photons per second). In the time domain, the pulse duration of the high harmonics is very short, ranging from a few femtoseconds to attoseconds. With the two advantages of short

wavelength and short pulse duration, high harmonics are suitable for both probing ultrafast dynamics and for microscopy at short length scales.

In the past, many research groups worldwide applied high harmonics to atomic and molecular spectroscopy [53, 54, 55], condensed matter research [56, 57], heat transportation studies [58], and microscopy [59, 60, 61]. Although high harmonics are regarded as a plausible tool for studying ultrafast magnetization dynamics [62], no one has successfully demonstrated this application until 2009 by our group [63]. We employ high harmonics to study magnetization dynamics by combining ultrafast time resolution with element selectivity into one tabletop experiment. This thesis describes this work in detail.

1.5 Outline of the Thesis

This thesis consists of two parts. The first part contains reviews of related past work (Chapter 2–4), and the second part presents our experiments (Chapter 5–9). In Chapter 2, I review the basic physics of high-harmonic generation using a semiclassical three-step model. In Chapter 3, I discuss magneto-optical effects in the extreme ultraviolet range and calculate contrast levels from various magneto-optical effects. One of these effects, the transverse Kerr effect, is used to probe magnetization for subsequent experiments reported in this thesis. In Chapter 4, I review past work on laser-induced ultrafast demagnetization dynamics.

In Chapter 5, I give a detailed explanation of our experimental setup and data-acquisition technique. In Chapter 6, I present experimental results using the high-harmonic probe to measure static magnetizations. I show that magnetic contrast up to 30% originates from the transverse magneto-optical Kerr effect at the M edges of iron and nickel. The chapter also covers the wavelength tunability and stability of our high-harmonic generation source. In Chapter 7, I present time-resolved magnetization-dynamics studies of ferromagnetic alloys, i.e., Permalloy and Permalloy–copper. Sur-

prisingly, the magnetization of iron decays faster than nickel during the first tens of femtoseconds, even in the presence of strong exchange coupling between iron and nickel. A phenomenological model based on this finite exchange time is introduced. In Chapter 8, I compare the demagnetization dynamics of elemental iron and nickel. Our results are in agreement with the dynamics observed in alloys. In addition, the measured fluence-dependent magnetization dynamics in nickel are in agreement with past experimental results measured by optical lasers and theoretical predictions. In Chapter 9, I conclude the thesis with a discussion of future prospects for magnetic-imaging experiments.

Chapter 2

High-hamonic Generation

2.1 Introduction

Later on in this thesis, I will present experimental results on magnetization dynamics studies with short extreme-ultraviolet pulses from high-harmonic generation. With this method, the photon energies of lasers are multiplied by a factor of 40, from infrared to extreme ultraviolet. Recently, by use of an intense mid-infrared laser, our group demonstrated that high harmonics are now in the soft x-ray region by up-converting the photon energy by 5000 [64]. No matter how high the orders of harmonics are, the basic physics to describe high-harmonic generation is still the same. In this chapter, I cover the mechanism behind high-harmonic generation using a simple approach based on classical mechanics. The model answers many important questions about properties of high harmonics, such as why high-harmonic generation can produce an isolate attosecond pulse and why high-harmonic spectra are discrete combs of photon energies. But before introducing the model, I will discuss the most important ingredient for high-harmonic generation: intense laser light pulses.

2.2 Ultrashort Pules and Nonlinear Optics

To be involved with any nonlinear optical phenomena, we need an intense source of electromagnetic field. Indeed, the first demonstration of a laser in 1960 [65] was followed immediatly by the discovery of nonlinear optics in 1961 [66, 67]. Later on, laser

technologies push nonlinear optics even further by providing short light pulses. With light pulses, higher intensity levels can be temporarily reached as the pulse duration of the laser pulses are generally very short, in the range of a few tens of femtoseconds. To visualize the number, our standard laser-amplifier system produces 2.25 mJ of energy per light pulse, which sounds weak; but since all of the energy concentrates in an infinitesimal burst of a laser pulse (30 fs), the peak power is enormous. The peak power is about 75 GW which is in the same range of the power consumption by American televisions during a Super Bowl game (57 GW). If a lens focuses this laser pulse to a moderate size (100 μm diameter), the peak intensity is elevated to $9.5 \times 10^{22} \frac{W}{cm^2}$, corresponding to the **peak** electric field of $8.5 \times 10^{10} \frac{V}{m}$. This peak electric field is close to the electric field inside an atom estimated from $E = \frac{1}{4\pi\epsilon_0} \frac{e}{a_0^2} = 5.1 \times 10^{11} \frac{V}{m}$, where e is the fundamental electronic change, ϵ_0 is the permittivity in vacuum, and a_0 is the Bohr radius.

If this laser electric field shines on any materials, atoms will react to light in different ways. At this extreme condition, the standard approximation for the interaction between light and matter does not hold any longer. And the response of polarization (P) could be written as a Taylor series of function to the electric field (E) [68],

$$P = \epsilon_0(\chi^{(1)}E + \chi^{(2)}E^2 + \chi^{(3)}E^3 + ...) \tag{2.1}$$

where $\chi^{(i)}$ are the i-th order of susceptibility. When the electric field is weak, only the first order of the expansion is a good approximation since the higher-order susceptibilities are typically small, and light is in the regime of linear optics. However, with the large amount of peak electric field in femtosecond-laser pulses, the higher order terms become significant resulting in nonlinear optical phenomena. For example, second-harmonic generation originates from the second-order susceptibility tensor, $\chi^{(2)}$, which is in the order of $10^{-12} \frac{m}{V}$ for solids [69]. The contribution to the polarization,

which is the product between $\chi^{(2)}$ and the peak electric field, E, of our laser pulse, is significant comparing to the first order susceptibility, $\chi^{(1)}$ which is in the order of unity. And the significant amount of second-harmonic light can be generated.

2.3 High-Harmonic Generation

To reach the extreme ultraviolet region of the electromagnetic spectrum, we need to generate the 40th order harmonic of the laser. One possibility is to use the 40th-order susceptibility $\chi^{(40)}$ of a solid. Unfortunately, conventional harmonic generation from solid-state materials is in the regime known as perturbative nonlinear optics where the conversion efficiency of higher orders of harmonics decrease as the reciprocal of the harmonic order. As a result, the conversion efficiency to extreme ultraviolet light is infinitesimal. In addition, the solid-state materials are not very tolerant to the intense laser light and tend to absorb most of extreme-ultraviolet radiation.

The situation is different in gaseous state. Electrons are strongly bounded to the atoms but have some finite probability to ionize to the continuum states with a laser pulse. Then, the laser electric field manipulates the trajectories of electrons which might again interact with ions. Processes involved this mechanism are no longer in the regime of perturbative nonlinear optics [70].

High-harmonic generation is a non-perturbative nonlinear optical process [71, 70, 72, 73, 74, 75], first demonstrated in the late 1980s [76, 77, 78]. High orders of odd-multiple harmonics of the laser are generated up to a cut-off energy. Among the harmonic orders, the conversion efficiencies are relatively constant which is the signature of a non-perturbative regime.

The simplest model to understand and describe high-harmonic generation is the semi-classical three-step model [79]. As the name implies, the model composes of three basic mechanisms: tunneling ionization, free propagation, and recombination.

2.3.1 Step 1: Tunneling Ionization

When the laser electric field is comparable to the field inside atoms, the laser electric field potential ($V_E = eEx$, where x is the distance away from the nucleus) can significantly distort the Coulomb potential from the nucleus. Consequently, there is a finite probability that an electron quantum-mechanically can tunnel away from the parent atoms.

Ammosov, Delone, and Krainov (ADK) described the rate of this tunneling ionization [80][1] by the ADK equation:

$$W(t) = -\frac{1}{N(t)}\frac{dN(t)}{dt} = \omega_p |C_{n*}|^2 (\frac{4\omega_p}{\omega_t})^{2n^*-1} e^{-\frac{4\omega_p}{3\omega_t}}, \tag{2.2}$$

where $N(t)$ is the number of **neutral** atoms at time t, $\omega_p = \frac{I_p}{\hbar}$, I_p is the ionization potential of gases (24.59 eV for He, 21.56 eV for Ne, and 15.76 eV for Ar), $\omega_t = \sqrt{\frac{e|E(t)|}{2mI_p}}$, $n^* = Z\sqrt{\frac{I_H}{I_p}}$, $|C_{n^*}|^2 = \frac{2^{2n^*}}{n^*\Gamma(n^*+1)\Gamma(n^*)}$, I_H is the ionization potential of hydrogen (13.6 eV), $E(t)$ is the laser electric field, m is the mass of an electron, Z is the order of ionization, and $\Gamma(x)$ is Gamma function defied as $\Gamma(x) = \int_0^\infty e^{-t}t^{x-1}dt$.

When the ionization is first-order kinetic (neutral atom $\rightarrow$ ion + e^-), the ratio of the number of ions ($N_0 - N(t)$) to the initial number of atoms (N_0) defined as the ionization fraction ($\eta = 1 - \frac{N}{N_0}$) can be calculated from

$$\eta(t) = 1 - \exp[-\int_{-\infty}^{t} W(t')dt']. \tag{2.3}$$

With the ADK rate equation (Equation 2.2), the fraction ionization can be calculated (Figure 2.1). During the first half of the laser pulse, the fraction ionization behaves like a step function where ionizations occur mostly at crests and troughs of the electric field wave, which happens at every half period of the laser electric field. At the

[1] The justification for using this ADK rate equation is derived from the Keldysh parameter [81], $\gamma = \sqrt{\frac{I_p}{2U_p}}$, where I_p is the ionization energy of the atom and U_p is the pondermotive potential defined in Equation 2.6. For the tunneling ionization described by the ADK equation, γ needs to be <1, otherwise the ionization is in the multi-photon regime. Our laser gives γ around 0.4 for neon.

second half of the laser pulse, the ionization fraction statutes at a some point of time, when the electric field becomes weaker.

2.3.2 Step 2: Free Propagation

After the electron-tunneling ionization, laser electric field modulates electron trajectory. This simple three-step model describes this behavior by classical mechanics:

$$m\ddot{x} = eE, \tag{2.4}$$

where x is the distance away from the atom, m is electron mass, e is electron charge and E is electric field. The electric field is defined with the phase constant (ϕ) and amplitude ($E_0(t)$):

$$E = E_0(t)\cos(\omega t + \phi). \tag{2.5}$$

This equation of motion has an analytical solution if the field amplitude (E_0) is a constant. After integrating the equation of motion and setting the initial conditions to zero for both position and velocity [82], we can construct the electron trajectories. A constant electric field amplitude is a good approximation because the profile variation of the pulse envelop is slow comparing to the time scale of high-harmonic generation, i.e., one half of an optical cycle. In contrast to the pulse profile, the phase factor, ϕ, is more critical. Physically, the phase constant corresponds to either a constant phase shift of the laser field or the time for tunneling ionization to happen[2] . In this case, I use a Gaussian-envelop electric field (Figure 2.1) to calculate electron trajectories from different laser phases, ϕ. The time zero of the calculation is set to the peak of the laser pulse.

I calculate only the phases ϕ from 0 to π since the trajectories just reverse when the electric field changes sign. For the phase of $0 < \phi < \frac{\pi}{2}$, initially, the electric field carries the electron away from the ion. Then, when the electric field reverses the sign,

[2] This is because the phase can be absorbed into the time parameter by defining $\phi = \omega t_0$

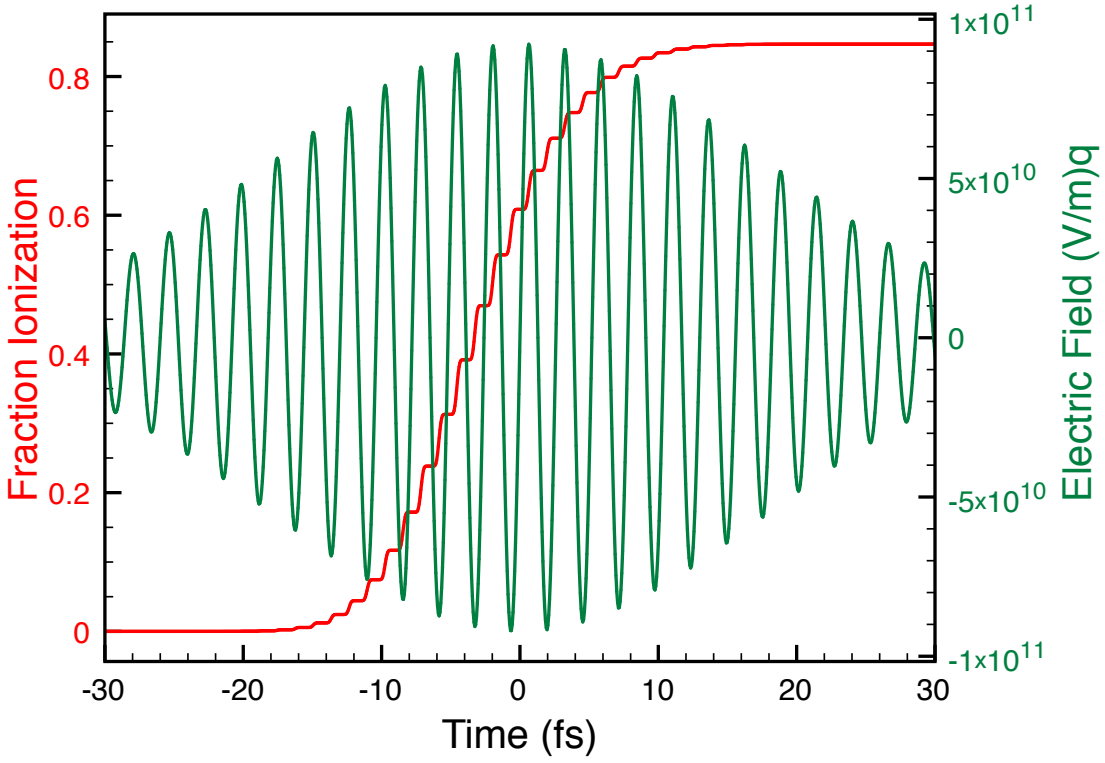

Figure 2.1: Fraction ionization (η red) calculated from ADK rate equation (Equation 2.2). The fraction ionization is a step function, where each step occurs at every half optical-cycle of the laser pulse (green) because the electric field reaches its local maxima, and electrons have higher probability to tunneling ionize. The gas medium is neon, and the laser pulse parameters are 25-fs pulse duration, 2.25-mJ pulse energy, 90-μm diameter focal-spot size, and 780-nm wavelength).

the electron trajectory is also reversed and crosses the starting point ($x = 0$) (solid lines in Figure 2.2); therefore, the recombination between the ion and electron, the third step in our simple model, can occur. However, for the phase of $\frac{\pi}{2} < \phi < \pi$, the electron only drifts away from the ion and never returns.

In addition, the calculation results validate the assumption made in the equation of motion (Equation 2.4), which assumes that electrons are free from atoms, and the electron trajectory can be described with classical mechanics. The calculation suggests that the distance which the electron is carried away by the electric field is in an order of a few nanometers (Figure 2.2). This distance is significantly greater than the atomic radii which are in the order of Å. This large distance confirms the free electron approximation. Moreover, the maximum possible kinetic energy of the electron is about 180 eV which is much lower than the rest mass of an electron at 0.5 MeV, validating the use of classical mechanics rather than a relativistic approach.

2.3.3 Step 3: Recombination

From the calculated electronic paths in the previous step, one half of the electrons reverse the direction of the propagation and cross the origin ($x = 0$) again. It is possible for these returning electrons to recombine with the ions. Since these electrons gain some kinetic energy during the course of travel, the remaining energy after recombining with the ions is released into high-harmonic photons. I calculate the return kinetic energies for different laser phases, ϕ (Figure 2.3). At the phase of 0.09π, the electron gains the highest possible kinetic energy, and if high-harmonic generation occurs at this phase, the harmonic will yield that highest photon energy, called the cutoff energy, $h\nu_{cutoff}$. It is conventional to write the cutoff energy in the term of pondermotive energy defined as mean kinetic energy gained during one laser optical cycle,

$$U_p = \frac{e^2|E_0|^2}{4m\omega^2} = \frac{e^2 I}{2m\epsilon_o cn\omega^2} \propto I\lambda^2, \tag{2.6}$$

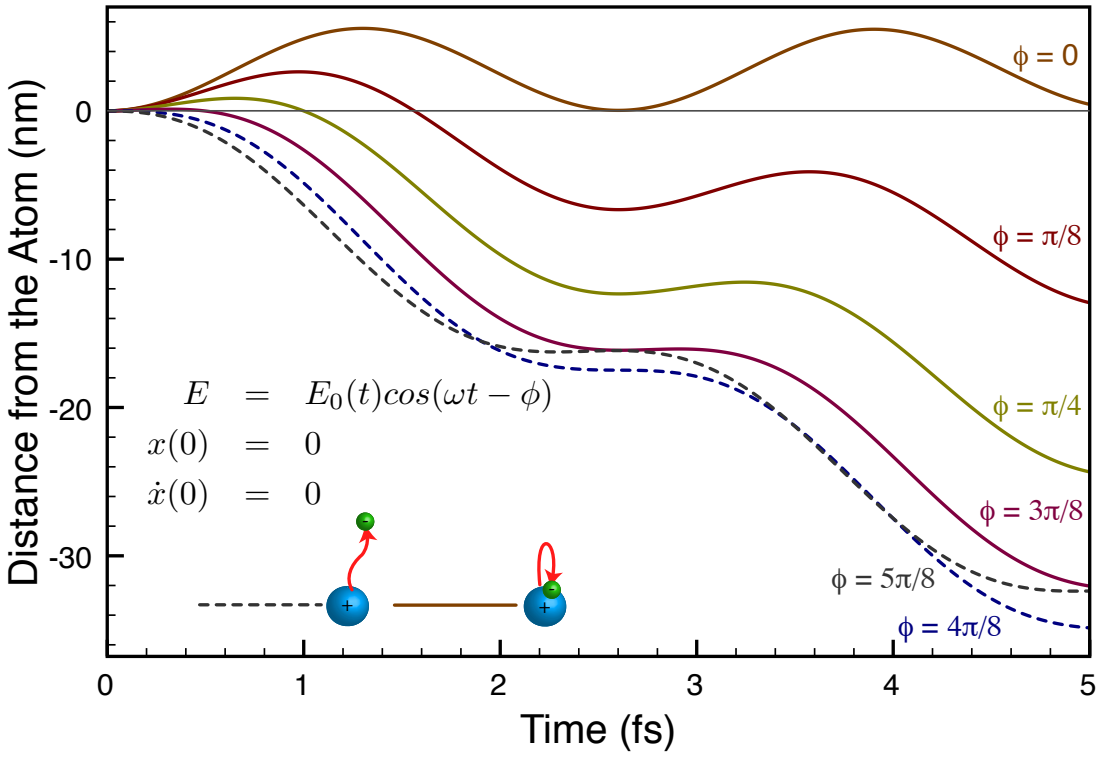

Figure 2.2: Calculated electron trajectories from the Newtonian mechanics for different values of the phase constants ϕ. The solid lines represent the trajectories allowing for the revisit of the electron the parent ion, and the dashed lines represent the trajectories that the electron never returns to the ion. The electric-field pulse, $E(t)$, is defined as in Figure 2.1. The initial velocity and location are both zero. The time zero of the calculation is set to the peak of the laser pulse.

where E_0 is the peak electric field, ω is laser frequency. The maximum possible kinetic energy gained is $3.17U_p$ (Figure 2.3). The ion is initially in the excited state where the energy is equal to the ionization potential I_p; therefore, the cut-off energy is equal to

$$h\nu_{cutoff} = I_p + 3.17U_p. \tag{2.7}$$

The cutoff rule suggests three degrees of freedom to control the cutoff energy of high harmonics: the ionization energy I_p, the driving laser wavelength λ, and laser intensity I. First, the cutoff energy can be extended by choosing gas species that have high ionization potential. For this reason, nobel gases are usually preferred as high-harmonic media and helium shows the largest cutoff energy among all noble gases. Moreover, the ADK fractional ionization decreases greatly with higher ionization potential. The mechanism allows for the phase match of high-harmonic conversion at higher photon energy. I will discuss this point in the next section. Second, the high-harmonic cutoff increases with a longer wavelength driving laser. This approach allows for high-harmonic generation at water window and soft x-rays [83, 84]. Third, the cutoff is extended when electrons gain more kinetic energy by more intense laser pulses. This observation implies that the cutoff energy is higher by the conversion with a shorter laser-pulse duration.

Up to now, my consideration on high-harmonic generation is based only on one laser cycle located at the peak of the laser pulse ($t = 0$ in Figure 2.1), which is the time zero of the electron trajectories in my calculation. However, this time zero is not the only possibility. As described by ADK the equation for the tunneling ionization rate, the ionization can also take place anywhere at the crests and troughs of the electric-field wave (Figure 2.1). With different time zeros, the same cut-off rule still describes the highest high-harmonic energy (Equation 2.7) because the pulse envelop is slowly varying comparing to the laser optical cycle. But since the pondermotive energy depends on the electric field, the numerical value of high-harmonic cutoff from the peak of the laser pulse is always the highest.

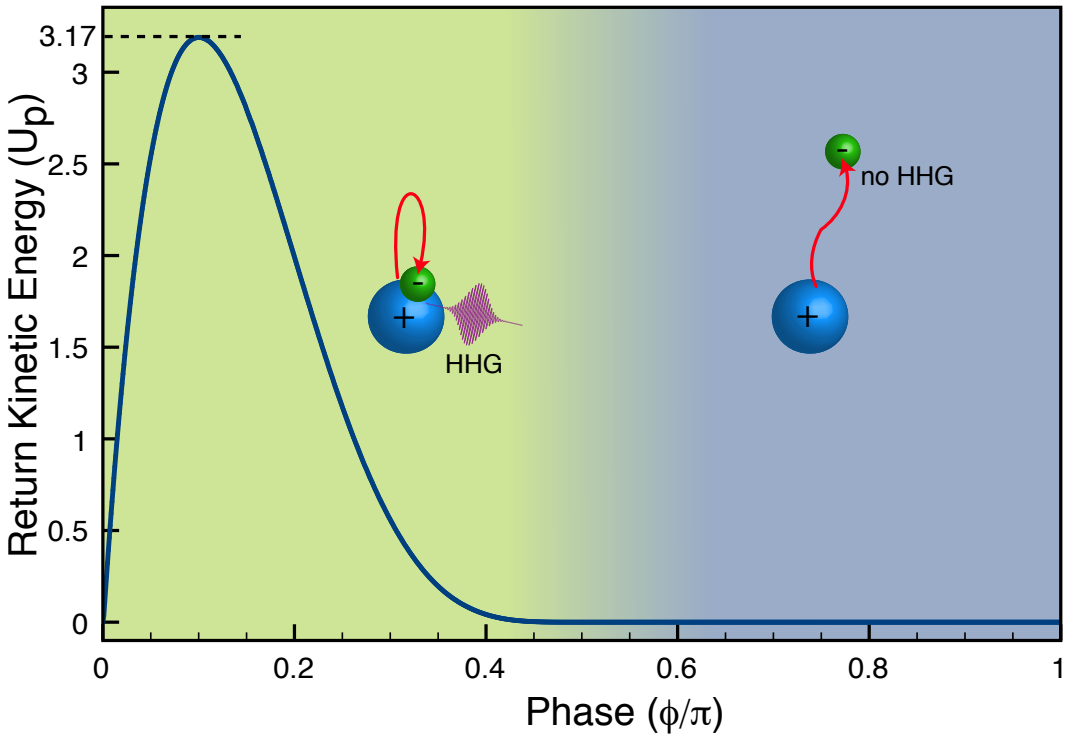

Figure 2.3: The return kinetic energy of electrons as a function of the laser phase (ϕ). Electrons only return to the parent ion when the laser phase ranges from 0 to $\frac{\pi}{2}$. The maximum possible kinetic energy gained is equal to $3.17U_p$, where U_p is the pondermotive energy defined as an average kinetic energy gained by an electron during one laser optical cycle.

From the picture of tunneling ionizations at every half-optical cycles, the three-step model also predicts the time structure of harmonics. In the time domain, high harmonics are actually a train of pulses with the spacing between pulses of about one half of the laser optical cycle, $\frac{T}{2} = \frac{1}{2f}$. The high-harmonic pulse duration, which ranges from attoseconds to a few femtoseconds, is determined by the number of optical cycles involved in the tunneling ionization. When the number of cycles is lower, the total harmonic pulse duration is shorter. This idea motivates the driven of high-harmonic with laser composing of the fewest optical cycles to generate a single attosecond pulse [85, 86, 87].

In addition, by looking at high-harmonics as a pulse train, the high-harmonic spectra must be in the form of frequency combs. Since a period of high-harmonic pulse train is $\frac{1}{2f}$, by performing a Fourier transform, the spectra are also a comb of delta function but with the separation of $\frac{2}{T} = 2f$. This spectral spacing agrees with the experimental high-harmonic spectra that contain only odd multiples of harmonics. With this idea, to create harmonics at all integer orders, one method is to seed a small amount of second harmonic light with the fundamental light [88]. The second harmonic beam breaks the symmetry of the nobel gas media such the tunneling ionizations occur at every full optical cycle, $T = \frac{1}{f}$. As a result, the spacing between harmonics reduces to one fundamental frequency, f.

2.4 Phase Matching

In the previous Section, the three-step model is only used a simple picture for an interaction between the laser field and a single atom to predict the cutoff energy of high harmonics. In practical, high-harmonic generation involves a large number of atoms ($\sim 10^{23}$) and some conditions must be met to yield the highest photon flux. Similar to most of the nonlinear processes, the laser phase velocity ($k_{laser} = k_{\omega}$) must be equal to the phase velocity of harmonics ($k_{harmonic} = k_{q\omega}$). If any phase mismatch exists,

$\Delta k = k_{laser} - k_{harmonic}$, the two light fields will destructively interfere at some point of time resulting in the low high-harmonic intensity.

The phase-matching of high-harmonic generation is available in many geometries [75]. Our group uses a hollow-waveguide geometry that employs glass capillaries filled with noble gases. The confinement of gas atoms in a capillary allows us to adjust the gas pressure to reach the phase-matching condition because the phase mismatch, Δk, is pressure dependent,

$$\Delta k \approx N(\frac{u_{11}^2 \lambda}{4\pi a^2} - P(1-\eta)\frac{2\pi}{\lambda}(\Delta\delta + n_2) + P\eta n_a r_e \lambda), \tag{2.8}$$

where N the harmonic order, u_{11} the first zero of Bessel function $J_0(\approx 2.4)$, λ is the laser frequency, a is the diameter of the waveguide, P is the pressure, η is ionization fraction (Equation 2.3), $n_2 = \tilde{n}_2 I$ is the nonlinear index of refraction, $\Delta\delta$ is the difference between the refractive indices of the fundamental and high harmonics, n_a is the number density of atoms at 1 atm, and r_e is the classical electron radius.

In the above equation, three sources of the phase mismatch contribute to each term: the waveguide geometry, dispersion in a neutral gas, and dispersion in a plasma, respectively [89, 90]. The phase-matching conversion achieves when the control of pressure balances contributions since the waveguide geometry (first term) and the plasma term (third term) contribute oppositely to the neutral term (second term). However, the possibility for the phase-mismatch compensation breaks down at high ionization fraction, η. By setting the second and the third terms of the phase mismatch condition to zero, the critical ionization fraction, η_c, which is the maximum possible value of η for any phase matching, is

$$\eta_c = \frac{1}{1 + \frac{n_a r_e \lambda^2}{2\pi\Delta\delta}}. \tag{2.9}$$

The critical ionization fraction are $\approx 4\%$ for Ar, $\approx 1\%$ for Ne, and $\approx 0.5\%$ for He [84, 90] from 780 laser nm. These numbers suggests that the bright high-harmonic generation happens only at the early part of the laser pulse where the ionization fraction is still

lower than the critical value (Figure 2.1). As a result, experimentally observed harmonic cutoff energies are always lower than the estimation by use of the peak intensities.

2.5 Conclusions

Semiclassical three-step model is a powerful and intuitive approach to understand high-harmonic generation. The model predicts the cutoff energy of high harmonics by a classical mechanic approach. In time domain, high-harmonics are a series of pulses with the period of one half optical cycle between them, which explains why high-harmonic spectra are combs of odd-interger harmonics. Besides the three-temperature model, the phase matching condition must be fulfilled to yield the brightest high-harmonic flux.

Chapter 3

Magneto-optics in the Extreme Ultraviolet

3.1 Introduction

In the previous chapter, we explore the fundamental physics behind high-harmonic generation to produce short pulses in the range of extreme ultraviolet. This section covers another important subject of how can high harmonics or any light in the extreme-ultraviolet region can probe magnetism.

Table 3.1: Example of Magneto-optical Effects

Magneto-optical Effects	Geometry [a]	Detection Scheme[b]	References
Transverse MOKE[c]	R	I	[91, 12, 92, 93]
Polar and Longitudinal MOKE	R	P	[94]
Magnetic Circular Dichroism	T	I	[95, 96, 97, 98, 99]
Linear Dichroism Dichroism	T	I	[100, 101]
Faraday Effect	T	P	[102, 103, 104, 105, 106]

[a] R = Reflection, T= Transmission
[b] I = Intensity measurement , P= Polarization analysis
[c] Magneto-optical Kerr Effect

A typical approach to probe magnetization is to employ the interaction between light and the magnetization via magneto-optical phenomena [107, 108, 109]). By measuring the properties of light induced from magnetic interactions, the state of magneti-

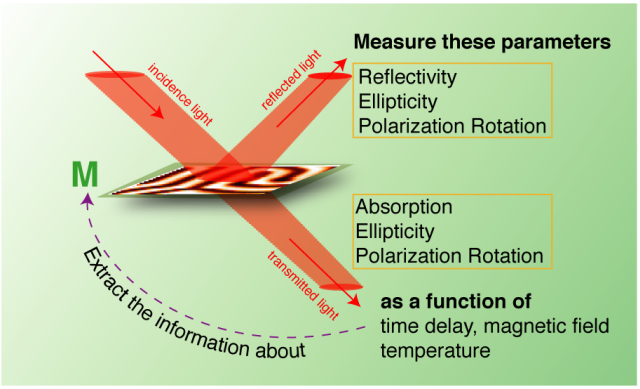

Figure 3.1: Magneto-optical effects as the probes of magnetizations

zation can be inferred. Although there are many types of magneto-optical effects (Table 3.1), the fundamental physics behind all of them are directly related to the symmetry reduction by magnetization. Mathematically, the symmetry of materials consider from a permittivity tensor ($\hat{\epsilon}$), defined as $\mathbf{D} = \hat{\epsilon}\mathbf{E}$. For isotropic materials, the permittivity tensor is a constant (ϵ), which relates to the reflective index ($n_0 = \sqrt{\epsilon}$). But for magnetized magnetic materials, the constant generalizes to a matrix ($\hat{\epsilon}$) that contains an off-diagonal element (ϵ'):

$$\hat{\epsilon} = \begin{pmatrix} \epsilon & \epsilon' & 0 \\ -\epsilon' & \epsilon & 0 \\ 0 & 0 & \epsilon \end{pmatrix}. \tag{3.1}$$

In this case, I simplify the form of matrix $\hat{\epsilon}$ by assuming that all off-diagonal elements are identical and the magnetization has no x or y components.

The off-diagonal element, ϵ', or the magneto-optical constant, is directly related to magnetization because the matrix transform in the same way[1] . Moreover, the

[1] This permittivity tensor represents the magnetization in z direction; therefore, the tensor should transform in the same way as a vector in z direction. For example, if we perform a 180 degree rotation along x axis by a rotation matrix $\hat{T} = \begin{pmatrix} 1 & 0 & 0 \\ 0 & -1 & 0 \\ 0 & 0 & 1 \end{pmatrix}$, the rotation transformation, $\bar{\hat{\epsilon}} = \hat{T}^T\hat{\epsilon}\hat{T}$, will result in the same matrix, but with the opposite sign of ϵ' (ϵ' turns to $-\epsilon'$.). The transformation is equivalent to the reversal of magnetization.

opposite sign in the off-diagonal element is the direct consequence of Onsager's relation, $\epsilon_{ij}(M) = -\epsilon_{ji}(M) = \epsilon_{ji}(-M)$ [110]. One of the most important properties of ϵ' is that its size is usually small compare to the diagonal element,

$$|\epsilon'| \ll |\epsilon|. \tag{3.2}$$

The condition is valid in in extreme ultraviolet and soft x-ray range where ϵ' is in the order of 10^{-3} [12] and the refractive index, $n_0 = \sqrt{\epsilon}$, is close to unity [111] (Figure 3.2). The condition allows for the simplification of many equations by Taylor expansions up to the highest order in ϵ'. Relying on this approximation of the permittivity tensor, I will discuss the four magneto-optical effects: transverse magneto-optical effect, magnetic linear dichroism, magnetic circular dichroism and Faraday effect.

3.2 The propagation of light through media

The first step of the analysis is to describe the propagation of light through magnetic materials. At the end, we will have an equation to determine the refractive index as a function of the magnetic constant (ϵ').

The propagation of light in extreme ultraviolet or soft x-ray range can be explained by a plane wave [111],

$$\mathbf{E} = \mathbf{E}_0 e^{i(\mathbf{k}\cdot\mathbf{r} - \omega t)}. \tag{3.3}$$

Although the equation is in a simple form, a special attention is needed here because it contains the refractive index, n which is highly dispersive and material specific in extreme ultraviolet or soft x-ray range. It is convenient to write the reflective index in the term of

$$n = 1 - \delta + i\beta. \tag{3.4}$$

The motivation of writing n in the above form is understandable by combining

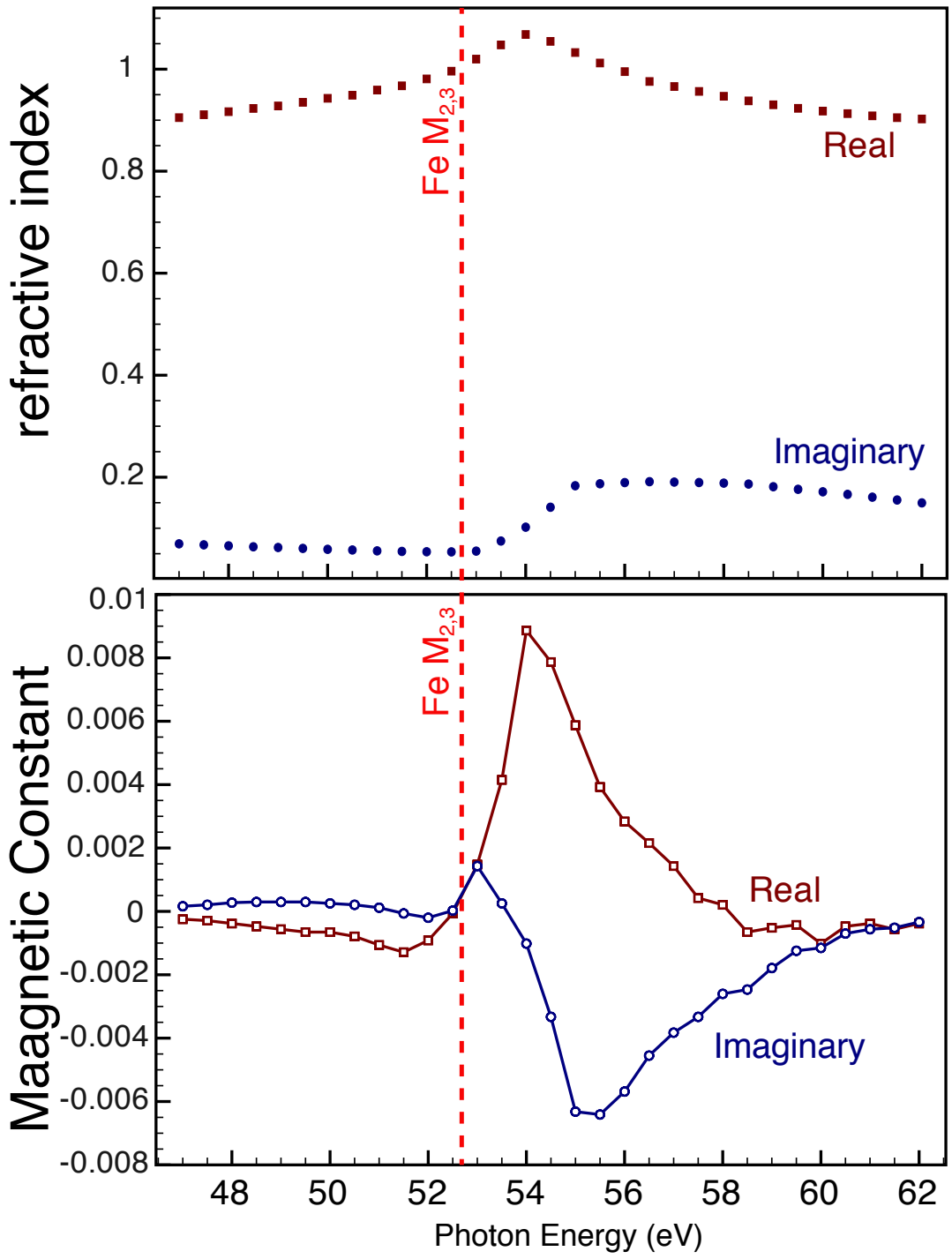

Figure 3.2: The refractive index (n_0 top) and the magnetic constant, which is the off-diagonal element of the permittivity tensor, (ϵ' bottom) of Fe around M-shell absorption edges (red dashed line). Data from [12, 13]

Equation 3.3 and 3.4,

$$\mathbf{E} = \mathbf{E}_0 e^{i(k_0(1-\delta+i\beta)\hat{\mathbf{k}}\cdot\mathbf{r}-\omega t)} \tag{3.5}$$

$$= \mathbf{E}_0 e^{i(\mathbf{k_0}\cdot\mathbf{r}-\omega t)} e^{-i(k_0\delta\hat{\mathbf{k}}\cdot\mathbf{r})} e^{-(k_0\beta\hat{\mathbf{k}}\cdot\mathbf{r})} \tag{3.6}$$

where $k_0 = \frac{\omega}{c} = \frac{|\mathbf{k}|}{n} = \frac{k}{n}$ is the wavevector in vacuum. The parameter δ controls the phase shift due to the presence of media, while the parameter β describes the absorption in media. Experimentally, the reflective indexes in extreme ultraviolet or soft x-ray range deviate by only small amount from unity, i.e. β, δ are small numbers (Figure 3.2).

The more fundamental physics behind the material phase shift and the absorption are described through scattering processes. The parameters δ, β are related to the real and imaginary part of the atomic scattering factor ($f^0 = f_1^0 - if_2^0$):

$$\delta = \frac{n_a r_e \lambda^2}{2\pi} f_1^0 \tag{3.7}$$

$$\beta = \frac{n_a r_e \lambda^2}{2\pi} f_2^0, \tag{3.8}$$

where the zero superscript implies that the scatterings is at the small angle (forward scattering approximation), n_a is the average density of atoms, and $r_e = \frac{e^2}{4\pi\epsilon_0 mc^2}$, the average radius of electron[2] . The calculation of the scattering amplitude is very complicated for multi-electron atoms and typically the data come from experiments. The tabulated data of the scattering factors can be found in x-ray databases [13] (Figure 3.3).

The previous consideration on refractive index does not account for magnetic contribution. To calculate the refractive index inside magnetic materials, we start with

[2] This expression can be derived simply by equating the "electrostatic energy" of an electron, $\frac{e^2}{4\pi\epsilon_0 r_e}$, with its rest mass mc^2.

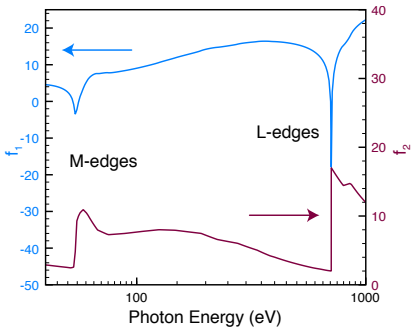

Figure 3.3: f_1^0 and f_2^0 parameters of Fe, which are related to the real and imaginary of the refractive index, respectively [13]. Both graphs show two significant discontinuities at M- and L-shell absorption edges.

the Maxwell's equations:[3]

$$\nabla \times \mathbf{H} = \frac{1}{c}(\hat{\epsilon} \cdot \dot{\mathbf{E}}) \tag{3.9}$$

$$\nabla \times \mathbf{E} = -\frac{1}{c}\dot{\mathbf{H}}, \tag{3.10}$$

and by combining the two, we get

$$c^2(\nabla^2\mathbf{E} - \nabla(\nabla \cdot \mathbf{E})) = \hat{\epsilon} \cdot \ddot{\mathbf{E}}. \tag{3.11}$$

With the plane wave solution (Equation 3.3), the final equation is

$$-\mathbf{k}(\mathbf{k} \cdot \mathbf{E}) + k^2\mathbf{E} = k_0^2\hat{\epsilon} \cdot \mathbf{E}. \tag{3.12}$$

The equation allows for the calculation of refractive index n which is implicit inside the wavevector, $k = \frac{\omega n}{c}$. The magnetic contribution comes from the permittivity tensor (Equation 1). To find the refractive index, we have to solve a vector equation (Equation 3.12). The solutions depend on the direction of light propagation and magnetization; therefore, the analysis must be separated into special cases for each of the magneto-optical effect.

[3] **H** represents magnetic field, which has the unit of Oersted (Oe) in CGS and Ampere per meter (A/m) in SI. **B**, on the other hand, is **not** the magnetic field but a magnetic flux density which has a unit of Gauss (G) in CGS Tesla (T) in SI.

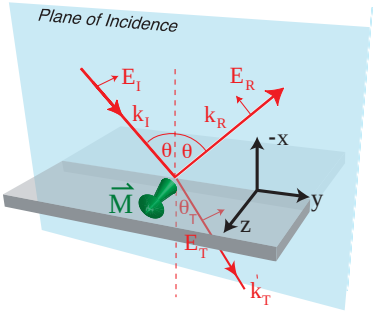

Figure 3.4: The geometry of transverse-magneto optical Kerr effect (T-MOKE). Magnetization aligns in the sample plane and transversly to the plane of incidence. Here, the magnetization is in the z direction. The incident polarization is in p-polarization.

3.3 Transverse Magneto-optical Kerr Effect (T-MOKE)

3.3.1 Calculating Magnetization Dependent Refractive Index

Transverse magneto-optical Kerr effect (T-MOKE) describes the coupling of magnetization to the light field into the reflectivity of p-polarized light [112] when the magnetization is aligned transverse to the plane of incidence (Figure 3.4). I first discuss this geometry because it is important for all experiments covered in this thesis. T-MOKE is chosen for the experiments because it is suitable for extreme ultraviolet high harmonics. The probing of magnetization via T-MOKE does not require any polarization analysis technique or circular-polarization conversion (Table 3.1), which are challenging techniques in extreme-ultraviolet region [113, 114, 115, 116].

To understand the dependence of magnetization on reflectivity, I set up the coordinate system such that the magnetization aligns in the z direction, and the incident and transmitted light is in the xy plane,

$$\mathbf{k}_I = (k_0 \cos\theta, k_0 \sin\theta, 0) \tag{3.13}$$

$$\mathbf{k}_T = (k \cos\theta_T, k \sin\theta_T, 0). \tag{3.14}$$

I assume that light approaches from a vacuum ($|\mathbf{k}_I| = |\mathbf{k}_R| = k_0$) into a magnetic

material ($|\mathbf{k}_T| = k = nk_0$). The refractive angle (θ_T) relates to the incident angle (θ) by Snell's law, $\sin\theta = n\sin\theta_T$.

Then, I substitute the wave vector into Equation 3.12 with $\mathbf{E} = [E_{xT}, E_{yT}, E_{zT}]$,

$$k_0^2 \begin{pmatrix} \epsilon - n^2\sin\theta_T^2 & \epsilon' + n^2\sin\theta_T\cos\theta_T & 0 \\ -\epsilon' + n^2\sin\theta_T\cos\theta_T & \epsilon - n^2\cos\theta_T^2 & 0 \\ 0 & 0 & \epsilon - n^2 \end{pmatrix} \cdot \begin{pmatrix} E_{xT} \\ E_{yT} \\ E_{zT} \end{pmatrix} = 0. \quad (3.15)$$

The next step is to solve these equations. This system of equations always has a trivial solution of $[E_{xT}, E_{yT}, E_{zT}] = 0$. The determinant of the matrix must be zero for the nontrivial solution:

$$(n^2 - \epsilon)((n^2 - \epsilon)\epsilon - (\epsilon')^2) = 0, \quad (3.16)$$

which has the solutions,

$$n_s^2 = \epsilon \quad (3.17)$$

$$n_p^2 = \epsilon + \frac{\epsilon'^2}{\epsilon}. \quad (3.18)$$

Interestingly, these two possible refractive indexes are independent from the geometrical angles. The method of finding the refractive indexes becomes an eigenvalue problem. For each of the value of $n_{s,p}^2$, which are 'eigenvalues', we can solve for their 'eigenvectors' by substituting the values of $n_{s,p}^2$ back to Equation 3.15. The results are

$$\mathbf{e}_s = \begin{pmatrix} 0 \\ 0 \\ 1 \end{pmatrix} \quad (3.19)$$

$$\mathbf{e}_p = \begin{pmatrix} 1 \\ \frac{\epsilon'\sin\theta_T - \epsilon\cos\theta_T}{\epsilon'\cos\theta_T + \epsilon\sin\theta_T} \\ 0 \end{pmatrix}, \quad (3.20)$$

for $n_s^2 = \epsilon$ and $n_p^2 = \epsilon + \frac{\epsilon'^2}{\epsilon}$, respectively.

The above results indicate that there are two possible reflective indexes for the system; one is magnetic (through ϵ') and the other is only optical. The choice of reflective indexes is dependent on the direction of polarization. If any unpolarized light enters the media, the beam will split into two parts weighted by the amount of projection on the eigenvectors shown above. This phenomenon also happens in non-magnetic, anisotropic materials, in which case it is known as birefringence.

The first eigenvalue, $\mathbf{e}_s$, reveals that the light with polarization along the z axis, i.e. s-polarized light, does not interact with magnetization. One the other hand, the magnetic effect contributes to the second eigenvector, $\mathbf{e}_p$, which is elliptical polarized light (ϵ' and ϵ are in general complex numbers). This polarization is almost p-polarized because a Taylor series expansion of the expression for $\mathbf{e}_p$ up to first order in ϵ' yields

$$\mathbf{e}_p = \begin{pmatrix} -\sin\theta_T - \frac{\epsilon'}{\epsilon}\sec\theta_T \\ \cos\theta_T \\ 0 \end{pmatrix}. \tag{3.21}$$

Because ϵ' is usually a small complex number, the eigenvector $\mathbf{e}_p$ is mostly linearly p-polarized.

From the above analysis, the origin for the T-MOKE can be traced to the dependence of refractive indexes on the magnetization. Indirectly, the reflectivity must also involve magnetization. The next step of our analysis is to find the reflectivity by applying the boundary conditions to the **E** and **H** fields to solve for reflectivity. And to simplify the mathematics, we will consider only special cases for s- and p-polarization as they are linearly independent eigenvectors of the system.

3.3.2 Reflectivity of p-polarized Light

In the case of p-polarized probe light, the relevant electric-field vectors are

$$\mathbf{E}_I = E_{I0}(-\sin\theta, \cos\theta, 0) \tag{3.22}$$

$$\mathbf{E}_R = E_{R0}(-\sin\theta, -\cos\theta, 0) \tag{3.23}$$

$$\mathbf{E}_T = E_{T0}(-\sin\theta_T - \frac{\epsilon' \sec\theta_T}{\epsilon}, \cos\theta_T, 0). \tag{3.24}$$

where, in the transmitted field (Equation 3.24), I employ the derived eigenvectors (Equation 3.21). In the same manner, the wavevectors ($\mathbf{k}$) are

$$\mathbf{k}_I = k_0(\cos\theta, \sin\theta, 0) \tag{3.25}$$

$$\mathbf{k}_R = k_0(-\cos\theta, -\sin\theta, 0) \tag{3.26}$$

$$\mathbf{k}_T = k_0\sqrt{\epsilon + \frac{\epsilon'^2}{\epsilon}}(\cos\theta_T, \sin\theta_T, 0). \tag{3.27}$$

Similarly, magnetic field vectors are calculated from the relation $\mathbf{H} = \frac{\mathbf{k}\times\mathbf{E}}{k_0}$:

$$\mathbf{H}_I = (0, 0, E_{I0}) \tag{3.28}$$

$$\mathbf{H}_R = (0, 0, E_{R0}) \tag{3.29}$$

$$\mathbf{H}_T = \sqrt{\epsilon + \frac{\epsilon'^2}{\epsilon}})(0, 0, E_{T0}(1 + \tan\theta_T \frac{\epsilon'}{\epsilon}). \tag{3.30}$$

Then, the electromagnetic boundary conditions require the continuity of electromagnetic field at the interface,

$$\mathbf{E}_{Iy} + \mathbf{E}_{Ry} = \mathbf{E}_{Ty} \tag{3.31}$$

$$\mathbf{H}_{Iz} + \mathbf{H}_{Rz} = \mathbf{H}_{Tz}. \tag{3.32}$$

With all of the provided information, the transmission coefficient, i.e. the ratio of the transmitted electric field amplitude to the incident electric field, is

$$\frac{E_{T0}}{E_{I0}} = \frac{2\cos\theta}{\cos\theta_T + \cos\theta(1 + \tan\theta_T \frac{\epsilon'}{\epsilon})\sqrt{\epsilon + \frac{\epsilon'^2}{\epsilon}}}, \tag{3.33}$$

and the reflection coefficient is

$$\frac{E_{R0}}{E_{I0}} = \frac{\cos\theta_T - \cos\theta(1+\tan\theta_T\frac{\epsilon'}{\epsilon})\sqrt{\epsilon+\frac{\epsilon'^2}{\epsilon}}}{\cos\theta_T + \cos\theta(1+\tan\theta_T\frac{\epsilon'}{\epsilon})\sqrt{\epsilon+\frac{\epsilon'^2}{\epsilon}}}. \tag{3.34}$$

Both coefficients are simplified by expanding up to the first order in ϵ',

$$\frac{E_{T0}}{E_{I0}} = \frac{2\cos\theta}{\sqrt{\epsilon}\cos\theta+\cos\theta_T} - \frac{2\cos\theta^2\tan\theta_T\epsilon'}{\sqrt{\epsilon}(\cos\theta_T+\sqrt{\epsilon}\cos\theta)^2} \tag{3.35}$$

$$\frac{E_{R0}}{E_{I0}} = \frac{\sqrt{\epsilon}\cos\theta-\cos\theta_T}{\sqrt{\epsilon}\cos\theta+\cos\theta_T} + \frac{2\sin\theta_T\cos\theta\epsilon'}{\sqrt{\epsilon}(\cos\theta_T+\sqrt{\epsilon}\cos\theta)^2}. \tag{3.36}$$

Finally, by writing ϵ in the term of the reflective index n_0, and the angle of incidence θ in the term of refracted angle θ_T by the Snell's law[4] ,

$$\sin\theta = n_0\sin\theta_T, \tag{3.37}$$

the transmission and reflection coefficients become

$$\begin{aligned}\frac{E_{T0}}{E_{I0}} &= \frac{2\cos\theta}{n_0\cos\theta+\sqrt{1-\frac{\sin\theta^2}{n_0^2}}} + \frac{2\cos\theta^2\sin\theta\epsilon'}{n_0^2\sqrt{1-\frac{\sin\theta^2}{n_0^2}}(n_0\cos\theta+\sqrt{1-\frac{\sin\theta^2}{n_0^2}})^2} \\ &= T_0 + T_M\epsilon' \end{aligned} \tag{3.38}$$

$$\begin{aligned}\frac{E_{R0}}{E_{I0}} &= \frac{n_0\cos\theta-\sqrt{1-\frac{\sin\theta^2}{n_0^2}}}{n_0\cos\theta+\sqrt{1-\frac{\sin\theta^2}{n_0^2}}} + \frac{\sin 2\theta\epsilon'}{n_0^2(n_0\cos\theta+\sqrt{1-\frac{\sin\theta^2}{n_0^2}})^2} \\ &= R_0 + R_M\epsilon', \end{aligned} \tag{3.39}$$

where $T_0 = \frac{2\cos\theta}{n_0\cos\theta+\sqrt{1-\frac{\sin\theta^2}{n_0^2}}}$, $R_0 = \frac{n_0\cos\theta-\sqrt{1-\frac{\sin\theta^2}{n_0^2}}}{n_0\cos\theta+\sqrt{1-\frac{\sin\theta^2}{n_0^2}}}$, $T_M = \frac{2\cos\theta^2\sin\theta\epsilon'}{n_0^2\sqrt{1-\frac{\sin\theta^2}{n_0^2}}(n_0\cos\theta+\sqrt{1-\frac{\sin\theta^2}{n_0^2}})^2}$, and $R_M = \frac{\sin 2\theta\epsilon'}{n_0^2(n_0\cos\theta+\sqrt{1-\frac{\sin\theta^2}{n_0^2}})^2}$.

The first terms in both equations are exactly the Fresnel's coefficients (T_0, R_0) [117] for p-polarized light. They are optical contributions to the reflected and transmitted light, while the magnetic contributions are in the second terms. Because of the relative size between ϵ' and ϵ, the optical terms usually dominate the reflection and transmission over magnetic term. The magnetic term is only significant near absorption edges where ϵ' becomes important (Figure 3.2).

[4] The p-polarized refractive index is second order in magnetic contribution (Equation 3.18); therefore only the first order term is kept here.

Before moving on to the next section, I would like to mention an important terminology. The optical reflectivity (R_0 defined in Equation 3.39) is zero at the particular angle called Brewster angel (θ_B). By setting the reflectivity term (R_0) to zero, the Brewster angle can be found at,

$$\sin^2\theta_B = \frac{n_0^2}{1+n_0^2}, \tag{3.40}$$

or equivalently

$$\tan\theta_B = n. \tag{3.41}$$

For extreme ultraviolet and soft x-rays, n is close to unity; therefore, the Brewster angle is approximately 45°.

3.3.3 Asymmetry parameter

The reflection coefficient (Equation 3.39) is not a measurable parameter because we can only measure the intensities but not the electric field. By measuring the intensity, we measure the modulus square of the field ($|E_{R0}|^2$), which also contains a quadratic term on the ϵ' as well as the linear term. To extract only the magnetic information, a typical method is to switch the sign of magnetization, which reverses the sign of ϵ'. Then, the two intensities are subtracted to remove the optical contribution ($|R_0|^2$). It is also convenient to normalize the result by the sum of the data in order to get rid of the intensity fluctuations ($|E_{I0}|^2$). We call this the **asymmetry** parameter,[5] A,

[5] Without mentioning the magneto-optical contrast mechanism, I use the term asymmetry A for T-MOKE geometry only. Later on in this chapter, similar parameters from magnetic linear dichroism asymmetry A_{MLD} and magnetic circular dichroism asymmetry A_{MCD} are also introduced.

$$
\begin{aligned}
A &= \frac{|\mathbf{E}_{R0}(\epsilon')|^2 - |\mathbf{E}_{R0}(-\epsilon')|^2}{|\mathbf{E}_{R0}(\epsilon')|^2 + |\mathbf{E}_{R0}(-\epsilon')|^2} \\
&\approx 2\frac{\Re[R_0^* R_M \epsilon']}{|R_0|^2} \qquad (3.42) \\
&= 2\Re[\frac{R_0^* R_M \epsilon'}{R_0 R_0^*}] \qquad (3.43) \\
&= 2\Re[\frac{\sin(2\theta)\epsilon'}{(n_0^4 \cos^2\theta - n_0^2 + \sin^2\theta)}], \qquad (3.44)
\end{aligned}
$$

In the second line, I assume that in the denominator the optical reflectivity $|R_0|^2$ is significantly larger than the magnetic part $|R_M \epsilon'|^2$. The approximation is typically very good specially when the photon energy is not at the resonance, and when the angle of incident is far away from 45°. The maximum error is less than 10% (Figure 3.5).

The final expression of the asymmetry is linear in ϵ'. By measuring the asymmetry, we directly probe magnetization, if the prefactor in Equation 3.44 remains a constant during the measurement. This condition usually satisfies for the static asymmetry measurement at a constant wavelength. The asymmetry maximizes when the denominator is zero at the angle of incident of

$$\sin^2\theta_B = \frac{n_0^2}{1 + n_0^2}, \qquad (3.45)$$

or equivalently

$$\tan\theta_B = n. \qquad (3.46)$$

This special angle is exactly the Brewster angle as discussed earlier.

By applying the asymmetry equation (Equation 3.44), I calculate T-MOKE asymmetry of Fe as a function of photon energy and the angle of incidence (Figure 3.6, 3.7). The calculated asymmetry of Fe indicates that the maximum asymmetry above 50% peaks around the absorption M-edges of Fe with the angle of incidence around 45°. This result suggests that the experimental incident angle should be close to the Brewster angle to maximize the magnetic signal, although the reflectivity is very low but still in a reasonable order of 10^{-5}.

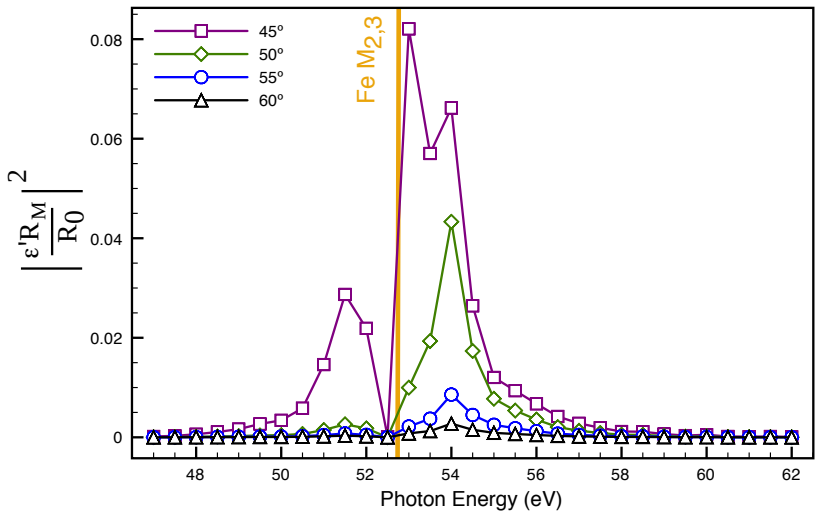

Figure 3.5: The ratio of the magnetic contribution, $|R_M\epsilon'|^2 = |\frac{\sin 2\theta\epsilon'}{n_0^2(n_0\cos\theta+\sqrt{1-\frac{\sin\theta^2}{n_0^2}})^2}|^2$, to the optical contribution, $|R_0|^2 = |\frac{\sqrt{\epsilon}\cos\theta-\cos\theta_T}{\sqrt{\epsilon}\cos\theta+\cos\theta_T}|^2$, of the reflectivity of p-polarization. The magnetic part is significant in comparison the optical near M-edges or near 45° angle of incidence (Brewster angle).

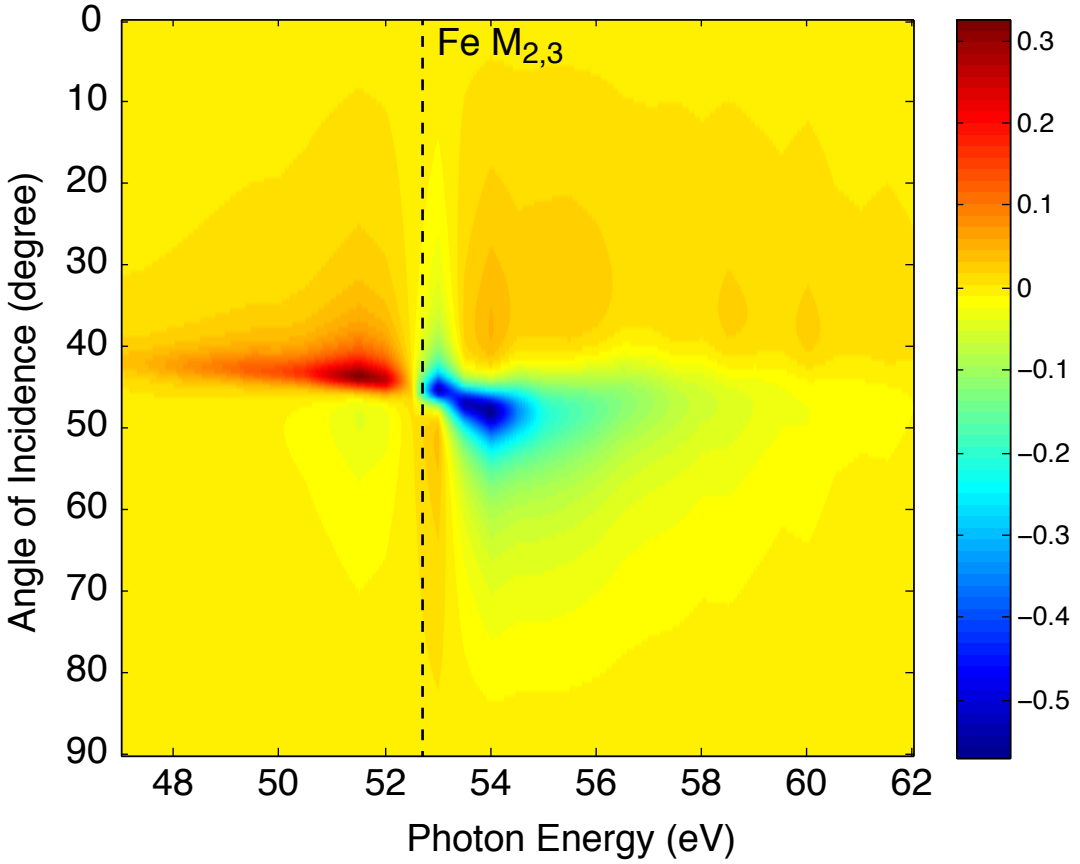

Figure 3.6: The calculated T-MOKE asymmetry of Fe as a function of energy and the angle of incidence (Equation 3.44). The asymmetry peaks near Brewster angle ($\sim 45°$) and the M-edges photon energy. The material parameters are from the Reference [12, 13] and Figure 3.2. Angle at 0° is defined at the normal incidence. Color scale is shown on the right hand.

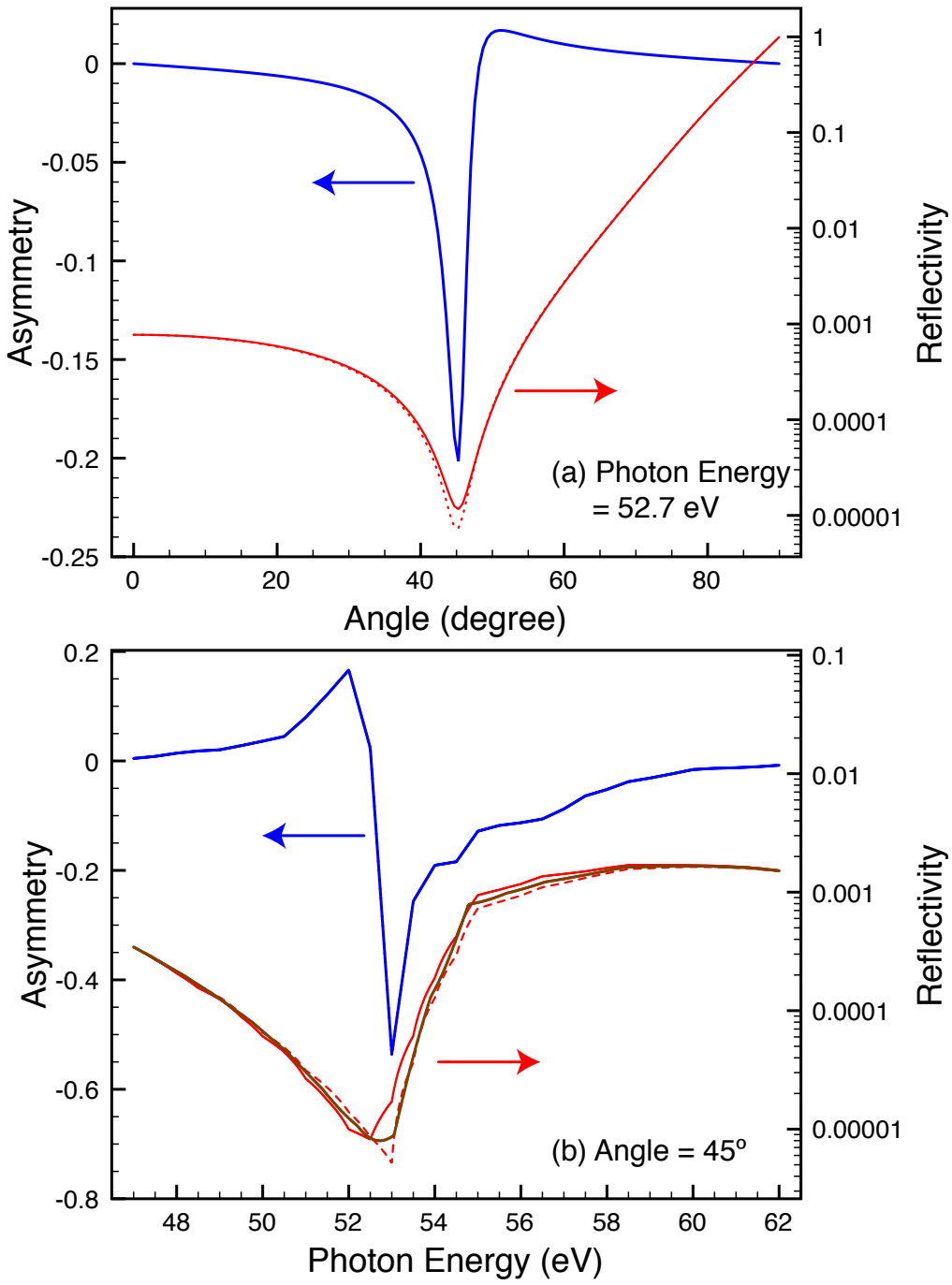

Figure 3.7: (Top) Asymmetry of Fe (blue) as function of incident angle at the photon energy of 52.7 eV ($M_{2,3}$ edges). Maximum asymmetry of 20% is close to the Brewster angle near 45° when the reflectivity (red) is at the minimum. Both reflectivities after switching magnetization are shown as line and dashed line. (Bottom) Asymmetry of Fe as a function of photon energy near M-edges. The reflectivity calculated from an x-ray database [13] is also plotted (brown) to show the non-magnetic contribution.

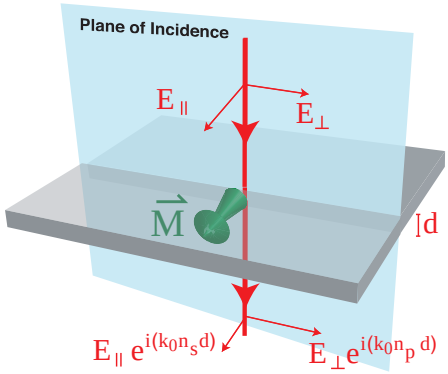

Figure 3.8: Magnetic linear dichroism geometry. The refractive index of linear polarized light transmitted through the in-plane magnetized sample with thickness d is dependent on the relative orientation between the magnetization vector and the polarization where $n_p = \sqrt{\epsilon + \frac{\epsilon'^2}{\epsilon}}$ and $n_s = \sqrt{\epsilon}$, for perpendicular and parallel polarization, respectively. The difference in refractive index results in the polarization-dependent contrast of absorption.

3.4 Magnetic Linear Dichroism

Another magneto-optical effect directly related to T-MOKE is magnetic linear dichroism (MLD). The effect describes the quadratically dependent of the absorption on the in-plane magnetization, and only the component of polarization that is normal to magnetization has the magnetic contribution.

We start the analysis by setting up the geometry in the same way as T-MOKE with at normal incidence ($\theta = 0$) to simplify the math (Figure 3.8). At normal incidence, the two reflective indexes of magnetic materials are still $n_s = \sqrt{\epsilon}$ and $n_p = \sqrt{\epsilon + \frac{\epsilon'^2}{\epsilon}} \approx \sqrt{\epsilon} + \frac{\epsilon'^2}{2\epsilon^{\frac{3}{2}}}$ (Equation 3.18). The former applies when the polarization is parallel to magnetization, while the latter is for the perpendicular case which is quadratically dependent on magnetic constant ϵ'.

Magnetic linear dichroism is the effect based on transmission geometry. Therefore, we have to consider an equation that describes intensity attenuation after light transmitting through a material. Since the imaginary part of the refractive index is re-

sponsible for the absorption (Equation 3.6), the transmitted intensity[6] after the sample thickness d for light at wavelength λ is

$$\begin{aligned} \frac{I}{I_0} &= \frac{|E|^2}{|E_0|^2} \\ &= e^{-2k_0\Im[n]d} \approx 1 - 4\frac{\pi}{\lambda}\Im[n]d. \end{aligned} \tag{3.47}$$

Magnetic linear dichroism originates from the contrast in this transmitted intensity of light when light polarization is parallel and perpendicular to the magnetization, or

$$\frac{I}{I_{0\perp}} - \frac{I}{I_{0\parallel}} = e^{-2k_0\Im[n_p]d} - e^{-2k_0\Im[n_s]d} \tag{3.48}$$

$$\approx \frac{2\pi d}{\lambda}\Im[\frac{\epsilon'^2}{\epsilon^{\frac{3}{2}}}]. \tag{3.49}$$

In the second line, I expand the expression up to the highest order in ϵ'. This expression suggests that magnetic linear dichroism is quadratic to magnetization. Therefore, only the rotation of magnetization by 90° causes the contrast but not the magnetization reversal, as in T-MOKE.

To get a good comparison of the magnetic contrast level between T-MOKE and magnetic linear dichroism, I define 'MLD asymmetry', A_{MLD}:

$$A_{MLD} = \frac{\frac{I}{I_{0\perp}} - \frac{I}{I_{0\parallel}}}{\frac{I}{I_{0\perp}} + \frac{I}{I_{0\parallel}}}. \tag{3.50}$$

I calculate magnetic linear dichroism asymmetry for 50 nm thick Fe film for the photon energy range around Fe M-edges (Figure 3.9). The contrast is very small (10^{-2}%) comparing to T-MOKE which is understandable from the quadratically dependent of the magnetic constant (ϵ'^2). The low contrast level and strong absorption at M-edges make magnetic linear dichroism very challenging for any experiments. Applications are more practical at L-edges with soft x-rays [100, 101] because of the magnetic contrast level and the transmission are an order of magnitude larger than those of M-edges.

[6] At normal incidence, the transmittance, T, are interchangeable with the absorbtion, Abs, since the reflectivity is negligible at that angle (Equation 3.38, 3.39) and $T = 1 - Abs$

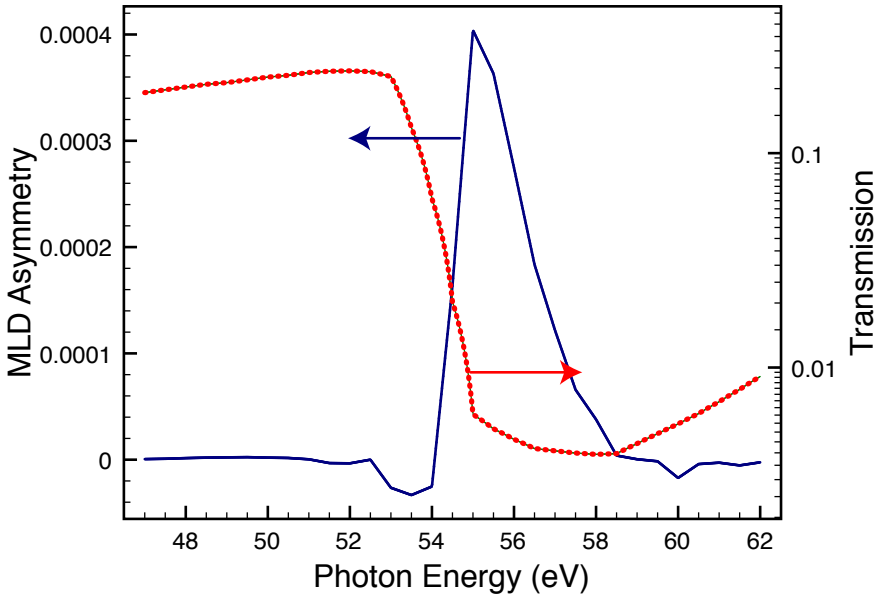

Figure 3.9: Magnetic linear dichroism asymmetry of 50 nm thick Fe film for the photon energy around M-shell absorption edges at normal incidence (dark blue). The contrast is very small (0.03%). The light transmissions of both parallel and perpendicular polarization (red and red dotted lines) range from 1 to 10%, but the different between them are too small to see in this graph scale.

3.5 Magnetic Circular Dichroism (MCD)

In the previous two sections, we discuss two magneto-optical effects, T-MOKE and magnetic linear dichroism. In both cases, we consider the situation where magnetization aligns in the plane of the interface. In the following two sessions, I will describe magnetic circular dichroism and Faraday effect that assume out-of-plane magnetization.

Magnetic circular dichroism describes the differential absorption of the magnetized magnetic materials based on the helicity of the circular polarized light (left or right). The effect is linearly dependent on the magnetization; therefore, the switching of magnetization direction can as well cause the magnetic contrast by keeping the polarization state.

3.5.1 Macroscopic View

To derive the equation for magnetic circular dichroism contrast, I employ the same lines of reasoning as T-MOKE. I define to coordinate such that the out-of-plane magnetization is along the z direction, and light is at the normal incidence (Figure 3.10). Therefore, the wave vector ($\mathbf{k}_T$) is

$$\mathbf{k}_T = (0, 0, k). \tag{3.51}$$

With the substitution of this wave vector into Maxwell's equation (Equation 3.12), the refractive index for magnetic circular dichroism can be found from the determinant of the matrix equation. The two refractive indexes are

$$n_1 = \sqrt{\epsilon + \epsilon'} \tag{3.52}$$

$$n_2 = \sqrt{\epsilon - \epsilon'}, \tag{3.53}$$

where eigenvectors for this geometry are circular polarization bases,

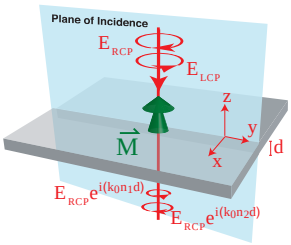

Figure 3.10: The geometry of magnetic circular dichroism. The magnetization is oriented out-of-plane, while the incident angle is set to the normal incidence. The magnetization is set to point along the z direction. The differential absorption arises between the left- and right-circular polarized light because of the dependent of refractive index on the polarization helicity: $n_1 = \sqrt{\epsilon + \epsilon'}$, $n_2 = \sqrt{\epsilon - \epsilon'}$.

$$\mathbf{e}_1 = \frac{1}{\sqrt{2}} \begin{pmatrix} 1 \\ -i \\ 0 \end{pmatrix} \tag{3.54}$$

$$\mathbf{e}_2 = \frac{1}{\sqrt{2}} \begin{pmatrix} 1 \\ i \\ 0 \end{pmatrix}. \tag{3.55}$$

The results indicates that the refractive indexes depend on the helicity of the incident circular-polarized beam. By repeating the same steps as in magnetic linear dichroism, the contrast from the differential absorption of left- and right-handed circular polarized light is

$$\begin{aligned} \frac{I}{I_0}_{LCP} - \frac{I}{I_0}_{RCP} &= e^{-2k_0 \Im[n_1]d} - e^{-2k_0 \Im[n_2]d} \\ &\approx 4\frac{\pi d}{\lambda} \Im[\frac{\epsilon'}{\sqrt{\epsilon}}], \end{aligned} \tag{3.56}$$

where d is the sample thickness, λ is the wavelength of circular polarized light. This expression indicates that magnetic circular dichroism is linear in magnetization and the contrast reverses the sign when the magnetization is at the opposite direction.

Similarly to the case of T-MOKE and magnetic linear dichroism, I define magnetic circular dichroism asymmetry A_{MCD} as

$$A_{MCD} = \frac{\frac{I}{I_0}_{LCP} - \frac{I}{I_0}_{RCP}}{\frac{I}{I_0}_{LCP} + \frac{I}{I_0}_{RCP}}. \tag{3.57}$$

Magnetic circular dichroism gives a significant contrast level of 8% for 50 nm Fe film, which is two orders of magnitude larger than magnetic linear dichroism, considered in the previous section. The significant contrast is due to the linearly dependence on the magnetic constant ϵ' (Equation 3.57). By increasing the thickness of the magnetic material, the contrast level is also improved. However, as a drawback, the transmission through sample is also exponentially reduced by material thickness (Figure 3.12).

3.5.2 Microscopic View

Magnetic circular dichroism can be described by an alternative approach that is related to the microscopic picture of band structures. For ferromagnetic elements, energy band can be splitted into two for spin up and down, known as the Stoner's picture. The 3d valence bands are slightly shifted with respect to each other by the exchange coupling. This exchange splitting is one of the fundamental mechanism for ferromagnetism. If the Fermi level, the highest energy level for electrons to occupied, is located in the spin-split valence band, the total number spins up and down become unequal resulting in some levels of spin polarization. This different in the number of spin up and down in the valence band is directly related to the magnetic moment.

When a material absorbs a circular polarized photon exactly at the M-edge, an electron from the core 3p levels is also excited to the valence 3d band. Since this excitation is spin selective as constrained by the selection rules, only one spin state can be excited depending on the helicity of the circular polarization. By this spin selective excitation and the exchange splitting of the valence band, the excitation probabilities,

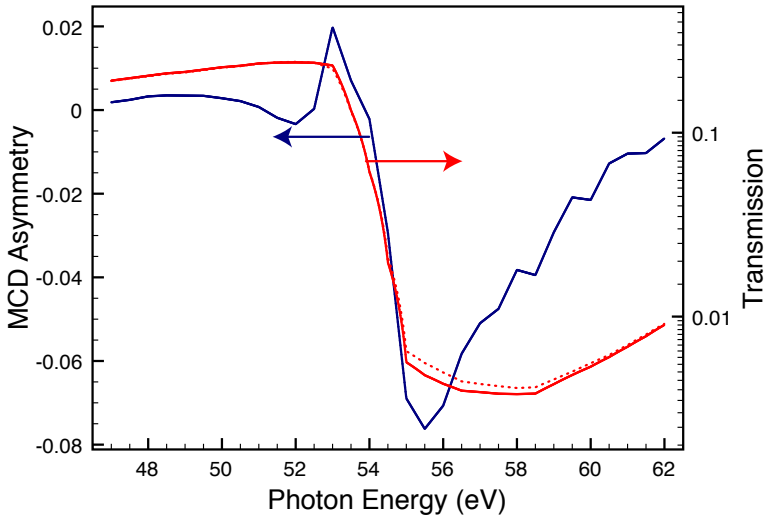

Figure 3.11: Magnetic circular dichroism asymmetry of 50-nm-thick Fe film as a function of photon energy around M-edges at normal incidence (dark blue). The maximum contrast near M-shell absorption edge is about 6%. This contrast level is two orders of magnitude greater to that of magnetic linear dichroism (Figure 3.9). The transmission of polarization left- (red lines) and right- (red dotted lines) circular-polarized light are in the range of 1–10%.

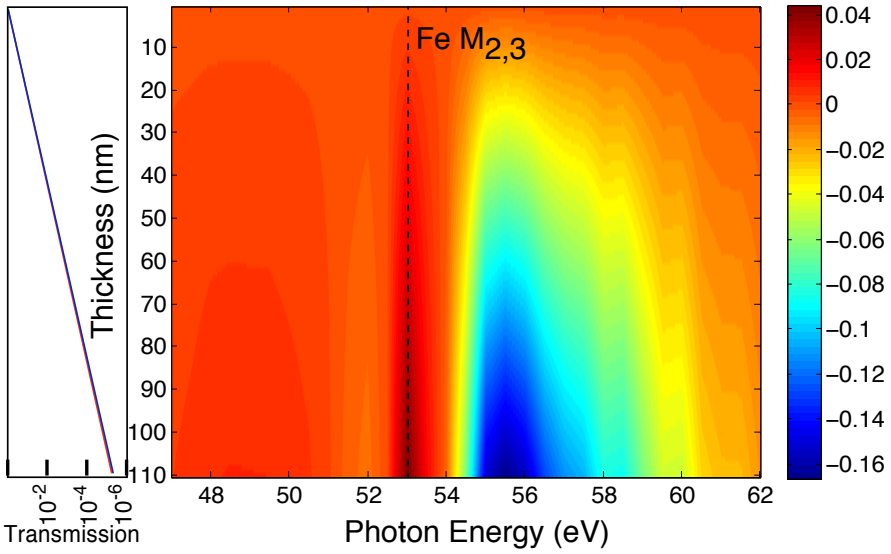

Figure 3.12: Magnetic circular dichroism asymmetry of Fe as a function of the material thickness and photon energy around M-edges at normal incidence. The asymmetry increases with the thickness, but the transmission also exponentially reduces. Fe $M_{2,3}$ are labelled with a vertical dashed line. The transmission of light at the photon energies giving the highest asymmetries is shown on the left axis.

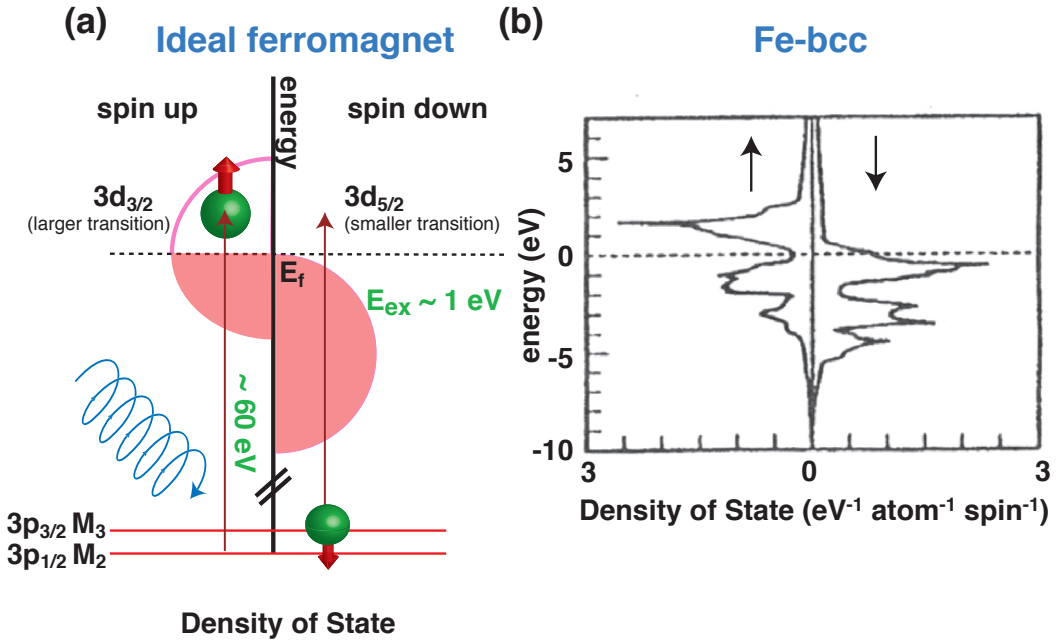

Figure 3.13: (a) A simplified ferromagnetic band structure is composed of the spin-up (left) and spin-down bands (right). Electrons fill these levels (pink area) up to the Fermi level (dotted line). In this case, more electrons are in the spin-down states because the spin-down band is lower in energy by an exchange energy (E_{ex}). If the material absorbs a circular polarized photon at the M_3 edges, a $3p_{\frac{1}{2}}$ core electron (green spheres) is excited to the unoccupied levels in 3d bands (white area). The transition is spin conservative; therefore, an electron can only be excited to the same spin state. In this simplifed picture, the spin-up down electron cannot be excited to the valence because empty states are not available. The contrast in electronic excitation probabilities of left- and right-circular polarized photons results in the contrast in light absorption, which is the origin of magnetic circular dichroism. (b) I simplify the band structure to semicircles and place the Fermi level such that the spin-down band is fully occupied. The real band structure of Fe is more complicated [14].

which are directly related to the absorption, are different for left- and right-circular polarization. This mechanism causes the magnetic circular dichroism.

3.6 Faraday Effect

Another magneto-optical effect that is closely related to magnetic circular dichroism is Faraday effect. Faraday effect involves with the rotation of the plane of linearly polarized light induced by magnetization. The angle of rotation is linear in the magnetization. The physics behind the Faraday effect is identical to magnetic circular dichroism discussed in the previous section. Since linearly polarized light can be decomposed into the sum of left- and right-circular polarized light, each of the components will experience a different refractive index as it propagates through a magnetic material. As a result, the two circular polarization bases have a different phase retardation, and the final transmitted light ends up having a rotated polarization.

To understand the above mechanism mathematically, I use the same coordinate system as in the previous section (Figure 3.10). The incident light polarization is at the angle ϕ with respect to the x axis,

$$\mathbf{E}_I = E_{I0} \begin{pmatrix} \cos\phi \\ \sin\phi \\ 0 \end{pmatrix}. \tag{3.58}$$

This linearly polarization is then written as a liner combination of left and right-circular polarization bases (Equation 3.54, 3.55),

$$\mathbf{E}_I = E_{I0}(\frac{e^{i\phi}}{\sqrt{2}}\mathbf{e_1} + \frac{e^{-i\phi}}{\sqrt{2}}\mathbf{e_2}). \tag{3.59}$$

After transmitting through the material, the two bases contain difference phase factors, and the final wave equation becomes

$$\mathbf{E}_T = E_{I0}(\frac{e^{i(\phi+k_0\sqrt{\epsilon+\epsilon'}d)}}{\sqrt{2}}\mathbf{e_1} + \frac{e^{-i(\phi-k_0\sqrt{\epsilon-\epsilon'}d)}}{\sqrt{2}}\mathbf{e_2}). \tag{3.60}$$

The equation can be written in a more symmetric form as

$$\mathbf{E}_T = E_{I0} e^{ik_0 \hat{n} d} \begin{pmatrix} \cos\frac{\delta}{2} \\ \sin\frac{\delta}{2} \\ 0 \end{pmatrix}, \tag{3.61}$$

where $\hat{n} = \frac{\sqrt{\epsilon+\epsilon'}+\sqrt{\epsilon-\epsilon'}}{2}$ and $\delta = 2\phi + k_0(\sqrt{\epsilon+\epsilon'} - \sqrt{\epsilon-\epsilon'})d$.

This result indicates that the polarization angle rotates from ϕ to $\phi + k_0 \frac{\sqrt{\epsilon+\epsilon'}-\sqrt{\epsilon-\epsilon'})d}{2}$. However, the polarization rotation is not the only effect on the incident light because the term $\sqrt{\epsilon+\epsilon'} - \sqrt{\epsilon-\epsilon'} \approx \frac{\epsilon'}{\sqrt{\epsilon}}$ is in general a complex number. Magnetization also induces some degree of ellipticity into the linearly polarized light. The two polarization effects can be decomposed into two parts by the equation $\Delta\phi = \varphi_F + i \tan\varepsilon_F$,

$$\varphi_F = \frac{\pi d}{\lambda} \Re[\frac{\epsilon'}{\sqrt{\epsilon}}] \tag{3.62}$$

$$\tan\varepsilon_F = \frac{\pi d}{\lambda} \Im[\frac{\epsilon'}{\sqrt{\epsilon}}]. \tag{3.63}$$

by taking the limit of $\epsilon \gg \epsilon'$ [106, 107].

I calculate the Faraday rotation constant, defined as the rotated angle per thickness of sample ($k = \frac{\Delta\phi}{d}$), which is approximately 6,000 degrees per millimeter (Figure 3.14). This number agrees with the measurement at M-edges with a synchrotron[106].

3.7 Conclusions

In this sections, I derive the contrast conditions for four magnetic-optical effects: transverse magnetic-optical Kerr effect, magnetic linear dichroism, magnetic circular dichriosm and Faraday effect. All of the derivations start with the same permitivity tensor (Equation 3.1) and the empirical magnetic constant ϵ' of iron [12]. Among these effects, T-MOKE gives the highest contrast up to 55% asymmetry with the probe photon energy near M-edges and at the angle of incidence of 45°. When the material thicknesses is set such that the transmission matches with T-MOKE reflectivity at

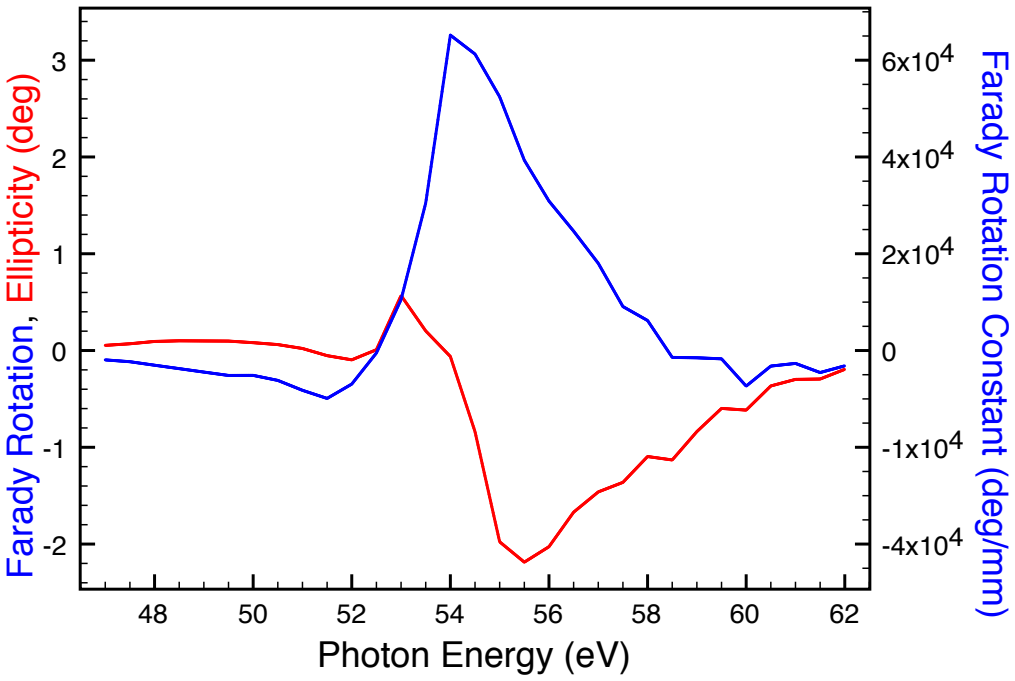

Figure 3.14: Faraday rotation angle (blue) and ellipticity (red) as a function of photon energy around M-edges of Fe (50 nm thick at normal incidence). The Faraday rotation constant defined as the rotated polarization angle per material thickness (blue) is displayed on the right axis.

Brewster angle, magnetic circular dichroism allows for less contrast at 16% between the absorption of left- and right-circular polarized light (3.12). Finally, magnetic linear dichroism gives the least asymmetry at 0.09% between the absorption of light with parallel and perpendicular polarization to magnetization[7] .

These calculations suggest that T-MOKE is an ideal geometry for high-harmonic experiments at extreme ultraviolet region since T-MOKE (1) gives the highest magnetic contrast level, (2) requires only a linearly polarized light source, and (3) does not need any polarization analysis techniques. Later on in this thesis, T-MOKE is used to probe the demagnetization dynamics, which is the subject of the next chapter.

[7] Faraday effect is excluded from this comparison since the contrast is not related to the intensity change.

Chapter 4

Laser-induced Ultrafast Demagnetization Dynamics

4.1 Introduction

In the previous two chapters, I discussed high-harmonic generation and magneto-optical effects for the probing of magnetic materials. By combining the two techniques, our research group studies laser-induced demagnetization dynamics, which is one of the most exciting fields in modern magnetism. The reports of many experimental studies indicate that the magnetization, as inferred from magneto-optical contrast, is reduced within a few hundreds of femtoseconds after a laser excitation. This surprisingly fast demagnetization opens up many questions such as: What are the fundamental physics behind the abrupt change of magnetization? What contributes to the demagnetization speeds? Is a few hundreds femtoseconds already the fastest possible time dynamics? What are the roles of microscopic quasi-particle entities (electrons, photons, phonons, spins, and magnons)? And, what are the dynamics in the case of nanoscale magnetic structures? Finding the answers to these questions may eventually result in our ability to control the dynamics of nanomagnets at the femtosecond time scale.

Historically, the first report of ultrafast demagnetization was in 1996 [9]. Beaurepaire et al. demonstrated that the Kerr-effect contrast of nickel is quickly reduced within 1-2 ps after the excitation a laser pulse. This result brought a great excitement to the research community since the demagnetization time is faster than the timescale of the spin-lattice relaxation approximately at 100 ps [118], which was thought to be

the fastest limit of any magnetization dynamics. Not too long after its first discovery, the ultrafast demagnetization dynamics were repeated by many experimental groups [119, 120, 121, 122, 123, 124].

Today, the field of ultrafast magnetization dynamics has been expanded greatly. The dynamics were studied in many magnetic materials such as multilayers [125], exchange-biased layers [126, 127], half metals [128], semiconductors [129], ferrimagnets [130], and Heusler materials [131]. Bigot et. al. proposed the occurrence of coherent magnetization dynamics, in which the phase of spins and the laser field are strongly correlated during the laser pulse [10]. The advancement of short-pulse x-ray technologies allows for the probing the demagnetization dynamics with soft x-ray pulses. Many exciting results were reported from this new technique [41, 132, 16, 130]. Finally, the field of ultrafast magnetization dynamics had spawned many new areas of research such as all-optical switching of magnetization [39], laser-induced ferromagnetic resonance [40], and terahertz emission during the demagnetization [42].

4.2 Electron-Lattice-Spin Dynamics

From a theoretical point of view, we can understand the ultrafast magnetization dynamics by separating magnetic systems into three subsystems of the electrons, spins and lattice. The three systems have different roles at different time scales during the course of dynamics. Electrons react directly with a laser pulse. The occupied electrons below Fermi level are optically excited to the unoccupied levels with the energy equal to the laser photon energy (~ 1.5 eV). After the initial exception, the temperature becomes well-defined only after electrons equilibrate by the electron-electron scattering process into a thermal energy distribution among electrons. The electron temperature can be inferred from the shape of the electronic distribution, which is of the Fermi-Dirac type.

Although the electrons are at thermodynamic equilibrium with respect to each other, comparing to spins and lattices, they are not. To cool down, electrons interact

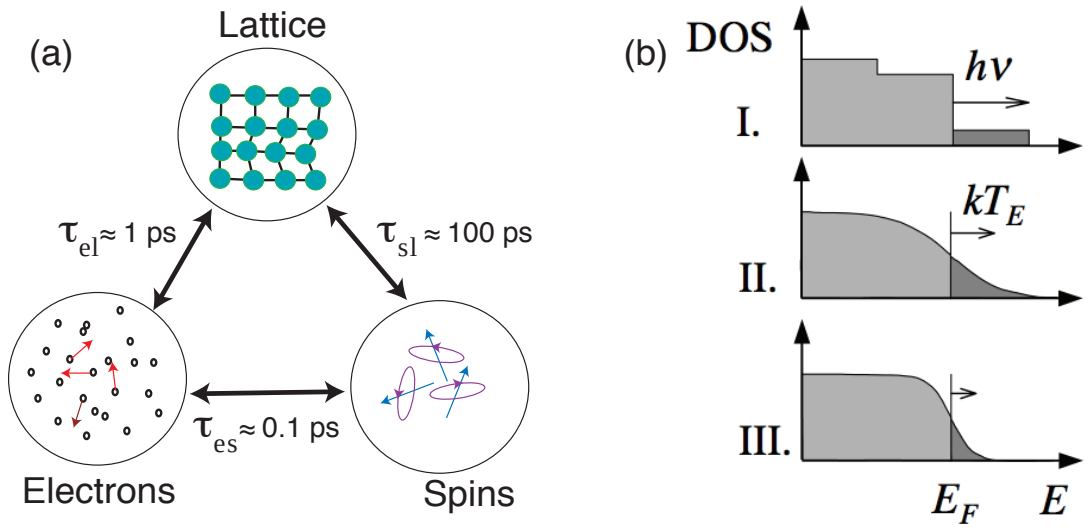

Figure 4.1: (a) The three-temperature model presumes that magnetic materials can be broken up into three separate thermal reservoirs: electrons, spins, and lattice. All reservoirs interact with one another with the indicated time scales. (b) Electronic density of states after pumping by a laser pulse: (I) non-equilibrium distribution right after an optical excitation, (II) thermalized 'hot' electron distribution, and (III) the distribution after scattering processes with lattice or spins to cool down the electron temperature. Figure from [15].

with the lattice through electron-phonon scattering that occurs on a time scale called the **electron-lattice relaxation time** (τ_{el}), which is on the order of picoseconds. The electron kinetic degree of freedom also interacts with the spin degree of freedom. However, the microscopic model leading to this process is still unclear. Although it is generally understood that the spin-orbit coupling is ultimately responsible for such processes. Since magnetization is the macroscopic manifestation of spins, the demagnetization time is a good estimate for the **electron-spin relaxation time** (τ_{es}) of a few hundred femtoseconds. Spins can also couple to the lattice system, but the **spin-lattice relaxation time** (τ_{sl}) is on the order of hundreds of picoseconds. Thus, the spin-lattice mechanism is too slow to account for the demagnetization dynamics. At the longer time scale of more than a nanosecond, the temperature of all systems reduces by transferring the excessive heat to other sources such as air or substrate to cool down all sub-systems to the initial states.

4.2.1 Three-temperature Model

The most simple mathematical model to describe the above picture is the three-temperature model [9]. The model considers the thermodynamics of the three sub-systems and assigns temperatures to each system, i.e. electron temperature (T_e), spin temperature (T_s) and lattice temperature (T_l), with the assumption that all temperatures are a well-defined at all times. This assumption breaks down specially at the initial part of the dynamics when the concept of electron temperature has not yet existed. In addition, the kinetic electronic and spin degrees of freedom are the so tightly coupled and correlated. It is hard to understand how each can be regarded as having different temperatures.

Three-temperature model is an extension of the two-temperature model, a standard method used to analyze ultrafast laser excitations in non-magnetic materials [133]. The two-temperature model accounts for the temperature dynamics of electrons

($T_e(\mathbf{r},t)$) and lattice ($T_l(\mathbf{r},t)$) with the interaction term between electrons and lattice system, $G_{el}(T_l - T_e)$:

$$\begin{aligned} C_e(T_e)\frac{\partial T_e}{\partial t} &= G_{el}(T_l - T_e) + P(\mathbf{r},t) \\ C_l(T_l)\frac{\partial T_l}{\partial t} &= G_{el}(T_e - T_l) - \kappa\nabla^2 T_l(\mathbf{r},t), \end{aligned} \tag{4.1}$$

where $C_{e(l)}$ is the heat capacity of electrons (lattice), $P(\mathbf{r},t)$ is the laser heating term, and $\kappa\nabla^2 T_l$ describes diffusion of heat via lattice. The extension to the three-temperature model incorporates spin temperature T_s and the additional coupling constants G_{es}, G_{sl}:

$$\begin{aligned} C_e(T_e)\frac{\partial T_e}{\partial t} &= G_{el}(T_l - T_e) + G_{es}(T_s - T_e) + P(\mathbf{r},t) \\ C_l(T_l)\frac{\partial T_l}{\partial t} &= G_{el}(T_e - T_l) + G_{sl}(T_s - T_l) - \kappa\nabla^2 T_l(\mathbf{r},t) \\ C_l(T_l)\frac{\partial T_s}{\partial t} &= G_{es}(T_e - T_s) + G_{sl}(T_l - T_s). \end{aligned} \tag{4.2}$$

The numerical solution to this system of equations predicts many characteristics of demagnetization dynamics such as the linearity between pump fluence and demagnetization amplitude at the low fluence limit. The detailed numerical calculation will be presented in Chapter 8 of this thesis. With some approximations, three-temperature model can be solved analytically[1] . The analytical solution to three-temperature model [17, 134] is

$$\frac{\Delta M}{M} = -\frac{A_2\tau_E - A_1\tau_M}{\tau_E - \tau_M}e^{-\frac{t}{\tau_M}} - \tau_E\frac{A_1 - A_2}{\tau_E - \tau_M}e^{-\frac{t}{\tau_E}} - A_3 e^{-\frac{t}{\tau_R}}, \tag{4.4}$$

where τ_M is the observed demagnetization time, τ_E is the magnetization recovery time and τ_R is the slow recovery time of magnetization to the original state. The analytical solution to the three-temperature model provides a general shape of demagnetization

[1] (1) At low fluence, heat capacity of spins is negligible. (2) Heat capacity of electrons and lattices are constant. (3) Spin dynamics follow the rate equation:

$$\frac{dT_s}{dt} = \frac{T_e - T_s}{\tau_{M,e}} + \frac{T_l - T_s}{\tau_{M,l}}, \tag{4.3}$$

where the observed demagnetization time contains the contribution from electrons and lattices: $\frac{1}{\tau_M} = \frac{1}{\tau_{M,e}} + \frac{1}{\tau_{M,l}}$. (4) Magnetization is linear in spin temperature.

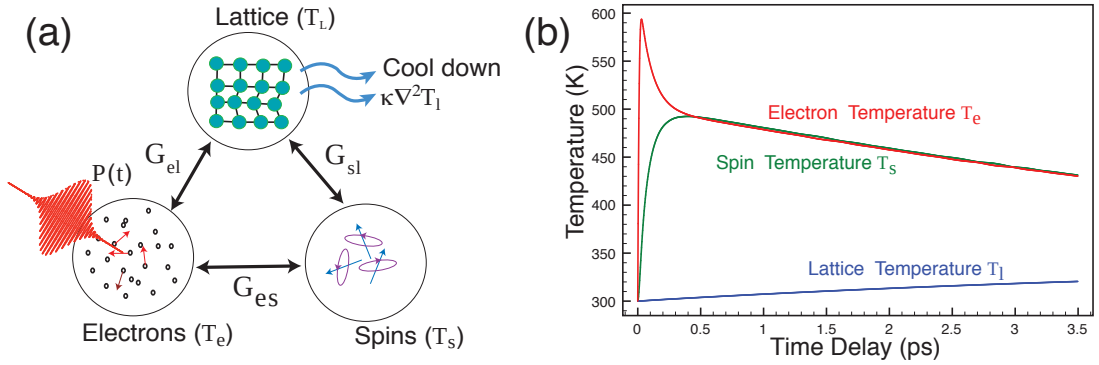

Figure 4.2: Three-temperature model. (a) The electronic system is first excited by a laser pulse, $P(t)$. The 'hot' electrons then cool down by transferring energy to lattice and spin system with coupling constant G_{el} and G_{es}. Spin and lattice can couple together with the coupling constant G_{sl}. Finally, the temperatures of all three subsystems reduce to ambient temperature through heat transportations $\kappa\nabla^2 T_l$. (b) The numerical solution of three-temperature model in nickel with the pump fluence of 2.5 mJ/cm^2.

dynamics and explains why exponential equations can describe phenomenologically the experimental demagnetization data.

4.2.2 Microscopic Models

The basic physics by three-temperature model does not consider any microscopic pictures of electron, spin and lattice dynamics. A complete theory to describe laser induced demagnetization must include the scattering processes between all involved fundamental entitles. Such information is still missing from our current understanding of the ultrafast demagnetization dynamics.

To my knowledge, one of the most controversial mechanisms to describe the laser-induced demagnetization dynamics is based on electron-phonon scattering accompanied by a spin flip. The mechanism is related to the Elliot-Yafet mechanism process [135, 136] that describes the enhancement of the spin-flip probability by an electron-scattering process. Because of the spin-orbit coupling, the two electronic spin states ($|\uparrow\rangle, |\downarrow\rangle$) are no longer good quantum numbers, and the states are the linear combination of both spins. An electron-electron scattering due to phonons or impurities can cause the flipping of the spins. Koopmans et al. choose the absorption and emission of a phonon to conserve the local angular momentum [137, 138, 21]. The model provides the relaxation channel for spins such that the magnetization time can be quenched within the timescale of electron-lattice relaxation ($\sim$ ps) [137]. If such a fast relaxation channel does not exist, spins can only relax through the spin-lattice relaxation channel which is slow ($\sim$ ns).

By having such a microscopic picture, many dynamical behaviors after the excitation by a laser pulse has been predicted.

4.2.2.1 Damping-Constant-Dependence of the Demagnetization Time

Koopmans et al. [137] solved for the demagnetization time as a function of two measurable parameters, Gilbert damping constant (α), and Curie temperature (T_c) [137]:

$$\tau_M = F(\frac{T}{T_c})\frac{1}{4}\frac{\hbar}{k_B T_C}\frac{1}{\alpha}, \tag{4.5}$$

where the pre-factor ($F(\frac{T}{T_c})$) is the temperature dependent function and equals to unity at the low fluence limit.

The formula above predicts the demagnetization time of 425 fs for Permalloy[2] which is in the right order of our observed value (τ_M = 197 fs). Several experimental groups attempted to verify this trend of demagnetization time by studying a series of Permalloy samples with different types of rare-earth doping to modify the damping constants (Ho, Dy, Tb and Gb [139], Pd and Dy [140]). Unfortunately, this simple equation of demagnetization time (Equation 4.5) failed to predict the variation of demagnetization time with the damping constant and Curie temperature. In Reference [140], the authors concluded that the band structures from rare-earth metals are too localized. The rare earths only contribute in slow dynamics involving damping constants but not in fast dynamics involving demagnetization. These results suggested that damping constant cannot be related to the demagnetization time in a straightforward manner as in Equation 4.5 for rare-earth–doped Permalloy. Further studies on transition-metal–doped alloys should be considered.

4.2.2.2 Two Types of Demagnetization Dynamics

Koopmans et al. combined the three-temperature model with the Elliot-Yafet mechanism [21] to construct a more complete model for demagnetization dynamics. They predicted that the demagnetization dynamics can be described into two catagories:

[2] $\alpha = 0.005, T_c = 853$

type I and II dynamics. In type I dynamics, the demagnetization (electron-spin relaxation channel) happens faster ($\tau_M \approx 0.1ps$) than the electron-lattice relaxation time ($\tau_{el} \approx ps$). Transition ferromagnetic metals (Fe, Co, and Ni) have this behavior at the room temperature. In contrast, type II occurs when the spin-flip scattering has a poor efficiency. As a result, the demagnetization time ($\tau_M > ps$) is slower than the electron-lattice relaxation time. Since electrons and spins are not yet under equilibrium before the complete demagnetization, magnetization can still reduce even further at longer time delay, which results in two-step demagnetization dynamics. The type II dynamics are predicted in rare-earth metal (Gd) and transition metals (Fe, Co, and Ni) near the Curie temperature. The model explains the long demagnetization time for Gd [118].

The figure-of-merit to separate between the two types of dynamics is given by the ratio $\frac{T_c}{\mu_{at}}$, where T_c is Curie temperature and μ_{at} is local magnetic moments per atom, which controls the spin-flip scattering efficiency.

4.2.2.3 Angular Momentum Consideration

The motivation of the Elliot-Yafet mechanism is due to the conservation of angular momentum. Since magnetization also contains angular momentum, the angular momentum must go somewhere after the demagnetization. And the total angular momentum from all reservoirs (magnetization, lattice, phonons),

$$\mathbf{L_{tot}} = \mathbf{L} + \mathbf{S} + \mathbf{L}_{lattice} + \mathbf{L}_{photon}, \tag{4.6}$$

must be conserved all the time including during the ultrafast time scale. The first two terms contribute from magnetic moment, which is the microscopic parameter to magnetization. The magnetic moment is composed of orbital and spin moments, $\mu = \mu_B(\mathbf{L} + 2\mathbf{S})$.

The microscopic picture described by the Elliot-Yafet mechanism conserves the angular momentum by assigning the lattice system as the final angular momentum

"sink". This observation is supported by two experiments. (1) Time-resolved XMCD measurement suggested that both **L** and **S** are not the angular-momentum sinks because both parameters are quenched during the demagnetization dynamics [16]. (2) The photon angular momentum is not involved in the dynamics [17] (Figure 4.3). From this evidence, the only remaining angular momentum "bath" is the lattice, which is assumed in the Elliot-Yafet mechanism. This angular-momentum transfer to the lattice can be thought of as an ultrafast version of Einstein-de Haas experiment [141], which is the observation of a mechanical rotation of bulk solids after switching the magnetization.

Other than considering the Elliot-Yafet scattering process, some alternative theories are available. For example, electron-electron scattering mechanism alone can reproduce the demagnetization dynamics [142]. In this model, only Coulomb scattering and spin-orbit coupling are considered. The driving force for the demagnetization is the scattering between majority and minority bands. This model is in line with the past theoretical result suggesting that only requirements for demagnetization dynamics are the laser field and spin-orbit coupling [143]. Experimental data of Co, Ni [142], and Heusler alloy [131] were reproduced by this mechanism.

More available microscopic models are spin-flip scattering mediated by magnons [144] and sp-d model to describe the demagnetization in semiconductors [145].

4.2.3 Thermal Mechanism: the Landau-Lifshitz-Bloch equation

Instead of considering microscopic scattering processes as the basic physics of demagnetization dynamics, the explanation of ultrafast magnetization dynamics can take another route by a phenomenological 'equation of motion' to solve for the magnetization as a function of time. The equation is directly related to Landau-Lifshitz-Gilbert equation, which is a standard equation to describe magnetization precession dynamics,

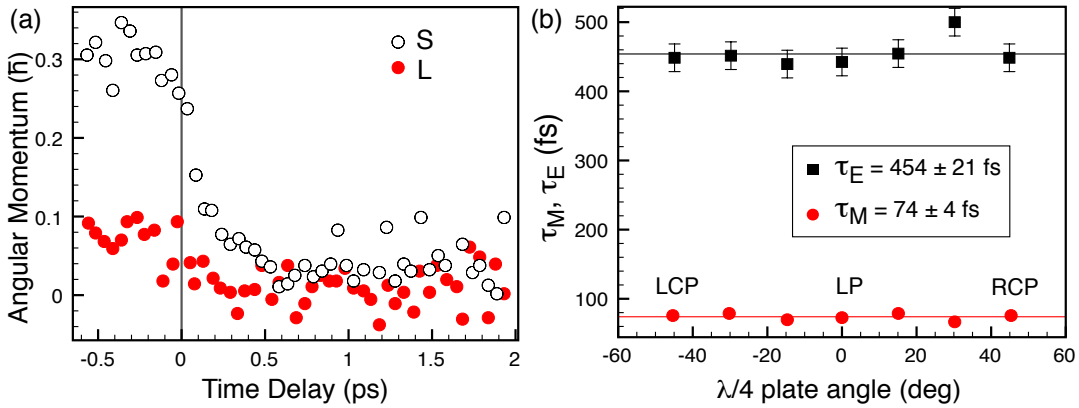

Figure 4.3: Angular momentum distribution during ultrafast demagnetization dynamics. (a) Both spin (**S**) and oribital (**L**) angular momentum are both quenched during the ultrafast demagnetization. These angular momentums are measured from x-ray magnetic circular dichroism sum rules. (b) Angular momentum of pump pulses, controlled by the degree of circular polarization, does not contribute to demagnetization dynamics. The demagnetization time (τ_M) and recovery time (τ_E) are independent from the pump circular polarization. Both results indicate that lattice is the final angular-momentum sink. Reproduced from Reference [16], [17].

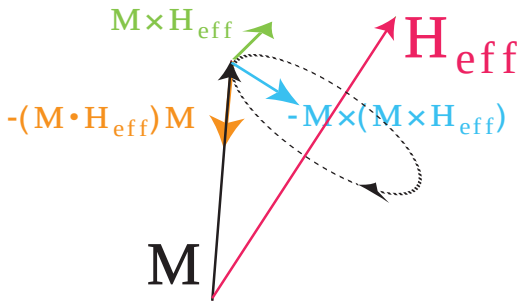

Figure 4.4: All possible torques that cause the magnetization dynamics governed by Landau-Lifshitz-Bloch equation. The precession term (green) drives magnetization (black) to precess around the effective magnetic field, $\mathbf{H}_{eff}$ (red). The damping term (blue) reduces the radius of precession and aligns the magnetization toward the field. The longitudinal relaxation term (orange) causes the demagnetization.

$\mathbf{M}(t)$:

$$\frac{d\mathbf{M}}{dt} = -\gamma \mathbf{M} \times \mathbf{H}_{eff} - \frac{\gamma\alpha}{M^2}\mathbf{M} \times (\mathbf{M} \times \mathbf{H}_{eff}), \tag{4.7}$$

where γ is the gyromagnetic constant and $\mathbf{H}_{eff}$ is the effective magnetic field contributed by applied, anisotropy, and dipolar magnetic fields. The first term describes the magnetization precession around the effective field, $\mathbf{H}_{eff}$. The second term accounts for the damping of the magnetization toward the field by introducing a phenomenological damping parameter α. If the second term did not exist, the magnetization would precess forever, and we could not reverse magnetization by any external magnetic field. Since demagnetization dynamics are too fast for the precession dynamics ($\approx \frac{1}{GHz} = $ ns), the Landau-Lifshitz-Gilbert equation above cannot account for the demagnetization in femtosecond time scales.

A modification to Landau-Lifshitz-Gilbert equation has been made to generalize the equation at elevated temperatures. At higher temperature, a fluctuation of the local fields on each atom becomes important [146]. Such a microscopic fluctuation leads to the Landau-Lifshitz-Bloch equation [147]:

$$\frac{d\mathbf{M}}{dt} = -\gamma \mathbf{M} \times \mathbf{H}_{eff} + \gamma \alpha_{\parallel} \frac{(\mathbf{M} \cdot \mathbf{H}_{eff})\mathbf{M}}{M^2} - \frac{\gamma \alpha_{\perp}}{M^2} \mathbf{M} \times (\mathbf{M} \times \mathbf{H}_{eff}). \tag{4.8}$$

The extra term, $((\mathbf{M} \cdot \mathbf{H}_{eff})\mathbf{M})$, describes relaxation **along** the direction of magnetization, which reduces the size of magnetization vector in the case of ultrafast demagnetization (Figure 4.4). The damping parameters, $\alpha_{\parallel}, \alpha_{\perp}$, and the field, $\mathbf{H}_{eff}$, become temperature dependent, which is the only input parameter for Landau-Lifshitz-Bloch equation. The authors of Reference [148, 149] reconstructed the demagnetization dynamics by using the electronic temperature as an input to the model. They concluded that demagnetization dynamics is driven by hot electrons. Another consequence from Landau-Lifshitz-Bloch dynamics, known as the critical slow-down, is the reduction of the magnetic relaxation times, i.e. $\alpha_{\parallel}$, when the temperature approaches the Curie temperature [150].

4.3 Conclusions

The understanding of ultrafast demagnetization dynamics induced by a laser pulse is challenging from both theoretical and experimental aspects. Theoretically, the complete explanation of the dynamics requires an understanding of the fundamental interactions between photons, electrons, spins and lattice at femtosecond time scales. Such a complete theory is not available today. Experimentally, the dynamics involves the fast probing of magnetization modulation. Short pulses are, therefore, required for pump-probe studies. Traditionally, demagnetization dynamics studies make use of laser pulses, which do not provide any element selectivity, and all of the available theoretical explanations considered do not consider this element-selective information either. In the rest of this thesis, I will present studies of ultrafast demagnetization dynamics with extreme-ultraviolet light pulses from high-harmonic generation that enable element-selective determination of demagnetization times.

Chapter 5

Laser-Pump–High-harmonic-Probe Experimental Setup

5.1 Introduction

In this chapter, I will provide an overview of the experimental setup for studying ultrafast demagnetization dynamics covered in the subsequent chapters. Important components of the experimental apparatus are the pump-probe beam paths (Section 5.2), samples and spectrometers (Section 5.3), magnets (Section 5.4), and the vacuum system (Section 5.5). The chapter concludes with the acquisition technique used to increase the signal-to-noise ratio of the data (Section 5.6).

5.2 High-Harmonic-Probe–and–Laser-Pump Geometry

The setup starts with a standard laser amplifier system to produce short pulses for high-harmonic generation and induce the demagnetization dynamics. The laser makes use of a chirped-pulse amplification technique [151] to amplify the average output power of 5 W at 2kHz repetition rate, equivalent to 2.5 mJ per pulse. The spectral bandwidth is 80-nm full width at half maximum with the center wavelength at 790 nm (Figure 5.1). The pulse duration is 25 fs measured by the frequency-resolved optical gating (FROG) technique [152].

The laser beam is sent to a beamsplitter to divide the beam into probe and pump arms. The probe arm requires more laser power (90%) because it involves high-harmonic generation, while we use the rest of the power (10%) to induce demagnetization

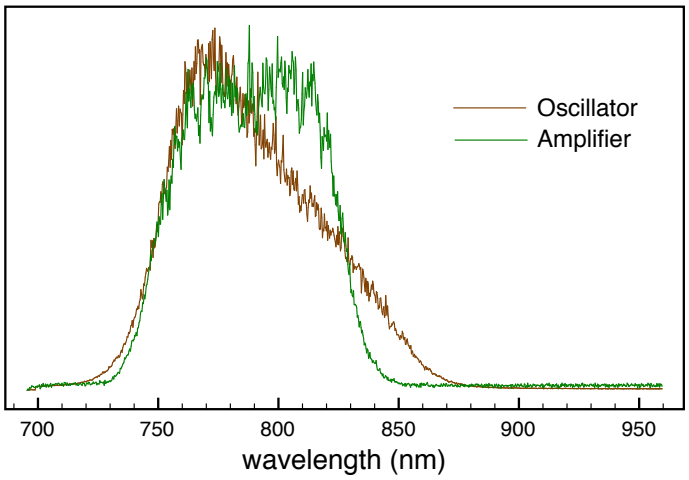

Figure 5.1: Output spectra from the Ti:sapphire oscillator and the chirped-pulse amplifier.

dynamics.

5.2.1 The Probe Arm: High-harmonic Generation

For high-harmonic generation, we couple the probe laser beam to a fused quartz 150-μm-diameter capillary (Wilmad-Labglass LN002 Q-0.150M-0-0-1Meter) with a 50-cm plano-convex lens that focuses the beam to the optimal size near 64.35 % of the capillary diameter [153]. We mount the lens on a translation stage to adjust the focal spot for the best coupling efficiency. We makes use of a v-groove fixture, described in detail in [154], to hold the capillary (Figure 5.3). The v-groove connects to the experimental chamber by custom-made tee adaptors.[1] We adjust the front and the back ends of the v-groove by use of two-dimensional translation stages. The optimal coupling to the capillary happens when the output beam is in an Airy pattern. To monitor the mode of the beam, we use a silver mirror to reflect the beam vertically through a viewport. We flow neon or argon, which are our high-harmonic generation

[1] A 1/2-inch stainless steel tee (316L-8TB7-3) welded to (1) a stainless steel tubing (to connect to the experiment, SS-8-UT-A-12BT), (2) a bored-through adapter to the 1/4 inch Ultra-torr fitting (to hold the v-groove, SS-4-UT-A-8BT) and (3) a bored-through adapter to the 1/2 inch Ultra-torr fitting (to connect to the vacuum pump)

media, into the capillary (controlled by MKS 640A13TW1VA2V) with the optimized pressure around 450 torr for Ne and 70 torr of Ar. For gas inlets in the original design, two holes with the separation of 5 cm are drilled through the outer diameter of the capillary. However, the high-harmonic flux is improved by introducing another hole next to one of the existing holes (Figure 5.2). This extra hole serves as the gas inlet, while we evacuate gas through the other two holes.

The residual laser beam also collinearly propagates along with the harmonics, and we need to get rid of the laser beam because high-harmonic intensity is always significantly weaker. We use a 200-nm-thick aluminum filter (Lebow) to block most of the laser light and transmit 70% of the extreme ultraviolet harmonics. The Al filters are protected in a filter wheel described in Reference [154]. A filter replacement during the pumping or venting of the vacuum chamber are very convenient with filter wheels.

Then, we send harmonics to a gold-coated toroidal mirror, which is our focusing optics. The toroidal mirror (ARW optical 50mm x 25 mm substrate R1= 3220 mm R2= 90.5 mm) focuses the beam onto the detector with a slight vertical astigmatism to improve the spectral resolution. As such, the high-harmonic beam at the sample is not at the focus. Nevertheless, the beam creates a spot size of 1 mm at the sample.

We use a CCD (charge coupled device) camera to detect high harmonics (Andor Newton DO920P-BN). The camera is a sensitive instrument to detect light in the range of extreme ultraviolet or soft x-rays (Figure 5.4). The CCD chip is cooled down to -60°c to reduce the thermal noise. The camera continuously acquires high-harmonic spectra in a kinetic-series mode, where sequences of exposures are made without transferring the spectra to a computer. The distance from the sample to CCD camera is set to 30 cm. Before the camera, two additional Al filters block the residual pump light when performing time-resolved experiments because every Al filter always contains many small pinholes that let the laser light transmit. And we need two filters to weaken the residual pump light through a filter.

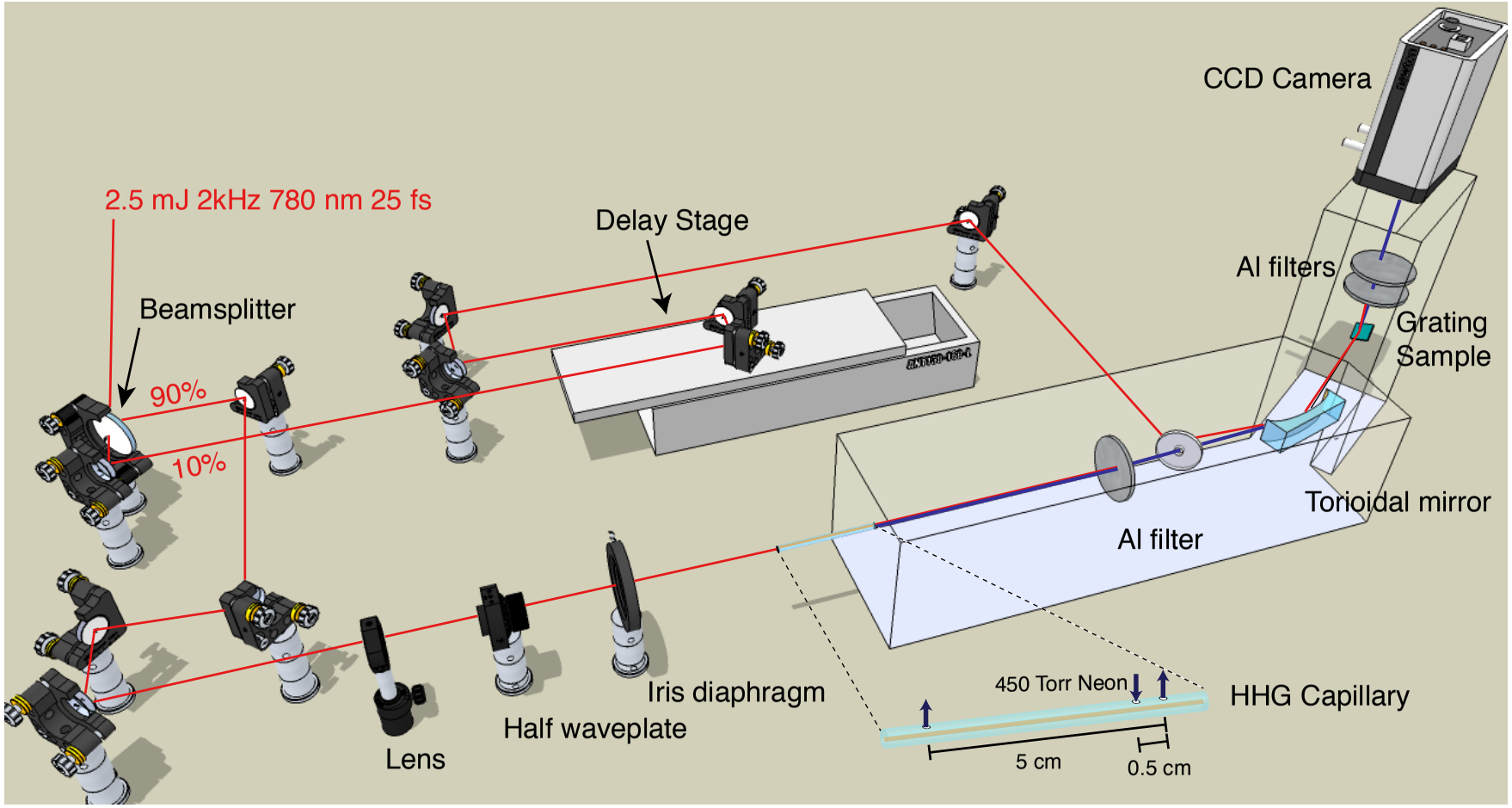

Figure 5.2: The optical beam path and experimental apparatus. High-harmonic generation (HHG) is achieved by focusing an intense laser beam into a capillary filled with neon or argon. We eliminate the residual laser light from high harmonics by an aluminum filter. Harmonics are then diffracted from a magnetic grating and detected by a charge-coupleddevice (CCD) camera to characterize the photon energy. Because of the strong absorption in extreme-ultraviolet region, experimental apparatus after HHG capillary must be kept in a vacuum system (transparent box). The optical models are from Reference [18].

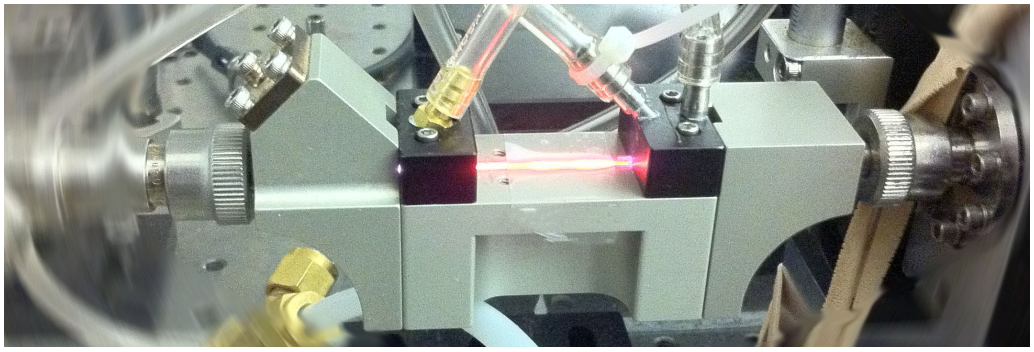

Figure 5.3: A photo of a v-groove fixture filled with orange plasma of Ne. The laser beam travels from the left.

We use a half-wave plate to control the polarization angle of the laser, which is the same polarization as high harmonics. In Chapter 3, I explained why we need p-polarized light to reflect from the sample to probe the magnetization. However, since s-polarized light always reflects more efficiently than p-polarization, we design the beam path such that the polarization of the incoming high harmonics is s-polarized (perpendicular to the optic table) with respect to the toroidal mirror to improve the reflectivity. Afterward, the sample is oriented perpendicular to the laser polarization to be in p-polarized geometry, hence the beam must reflect upward from the optics table after the sample (Figure 5.2, 5.5).

We put an iris diaphragm just behind the half-wave plate to control the intensity of the incoming beam. The energies of high-harmonic spectra are tunable by controlling the iris size (Chapter 6). To yield the best data statistics, we adjust high-harmonic spectra such that one harmonic peaks at the asymmetry maxima.

5.2.2 The Pump Arm

The remaining laser power (10%) is used for pumping the sample to induce demagnetization dynamics. We first offset the optical path length of the pump and probe pulses by a motorized linear stage (Aerotech ANT130-160-L). The stage moves with

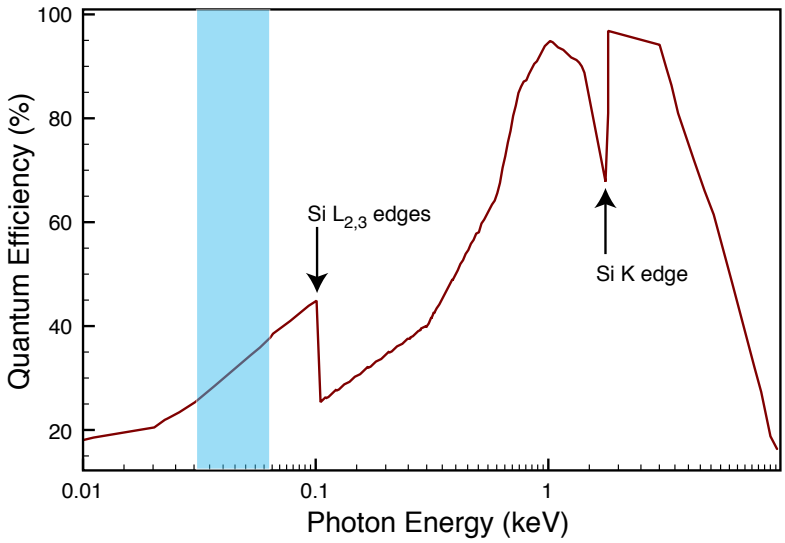

Figure 5.4: Charge-coupled device (CCD) cameras as sensitive detectors for extreme ultraviolet or soft x-rays. The plot shows quantum efficiency of the sensor defined as the efficiency of photons to be converted to the the electronic signal. The blue bar highlights the wavelength range high harmonics employed in this thesis. Reproduced from [19]).

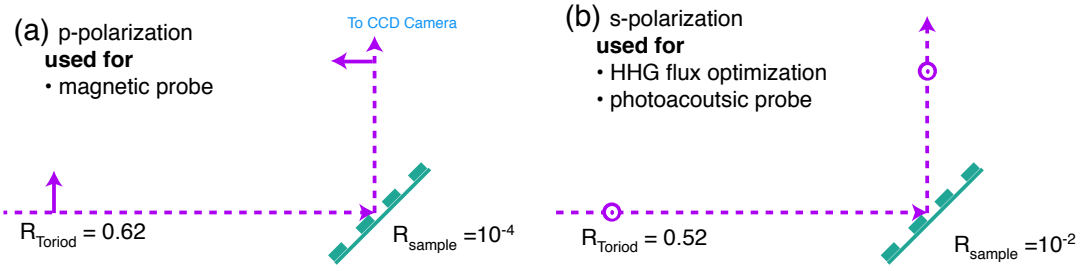

Figure 5.5: Two states of polarization: (a) p-polarization has low sample reflectivity but can probe magnetization. (b) s-polarization has higher reflectivity; therefore, we use this polarization for flux calibration or probing small variation in sample reflectivity such as photoacoustic wave. The drawing geometry is based on the experimental set up (Figure 5.2). We set up the sample reflection upward such that, for p-polarized light, the toridal mirror has 20% higher in reflectivity

1-nm resolution with 250-nm accuracy. The pump beam enters the experimental chamber using a lens (1m focus) glued on the vacuum chamber. The lens and the toroidal mirror together act to reduce the pump beam size on the sample. We recombine the paths of the pump and probe pulses into near collinear propagation with a mirror that has a hole drilled through its center. The pump reflects from the front surface of the mirror, while the probe passes through the hole. The size of the pump beam on the sample is 2.5 mm in diameter. The difference in angle between pump and probe arms at the sample is less than 1°. The spatial and temporal overlap between pump and probe pulses is determined indirectly via the cross correlation; the second-harmonic light is generated when pump and probe pulses overlap at the BBO crystal co-located at the sample position. The accuracy of this method is within ±10 fs. We attenuate the amount of pumping intensity by a continuous neutral density filter wheel. The back reflection beam from the filter is useful for tracking the position of the pump beam to ensure the spatial overlap between pump and probe.

5.3 Samples as Spectrometers

After the high-harmonic beam reflects from a magnetic sample, the spectra of high harmonics must be analyzed with a spectrometer because the magnetic response is strongly dispersive. However, to incorporate an additional spectrometer requires the inclusion of a few more optics such as gratings and toroidal mirrors [155]. However, at the present capability of our light source, the high-harmonic flux after reflecting from the sample is rather limited because of the strong absorption (10^{-4}, Chapter 3) near the Brewster angle, and the inclusion of any more lossy optical components is highly unfavorable. We solve this problem by turing the sample into a spectrometers [156]. We use magnetic grating samples to diffract high harmonics and disperse the harmonic energies (Figure 5.6). These samples are made by Justin Shaw and Tom Silva from NIST by use of photolithography techniques. We optimize the present experimental

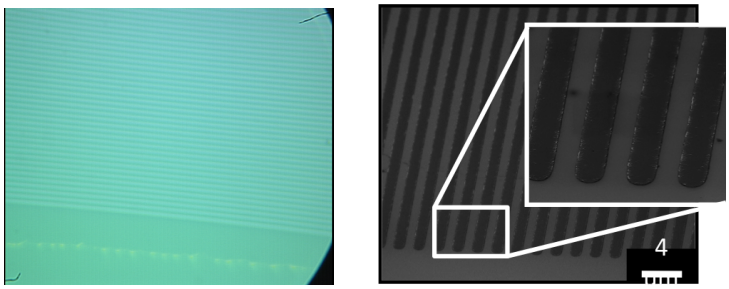

Figure 5.6: Optical and scanning electron micrographs of Permalloy-grating samples showing 1 μm line and space (2 μ m period). Scanning-electron-microscope image is taken by Justin Shaw from NIST.

setup for a grating with $2\mu m$ period.

5.4 Magnets

Other important pieces of our experiment apparatus are the magnets, which produce external magnetic fields to saturate the magnetization. I make use of two magnet geometries in this thesis work. Both types of magnets are driven by a bipolar power supply (Kepco BOP 20-10ML4886).

5.4.1 Helmholtz coil

A Helmholtz pair is composed of two sets of coils with the same direction of winding. The coil radius must be equal to the separation between the coil forms (Figure 5.7a) . At this special condition, magnetic field at the center of the coil is equal to

$$B = (\frac{4}{5})^{\frac{3}{2}} \frac{\mu_0 N I}{R}, \tag{5.1}$$

where μ_0 is permeability of free space ($1.2566 \times 10^{-6} Tm/A$), R is coil radius, I is electrical current and N is the number of wire turns. For our case, N is 33 turns, and radius R is 3 cm while the current I can be varied from -10 to 10 A. The measured magnetic field follows perfectly the prediction from Equation 5.1 (Figure 5.8).

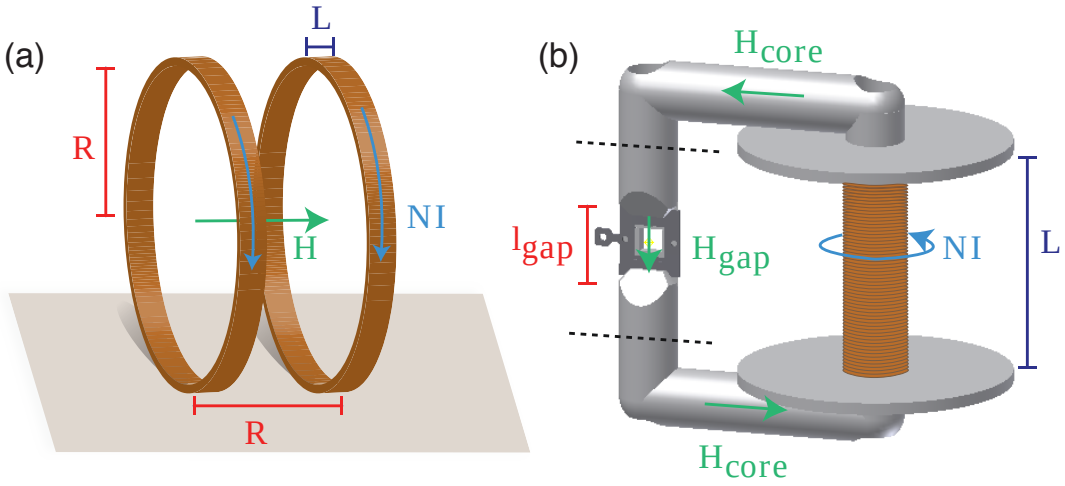

Figure 5.7: Two Magnet Geometries used in this thesis: (a) Helmholtz coil (b) soft-iron-yoke magnet. The dimension parameters described in the text are defined in both figures. The yoke-magnet model is drawn by Carson Teale and Patrik Grychtol.

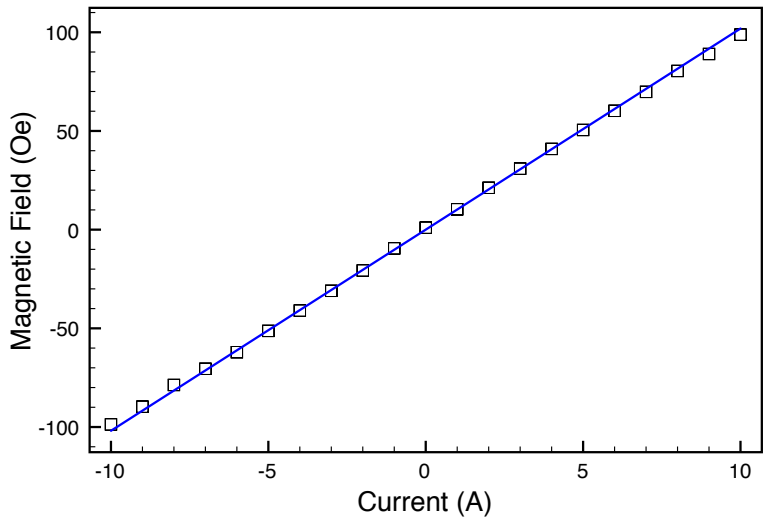

Figure 5.8: Magnetic field generated by our Helmholtz coil with 33 wire turns and 3-cm radius. The blue line is the prediction from Equation 5.1.

The Helmholtz coil geometry has two advantages. Firstly, the coil produces a highly uniform magnetic field. The magnetic field generated is uniform almost everywhere between the coils. Secondly, since the Helmholtz coil utilizes an air core, the total magnetic inductance comes only from the copper wire, which is typically low at our operation frequency at 0.5-1 Hz (1.4 mH [2]). One of the disadvantages of the Helmholtz coil is the small amount of generated magnetic field (H =100 Oe for our case); hence, we are limited to soft magnetic-material samples such as Permalloy. Moreover, the experimental setup is complicated by the requirement for cooling water that must be fed into the vacuum chamber to reduce the heat from the coils.

5.4.2 Soft-iron Yoke Magnet

When magnetic samples require larger amount of magnetic field to switch, we use a soft-iron yoke magnet. The magnet is composed of a loop of magnetized soft-iron as a core. The magnetic field is only confined inside the iron core, unless there is a small gap to make the field accessible to the outside. Typically, modeling of yoke magnets is very complicated. But if the magnet is simplified to be a perfect magnetic circuit with no flux leakage besides the gap, the output magnetic field inside the gap (H_{gap}) is

$$H_{gap} = \frac{NI}{l_{gap} + l_{core}\frac{A_{gap}}{A_{core}}\frac{1}{\mu_{core}}}, \tag{5.2}$$

where N is the number of wire turns, I is the current, l_{gap} is the width of the gap, l_{core} is the total length of the yoke, A_{gap} is the surface area of the gap, A_{core} is the surface area of the yoke, and μ_{core} is the permeability of the core (Figure 5.7b).

The equation suggests that the magnetic field increases with the number of turns of wire or the amount of current. From the textbook value [20], μ_{core} for iron at saturation is about 5000. The number implies that neither the reduction of magnetic-circuit

[2] I estimate the inductance in μH from the formula $\frac{2R^2N^2}{9R+10L}$ [157], where R is the coil radius in inch, N is the number of turns and L is the length of the coil in inches along the direction of the coil axis.

pathlength l_{core} nor the focusing of magnetic poles toward the gap $\frac{A_{gap}}{A_{core}}$ are critically important. In our coil (N = 300 l_{gap} = 1cm, $A_{gap} \approx A_{core}$, μ_{core} =5000, I = 10A), the maximum magnetic should be 3800 Oe, but our field measured is only 500 Oe. The performance of our yoke magnet does not follow very well with the theoretical prediction as in the case of Helmholtz coil. This discrepancy indicates that the assumptions to derive Equation 5.2 are not adequately met. Although the field is smaller than the prediction, this magnetic field is large enough to switch varieties of samples such as Fe and Ni films.

To adapt this magnet into our experiment, we designed this iron-yoke magnet to have samples located between the gap (Figure 5.9). We inserted part of the yoke into the vacuum chamber through Ultratorr feedthroughs but keep the coil outside the chamber. The design simplifies the experiment by not incorporating the water cooling line into the vacuum system.

5.5 Vacuum System

We use three vacuums pumps in our experimental apparatus. At the high-harmonic capillary, a dry scroll pump (Varian TS300) evacuates the gas for high-harmonic generation. Second, another dry scroll pump (Varian TS300) connects to a differential-pumping-section piece with a 45° surface and a hole in the middle to improve the pumping efficiency. Finally, a turbo molecular pump (Pfieffer HiPace 80), backing up by a smaller dry scroll pump (Varian SH110), pumps down the rest of the system. The base pressure of the system is 10^{-6} torr and, because of the compact size of the experiment, the system can be pumped down quickly to 10^{-5} torr within 5 minutes. To vent the system, we make use of an automatic venting value (Pfeiffer TVF 005) to increase the venting speed and protect the turbo pump. The complete venting is done in 10 minutes. We use two types of experimental chambers depending on the types of magnets. The Helmholtz coil fits into a spherical CF chamber (Kimball Physics 6 inch

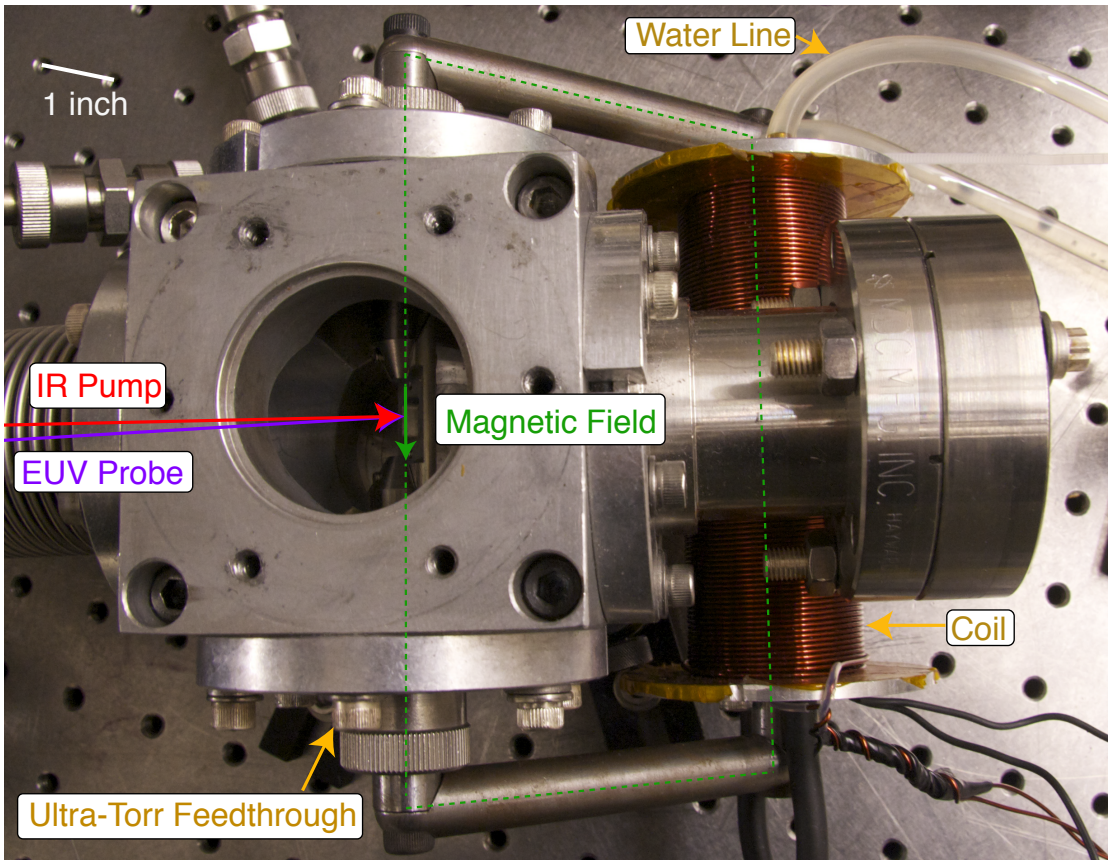

Figure 5.9: Photo of a sample holder and an electromagnet incorporated into a compact experimental chamber (top view). The magnetic samples are located between the gap of the electromagnet where pump and probe beam overlap (red and purple arrows). The electromagnet is composed of soft-iron yoke (green dashed line) magnetized by a coil. Magnetic filed is applied transversely to the sample plane of incidence in T-MOKE geometry (green arrow). Part of the yoke is inserted through Ultra-torr vacuum feedthroughs. The beam height is four inch from the optics table, and the holes on the optical table are one inch apart.

Spherical Octagon Chamber MCF600-SphOct-F2A8), and the soft-iron-yoke magnet is inserted into a custom-made KF40 cube.

5.6 Data Acquisition

Because of intensity fluctuations from high-harmonic source (Figure 6.14), synchronization between magnets and the CCD camera must be incprporated into the experiment. This requirement follows from our experimental technique to measure two high-harmonic spectra with two opposite directions of magnetization to calculate T-MOKE asymmetry. Recall that the reflected intensity of p-polarized light with the presence of magnetization is proportional to

$$|E_{R0}|^2 = |E_{I0}|^2(|R_0|^2 + 2\Re[R_0^* R_M \epsilon'] + |R_M \epsilon'|^2), \tag{5.3}$$

where $|E_{I0}|^2$ is related to the incident intensity, $|R_0|^2$ is the optical contribution, and $|R_M\epsilon'|^2$ is the magnetic contribution. By reversing the sign of magnetization, the magnetic constant has the opposite sign ($\epsilon' \rightarrow -\epsilon'$). From this condition, we can calculate the asymmetry according to the Equation 3.44. We always assume that the incident intensity of light must be equal such that the factor $|E_{I0}|^2$, which appear in both numerator and denominator of asymmetry equation, cancels out. The two reflected spectra must be measured sequentially and faster than the time scale of the intensity fluctuations. We accomplish this condition by switching magnetization as quickly as possible at every camera exposure.

The current direction of the electromagnet is controlled using a simple circuit driven by the "fire" output of the andor CCD[3] (Figure 5.10a). The signal is high (+3 V) when the camera is taking exposures and 0 V during the readout. Then, we use a simple electronic circuit (Appendix 3) or a commercial delay generator (Stanford Research DG535) to divide the frequency of the fire signal by a factor of two (Figure

[3] This output can be located at the back of the camera enclosure for newly design cameras, or from an output box (Andor IO160 for old style cameras with PCI cards.

5.10b). Next, we offset this output voltage down by a half amplitude with a DC power supply. This electrical signal is then used to drive the magnet power supply by inserting the signal into the programing input. With a minor gain adjustment using a simple circuit (Appendix 3) (Figure 5.10c), the final wave form is in the correct phase, and the sign of the current wave switches at every CCD camera exposure (Figure 5.10d).

We apply the same idea of synchronization to hysteresis measurements. In this case, we do not apply a magnetic field to saturate magnetization in both directions ($H > H_s$ and $H < -H_s$). However, we only sweep the field between the saturation ($H > H_s$) and an intermediate state ($-H_s < H < H_s$). The new asymmetry parameter (A_{hys}) can be defined as

$$A_{hys}(H) = \frac{|\mathbf{E}_{R0}(H > H_s)|^2 - |\mathbf{E}_{R0}(H)|^2}{|\mathbf{E}_{R0}(H > H_s)|^2 + |\mathbf{E}_{R0}(H)|^2} \tag{5.4}$$

$$= \frac{(2\Re[R_0^* R_M \epsilon'(H > H_s)] - 2\Re[R_0^* R_M \epsilon'(H)])}{2|R_0|^2 + 2\Re[R_0^* R_M \epsilon'(H > H_s)] + 2\Re[R_0^* R_M \epsilon'(H)]} \tag{5.5}$$

$$\approx \frac{\Re[R_0^* R_M (\epsilon'(H > H_s) - \epsilon'(H))]}{|R_0|^2} \tag{5.6}$$

Again the idea behind this asymmetry definition is to eliminate the optical reflectivity $|R_0|^2$ and the incidence intensity $|E_{I0}|^2$. This hysteresis asymmetry (Equation 5.6) is good for hysteresis loop measurements because the parameter is proportional to the magnetization through $\epsilon'(H)$ with only a constant offset of $\epsilon'(H > H_s)$. The approximation in the third line assumes that the expression can be written in the first order in magnetic constants, $\epsilon'(H)$ and $\epsilon'(H > H_s)$. This approximation breaks down when the angle of incidence is near 45°, or the photon energy is near the absorption edges (Figure 5.11), and in our experiment, we made use of a more grazing incident angle at 72°.

Experimentally, hysteresis loops are measured by synchronizing the CCD camera with magnetic fields oscillating between the saturated field H_s and the measured field H. The field H can be swept across the whole range by adjusting the offset voltage (Figure 5.10c).

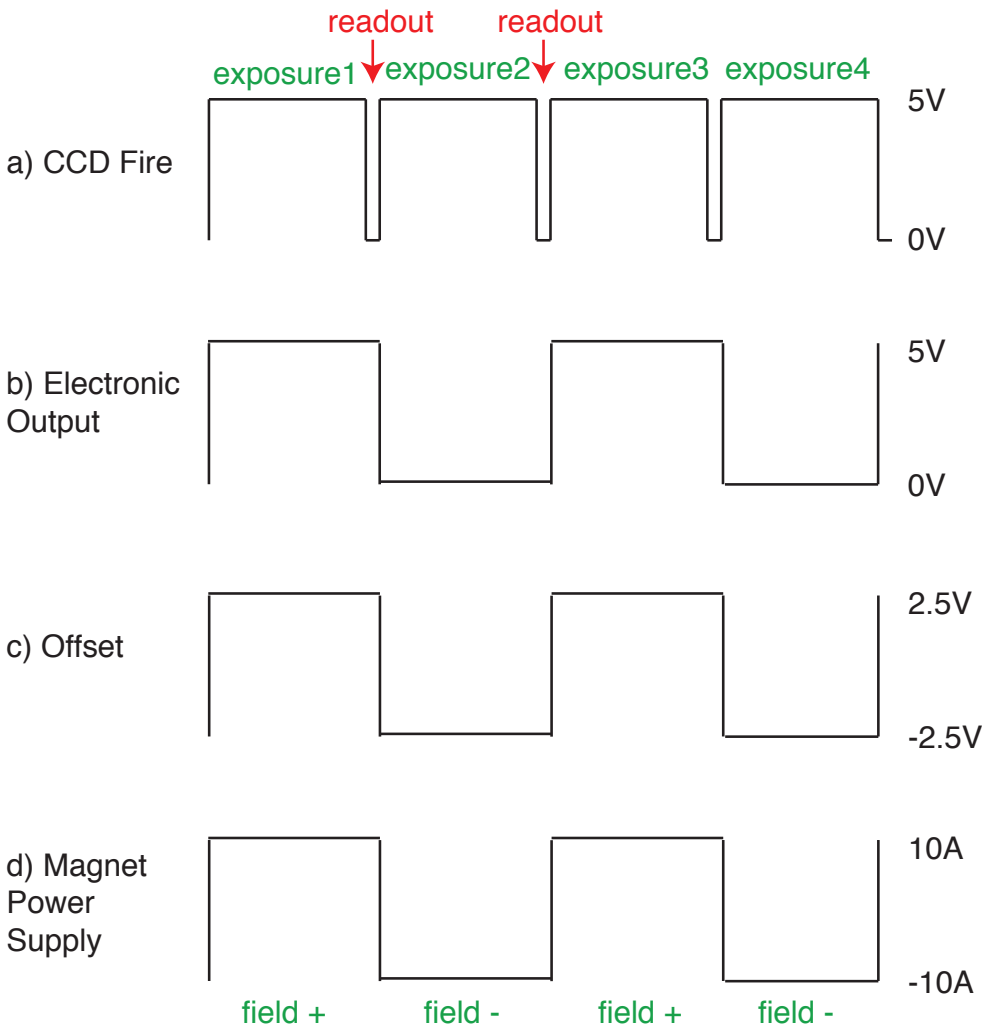

$$I_+ = exposure1 + exposure3 + exposure5 + ...$$
$$I_- = exposure2 + exposure4 + exposure6 + ...$$
$$A = \frac{I_+ - I_-}{I_+ + I_-}$$

Figure 5.10: The synchronization between the CCD camera and the magnetic power supply. Start from (a), the fire output from CCD camera in the kinetic-series mode gives a high signal during the exposure and a low signal during the readout. Then, (b), an electronic circuit modifies the signal waveform. (c) A DC-power supply offsets the voltage down. Finally, (d), the waveform becomes an input into a current-power supply. After a series of exposures, the exposures with the same sign of magnetic field are averaged together for the calculation of asymmetry.

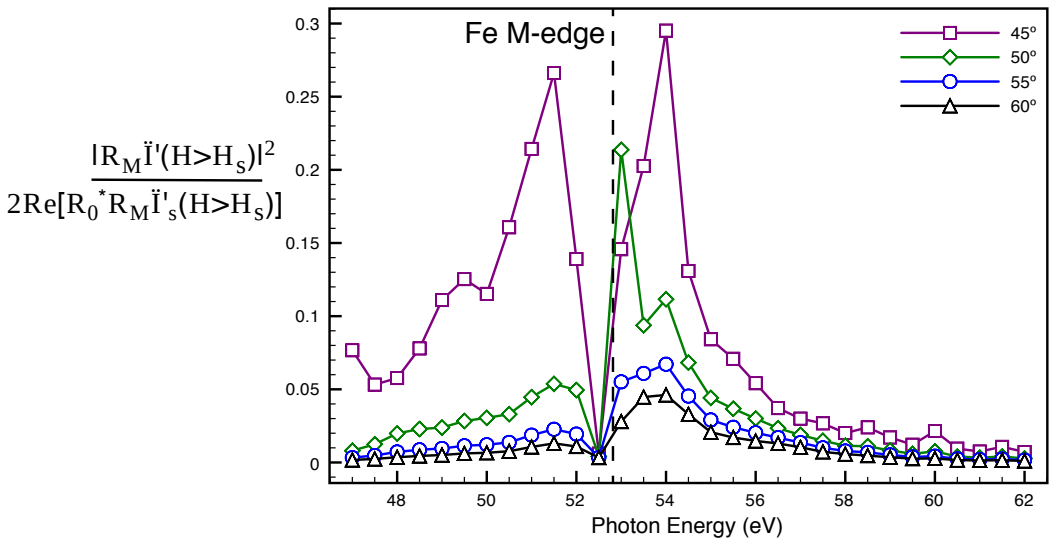

Figure 5.11: The validation of the linear approximation applied to the numerator of Equation 5.6. The plot shows where the second order term, $|R_M \epsilon'_s|^2$ is significant when compared to the first order term, $2\Re[R_0^* R_M \epsilon'_s]$. This hysteresis asymmetry is not proportional to magnetization when the angle of incidence is close to 45°, or the photon energy is near M edges.

Chapter 6

Probing Magnetization by Use of Extreme Ultraviolet High-harmonics

6.1 Introduction

This chapter covers the experimental results showing that extreme ultraviolet high harmonics are capable of probing static magnetization. Acquiring these static results is an important step toward the time-resolved studies presented in the next chapter. In the next section, I present the measured high-harmonic spectra and the method to calibrate photon energy from the CCD images. Then, by switching the magnetization, I discuss the observed magnetic asymmetry in reflected spectra via the transverse magneto-opitcal Kerr effect (T-MOKE), which is directly related to magnetization. At the end of this chapter, I present important information about the tunability and stability of our high-harmonic generation light source.

6.2 High-harmonic Spectra

In our experimental geometry (Section 5.3), we diffract high harmonics from magnetic grating samples to spectrally resolve the photon energy of the harmonics. We use a CCD camera to capture images of high-harmonic diffraction patterns. The photon energies of harmonics are scaled by the physical length along the CCD chip, and we have to relate the pixel information back to the photon energy. Employing the geometry of our spectrometer and sample parameters, I calibrate the image pixel number to photon energy by the following:

6.2.1 Diffraction Formula

I start with the diffraction formula for gratings:

$$d(\sin(\beta) \pm \sin(\alpha)) = \pm m\lambda \tag{6.1}$$

where d is grating period, m is diffraction order, λ is wavelength, and the α is incident angle, and θ is diffracted angle (Figure 6.1). I convert the diffracted angles (θ) to the number of image pixels (n), CCD pixel size (D) and the sample-to-CCD distance (z) (inset of Figure 6.1). The wavelength (λ) can be written in the form high-harmonic photon energies, which are odd multiples of the fundamental photon energy (E_o) , $E = \frac{hc}{\lambda} = NE_o$, where h is the Plank's constant, c is the speed of light, and N is an odd integer. Then, the diffraction formula (Equation 6.1) is transformed to

$$n = (\arcsin(\frac{mhc}{E_o N d} - \sin(\alpha)) + \alpha)\frac{z}{D}, \tag{6.2}$$

which describes the pixel location n for the the Nth-order harmonic in the case of m-th order diffraction.

6.2.2 Fit to Data to the Diffraction Formula

The above equation has two unknown variables: the fundamental photon energy (E_o) and the orders of harmonics (N). To find these two parameters, I perform a curve fitting to the experimental data with the diffraction formula (Equation 6.2) with N as the independent parameter (x) and n as the dependent parameter (y). The free parameter for the fit is the fundamental energy (E_0). Initially, I guess the highest orders of harmonics N from the L-edges of Al filters (72 eV or $N_{max} \approx 45$) used to block the laser light after the high-harmonic waveguide, which limits the highest photon energy. Since the orders of harmonics are only based on guessing, the correct orders might be slightly different. Only the right order of harmonics gives a good fitting result (Figure 6.2).

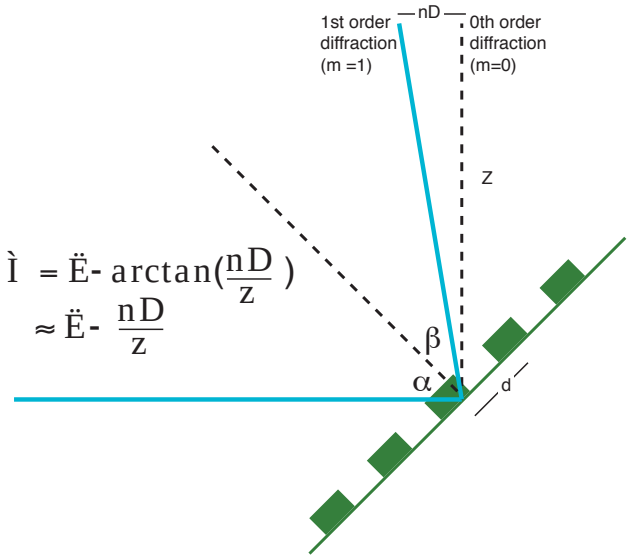

Figure 6.1: The diffraction geometry from a grating (Equation 6.1), where d is the grating period, α is the incident angle, D is the pixel size, n is the number of image pixels , and z is the sample-to-CCD distance.

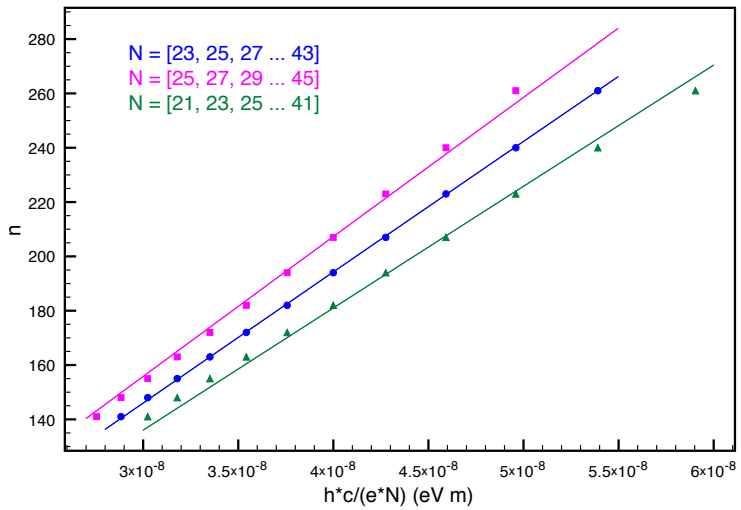

Figure 6.2: How to determine the correct high-harmonic orders. The diffracted distance (n, in pixel) measured from the CCD image is plotted as function of the inverse high-harmonic order (N scaled with $\frac{e}{hc}$) from three series of high-harmonic orders. The series $N = 23, 25, 27, ...43$ (blue) is the only correct high-harmonic order because it gives a good fitting result.

For our experimental geometry, we can simplify the fit equation greatly by setting the angle of incidence (α) to 45°. In this special case, the factor $\frac{hc}{E_o N d}$ in the Equation 6.2 becomes a small number ($\sim$ 0.01 for 60 eV) comparing to $\sin\alpha = \sin 45^\circ \approx 0.7$; therefore, the fitting function (Equation 6.2) is approximately

$$n \approx \sqrt{2}\frac{mhcz}{E_o N d D}. \tag{6.3}$$

The result shows that n is linearly dependent on $\frac{1}{N}$ (Figure 6.2). In addition, Equation 6.3 implies that the fit can only yield the ratio $\frac{z}{E_o}$, and either the fundamental photon energy (E_o) or the sample-to-CCD distance (z) must be predetermined from a measurment, and usually, the distance z is more convenient to measure.

6.2.3 Results

I calibrate a high-harmonic spectum diffracted from a Permalloy grating with the period of 2 μm (Figure 6.2). The sample-to-CCD distance (z) is 29 cm, and the angle of incident is set to 45°. The fit gives $E_o = 1.61 \pm 0.002$ eV. This result corresponds to 770 ± 1 nm wavelength. The fundamental photon energy is slightly blue-shifted in the same way as reported in Reference [155]. The blueshift originates from a non-linear optical process in the capillary discussed in Section 6.4.

From this information, I map diffraction-pattern pixels to photon energy (Figure 6.3). The result is verified by determining the photon energies of the higher-order diffraction patterns ($m > 1$). For example, the second order diffraction photon energy must be one-half of the first-order diffraction[1] .

I repeat the same fitting method for calibrating the high-harmonic spectrum from argon (Figure 6.4). The intensity of high harmonics generated by argon is generally one to two orders-of-magnitude larger than that of neon because of the lower ionization

[1] This comes from the factor $m\lambda$ in Equation 6.1. The second order diffractions overlap with the first order diffractions where $\lambda_{m=1} = 2\lambda_{m=2}$.

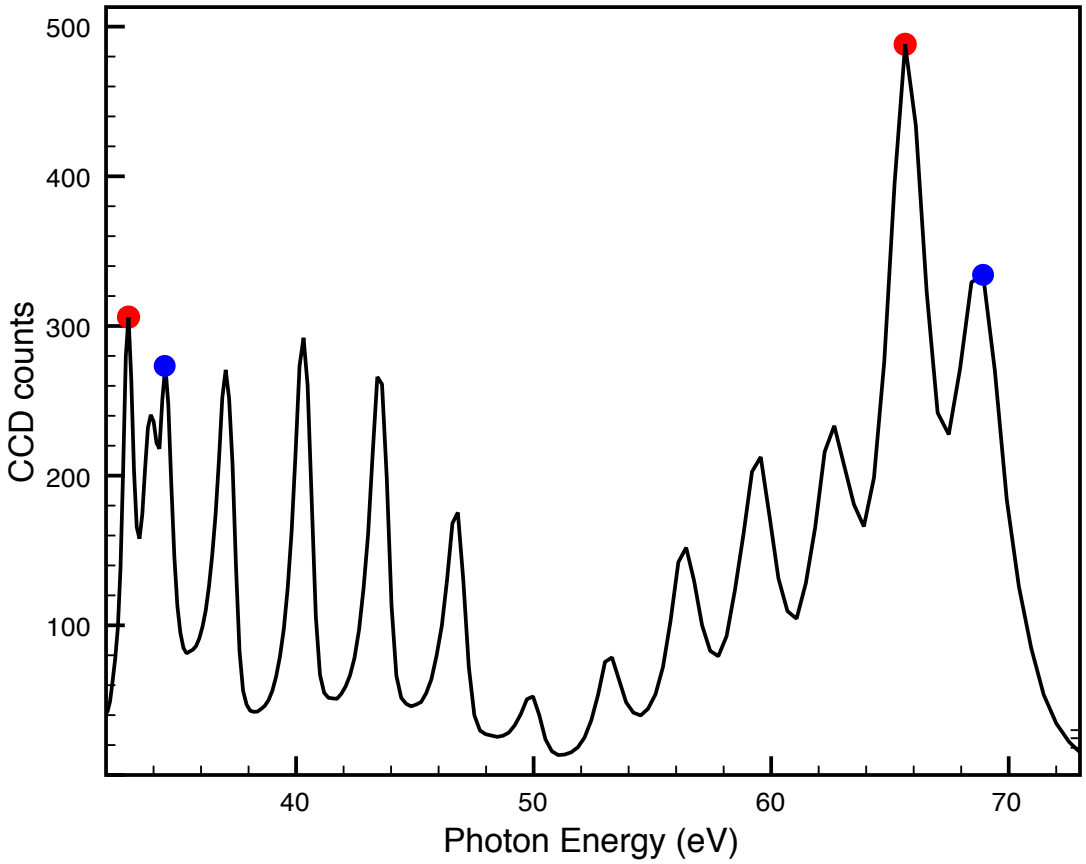

Figure 6.3: High-harmonic spectrum from neon reflected from a Permalloy grating with p-polarized light and the exposure time of 0.5 s. The second-order diffraction pattern is visible in in the spectrum, and the locations of them are exactly one half of the photon energies of the corresponding first-order harmonics as shown by the blue and red dots.

potential and higher gas trasmittivity. In this case, the counts from the CCD camera are ten times greater, although the exposure time of the camera is five times shorter.

6.3 Asymmetry Spectra

6.3.1 Static Asymmetry of Permalloy

After the calibration of a high-harmonic spectrum, the asymmetry spectrum introduced in the Chapter 3 can be calculated. The first important step is to subtract the background level of the CCD images because of 'dark current', which originates from thermal excitations inside the CCD pixels. With the background contribution, the asymmetry can be erroneous especially when the background level is comparable to the signal level. Its contribution can be seen from the definition of asymmetry, $A = \frac{I_+ - I_-}{I_+ + I_-}$. With the presence of the background level (B), the detect signal on CCD is

$$(I_{+(-)})_{measured} = I_{+(-)} + B. \tag{6.4}$$

The background level cancels out in the numerator but does not in the denominator,

$$(I_+ + I_-)_{measured} = I_+ + I_- + 2B = (k+1)(I_+ + I_-), \tag{6.5}$$

where k is defined as the ratio of the background level to the signal level ($B = k\frac{I_+ + I_-}{2}$). As a result, the measured asymmetry is smaller by a factor of $k+1$ than the actual value,

$$(\frac{I_+ + I_-}{I_+ - I_-})_{measured} = \frac{1}{(k+1)}(\frac{I_+ - I_-}{I_+ + I_-}). \tag{6.6}$$

The background has to be subtracted out to yield the actual asymmetry ($B = k = 0$). As a drawback, the background subtraction can cause a noisy asymmetry spectrum at the background level because of the division by zero ($I_+ + I_- = 0$). The problem can be addressed in part by averaging the asymmetry spectra over many repeated measurements.

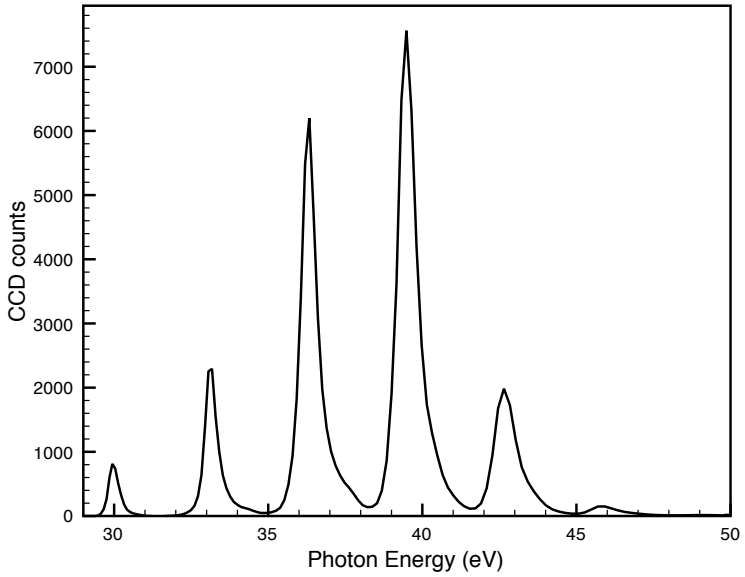

Figure 6.4: A typical high-harmonic spectrum from argon from a Permalloy grating with s-polarized light and the exposure time of 0.1 s.

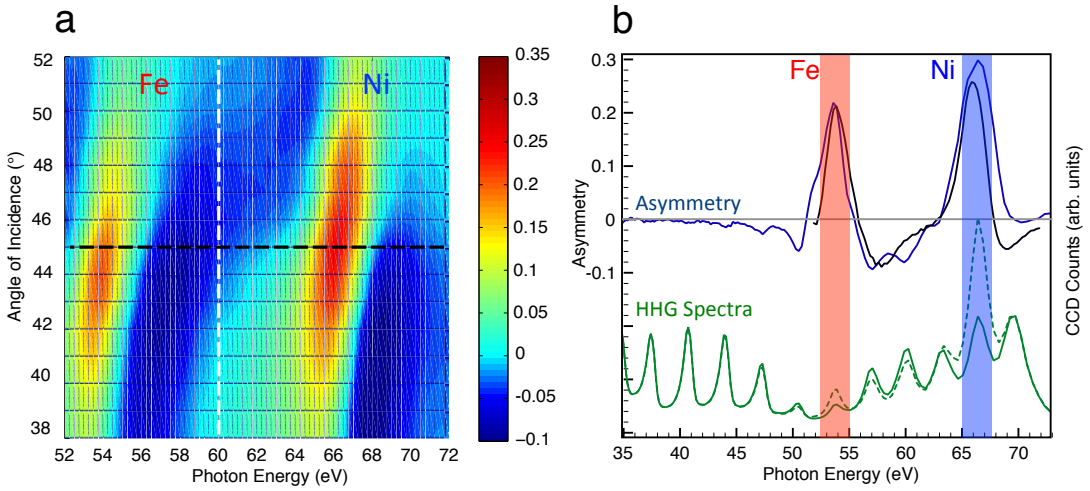

Figure 6.5: (a) Asymmetry spectra as a function of the angle of incidents. The spectra are measured from BESSY synchrotron (data courtesy from P. Grychtol, R. Adam and C. M. Schneider, Forschungszentrum Jülich, Germany) (b) The synchrotron asymmetry data at 45° (black line) is compared with an experimental asymmetry by use of the high-harmonic source (blue line). Both results are in agreement (top). The figure also displays high-harmonic spectra reflected from a Permalloy grating before (green line) and after (dashed green line) revering the magnetization (bottom).

After averaging multiple asymmetry spectra, a clean asymmetry can be calculated (Figure 6.5). The larger amount of asymmetry (30%) is measured near Fe and Ni M-edges of both elements (53 eV for Fe and 67 eV for Ni). Fe and Ni contribute to the asymmetry spectrum by exhibiting two sets of positive and negative contrasts, which is the consequence of the bipolar nature of the magneto-optical constant at resonance transitions. The asymmetry measured by high-harmonic generation source is in agreement with a T-MOKE measurement of the same Permalloy grating obtained at the BESSY synchrotron (Figure 6.5). A slight mismatch comes from the qualitatively distinctive spectra between high-harmonic generation and synchrotron radiation, which is composed of discrete harmonics for high-harmonic generation and is a quasicontinuum for synchrotron radiation.

The measured asymmetry of Permalloy is in contrast to that of Ni. With one constituent element, the asymmetry only shows one positive and negative contrast near Ni M-edges (Figure 6.6) .

From all previous results, the experimental geometry is set to 45°. If the asymmetries are measured at more grazing-incident angles (higher incident angles α) (Figure 6.7), the asymmetry parameter drops down quickly from 30% to less than 10% with more grazing angles. This reduction in asymmetry is also found in the synchrotron result and earlier in the T-MOKE calculation (Figure 6.5 and 3.6). Moreover, by tuning the polarization of harmonics from p- to s-polarization, the asymmetry disappears as expected from the derived refractive index of s-polarized light (Equation 3.18).

6.3.2 Element-Selective Hysteresis

By generalizing the static asymmetry measurement, magnetic hysteresis is measured by extracting asymmetries as a function of the external magnetic field, H. I have already explained the experimental method to measure the hysteresis loop (Section 5.6), which suggests that the angle of incident should be more grazing (62°) to make sure

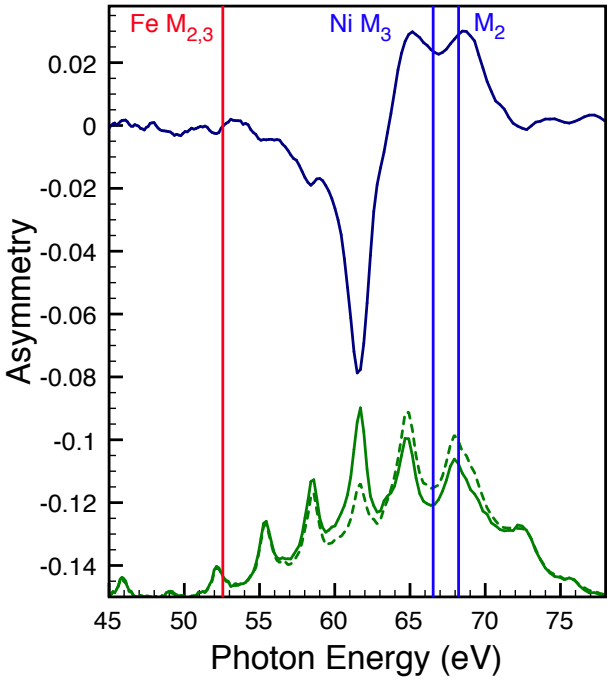

Figure 6.6: The asymmetry spectrum at 45° of Ni (Top) calculated from high-harmonic spectra reflected from a Ni grating with two signs of the magnetization (bottom). In contrast to Permalloy, only Ni contributes to the asymmetry spectrum.

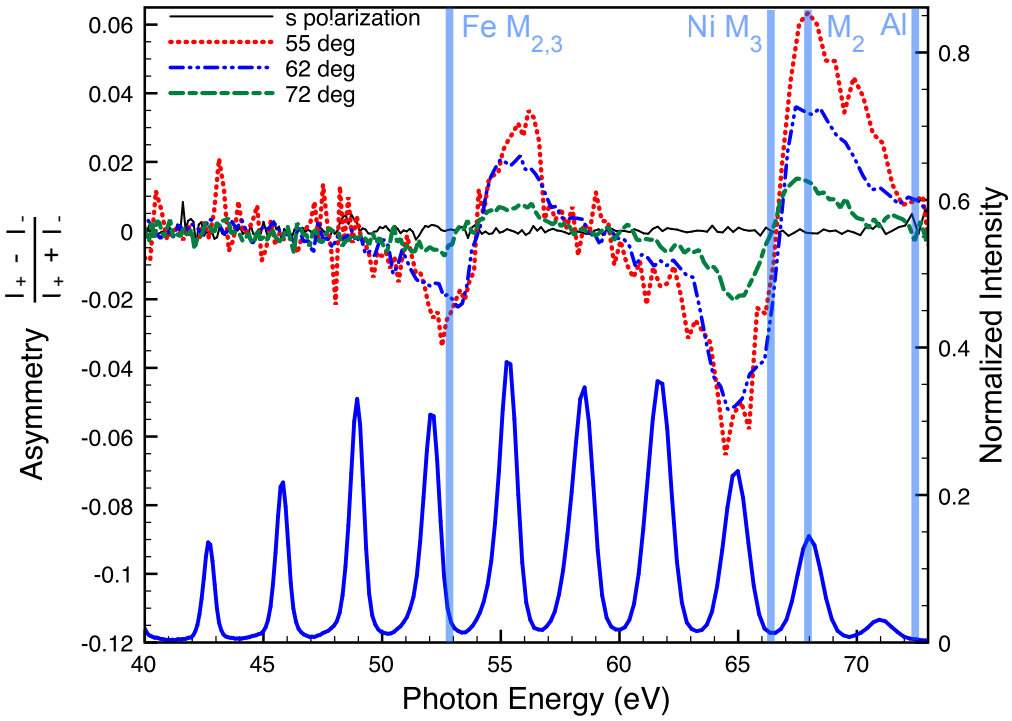

Figure 6.7: Magnetic asymmetries with three angles of incident, 55° (red), 62° (blue), 72° (green), measured from high-harmonic generation light source (a typical spectrum shown in the bottom). The M-shell absorption edges of Fe and Ni are shown as vertical lines. The three measurements employs p-polarized probe light. In contrast, with s-polarized probe light, the asymmetry signal disappears (black).

that the asymmetry and magnetization are linearly dependent. In this case, our group extracts two hysteresis loops near Fe and Ni M-edges (Figure 6.8). The loops have a square shape, as expected for a patterned grating material with field applied along the easy axis [158]. The measurements at both M-edges yield identical hysteresis loops, with a coercivity[2] of 800 A/m (10 Oe). The observation of nearly identical hysteresis loops for Fe and Ni in Permalloy is the consequence of the strong exchange coupling between the local magnetic moments of Fe and Ni.

6.3.3 Attenuation of Asymmetry Signal with a Palladium Capping Layer

Besides the hysteresis measurement, extreme ultraviolet light can be exploited to probe the surface properties of layered magnetic structures because of the short penetration depth of only a few tens of nanometers at energies below absorption edges. To demonstrate this ability, the asymmetries for Permalloy gratings with Palladium (Pd) capping layers of different thickness on top of the Permalloy gratings are measured. Pd is used because it does not oxidize or have any strong absorption edge near either the Ni or Fe edges (Figure 6.9b). This allows the measurement of the asymmetry decay because of the absorption of harmonics by the Pd overlayer. Tabulated data for Pd, with an assumed density of 1.2×10^4 kg/m^3, predict attenuation lengths of 3.6 nm and 3.3 nm, at 55 eV and 67 eV, respectively, for the angle of incidence at 62°. The asymmetries near the Ni and Fe absorption edges decay exponentially as a function of the capping-layer thickness (Figure 6.9). Data fitting yields decay lengths of 3.02±0.4 nm (Ni M-edge) and 2.68±0.9 nm (Fe M-edge) which are very close to the predicted penetration depth. This data shows the sensitivity of asymmetry to the surface properties of magnetic material and exhibits potential for using M-edge as a near-surface-sensitive magnetic probe.

[2] The amount of magnetic field where the magnetization crosses zero.

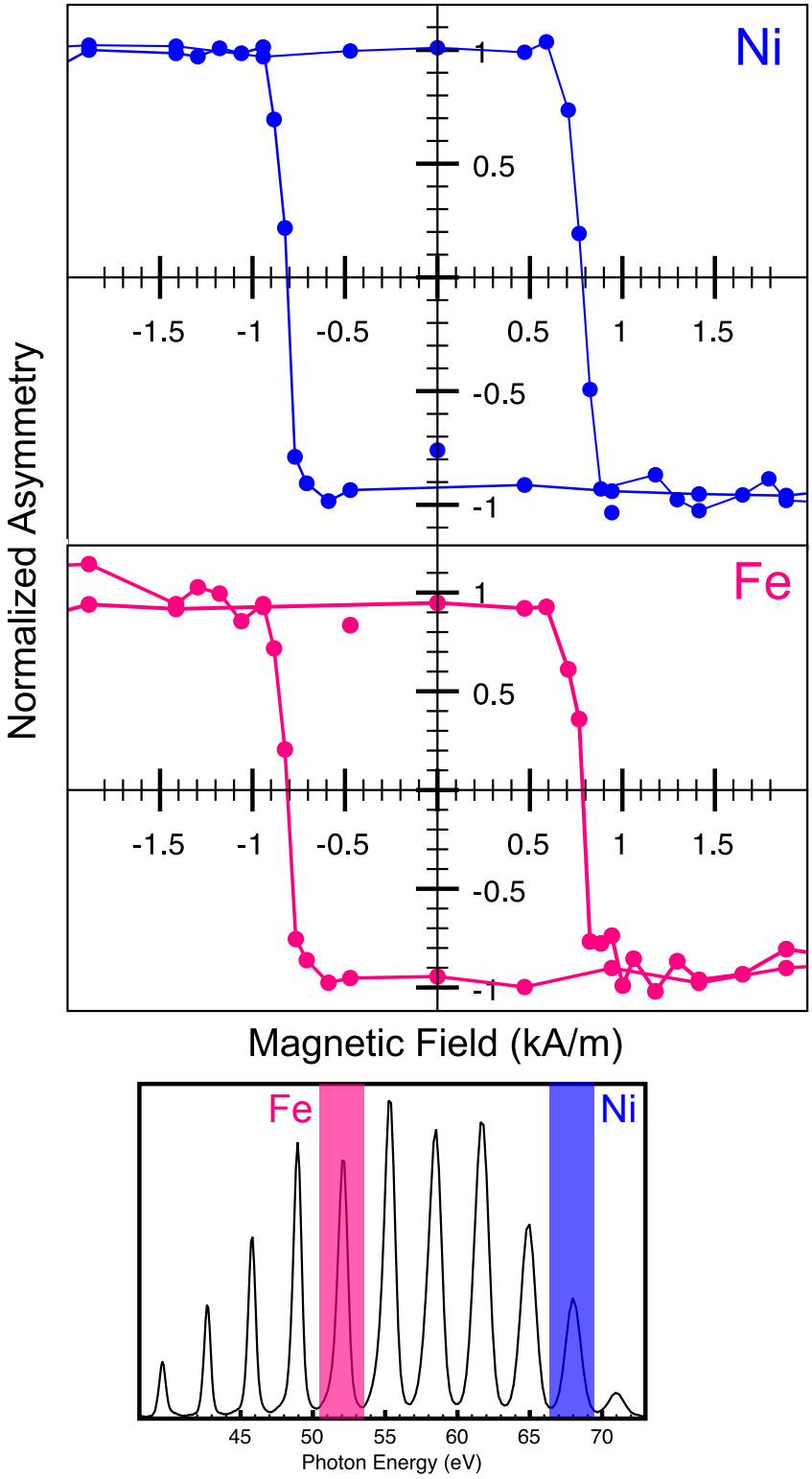

Figure 6.8: Element-selective hysteresis loops of a Permalloy grating measured near the Ni (top) and Fe (bottom) M-edges, with the selected energies indicated on the bottom. Fe and Ni have the same hysteresis loop because of the tight exchange coupling in Permalloy.

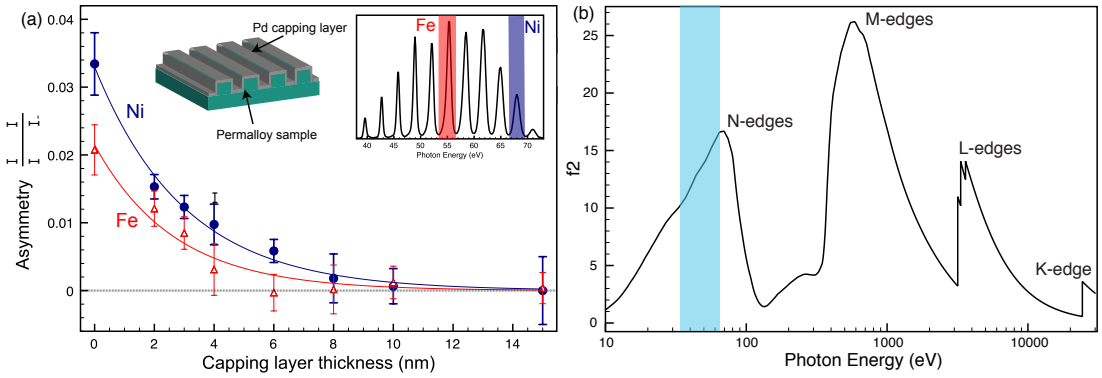

Figure 6.9: (a) The asymmetry of Permalloy as a function of Palladium capping-overlayer thickness. The asymmetries near Fe and Ni M-edges, labeled on the inset, decay exponentially with the decay constants of 3.02±0.4 nm (Ni) and 2.68±0.9 nm (Fe). (b) f_2 parameter of Pd from [13] to illustrate the positions of absorption edges to show that the our high-harmonic spectra (blue shade) are far away from strong absorption edges of Pd.

Grating Material and thickness	Ni	Fe
Si_3N_4		
20 nm	0.29	4.29
10 nm	1.14	2.95
Cr		
10 nm (Figure 6.10)	1.15	0.98
5 nm	0.50	4.02
2 nm	0.21	3.64

Table 6.1: Optimizing the grating structures to improve the signal-to-noise ratio of the data, defined as a ratio of the average of asymmetries to their standard deviation. The asymmetry is acquired near M-edges of Ni and Fe from 30 data sets with 25 s of exposure time for each of them.

6.3.4 Multilayers

Since the asymmetry decays exponentially as a function of the Pd buried thickness, the magnetic signals of the underneath layer may be too weak for the probing of magnetization in case of magnetic-multilayer structures, which are useful for many spintronic applications [159, 136]. Here, I present a result to demonstrate that the asymmetry signal near absorption edges is strong enough to measure even with some degree of attenuation.

A sample employed here is a trilayer of Fe(10 nm)/Cr(2 nm)/Ni(5 nm) from the bottom to the top (Figure 6.10). The grating pattern on the top layer is made from 10 nm of Cr. Light is absorbed by Ni and Cr, but the penetration depths of both elements are longer (∼10 nm) comparing to Pd (∼2 nm). The longer penetration depth can be understood from the general trend that the higher atomic mass (Z), the stronger material absorption.

For this sample condition, the magnetic asymmetry is dominated by Ni (10%) since it is the top layer. But near Fe edge, we observe a slight negative asymmetry (-2%), which may attribute to the Fe layer. However, this Fe asymmetry is not large enough for the demagnetization dynamical studies. We tried to improve the signal-to-noise ratio of the data by improving both the diffraction efficiency of the gratings and

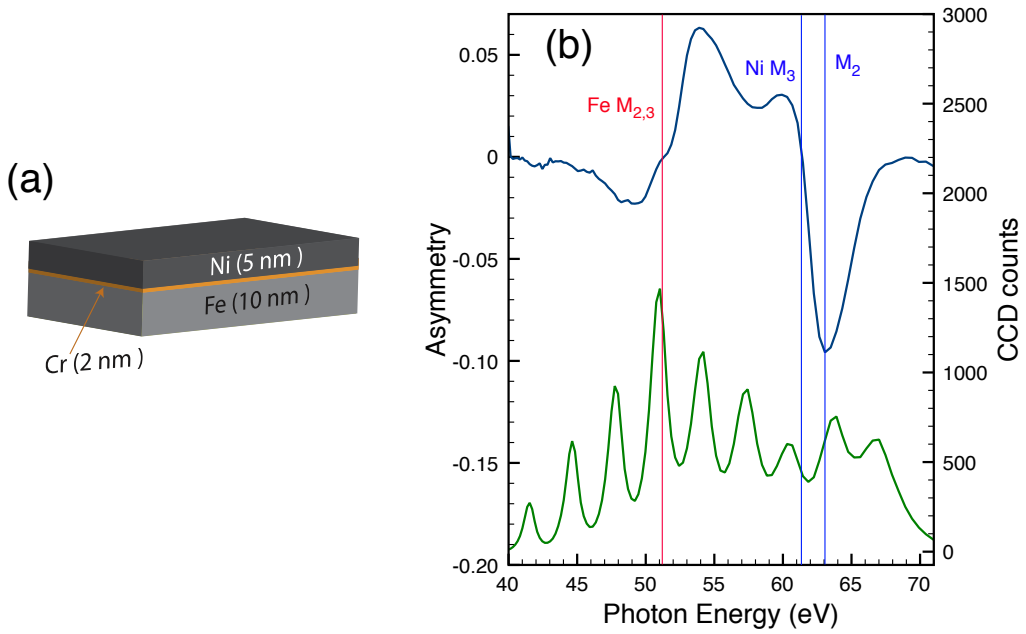

Figure 6.10: (a) The geometry of a magnetic trilayer of Fe, Cr and Ni. (b) The asymmetry measured from this sample dominates by the top layer (Ni), while we only observe a weak signal of Fe.

the amount of the asymmetry contrast. Both factors are controlled by the choice of grating materials and thicknesses. The diffraction efficiency is the highest when the reflected light from the top surface and the groove of the grating destructively interfere to each other by the optical-path difference due to the grating thickness. On the other hand, the asymmetry is exponentially reduced as a function of the grating thickness demonstrated in the previous section. Both requirements are strongly photon-energy dependent; therefore, it is not trivial to find the best grating structure for the Fe and Ni M-edge photon energies simultaneously.

To optimize for the grating condition, we varied the thickness of both Cr and Si_3N_4 capping-layer gratings (Table 6.1). The signal-to-noise ratio (defined as the ratio of the average asymmetry to its standard deviation) at Fe M-edges is enhanced by Si_3N_4 gratings or thinner Cr gratings. This observation can be explained by the weaker absorption of Si_3N_4 comparing to Cr; therefore, Si_3N_4 gratings yield the higher asymmetry. However, as a drawback, the grating efficiency for the Ni M-edge harmonic is reduced as the grating bars become more transparent to light. Therefore, there must be a balance between the two photon energies. From this data, the grating made from 10 nm of Si_3N_4 appears to be the best compromise to improve both Fe and Ni signal-to-noise ratios.

Thus far, in this chapter, I cover magnetic measurements from the asymmetry parameter. However, in the next two sections, I would like to switch our attention to non-magnetic measurements that provide important information about our high-harmonic generation source: the tunability and stability analysis.

6.4 Tunability of High-harmonic Spectra

To achieve the best signal-to-noise for asymmetry measurements, the photon energies of the harmonics that are the nearest to M-edges need to be shifted to the maxima

of the asymmetry spectra. We can shift the photon energies of harmonics by adjusting the prisms in the oscillator or the laser chirp [160]. However, the most convenient way to tune the harmonic spectra is by a slight intensity adjustment of the driving laser. The fundamental mechanism behind the energy shifting is due to a non-linear interaction between laser and plasma known as 'plasma-induced blue-shifting' [161, 155] . The laser photon energy is shifted (ΔE) in the presence of plasma by

$$\delta E = \frac{h^2 N}{2\pi m_e c} \frac{1}{E} \frac{d\eta}{dt} L. \tag{6.7}$$

In this equation, the Planck's constant (h), the speed of light in vacuum (c), the electron mass (m), and the interaction length (L) are constants. The number density of atoms (proportional to the gas pressure), N, can cause the wavelength shift, but the gas pressure has to be optimized to achieve the best phase matching [89, 84]. The only free parameter here is the rate of change in ionization fraction, $\frac{d\eta}{dt}$, which is a sensitive function of the laser-pulse electric field (Chapter 2); therefore, a small change in the laser intensity will result in a slight shift of the fundamental photon energy of high-harmonic generation, which is enlarged at the high orders of harmonics ($N \approx 40$). A shift of $\sim \frac{3}{40}$ eV $= 0.075$ eV is needed to cover the whole comb of high-harmonic separations.

Experimentally, we tune the laser intensity easily by adjusting the size of an iris diaphragm in front of the high-harmonic capillary (Figure 6.11). The harmonics can be tuned over the full spacing of the high-harmonic separation, while the intensity is slightly reduced. However, regardless of the tuning of high-harmonic spectra, the asymmetry peaks associated with M-edge transitions of Ni and Fe are always located at the same photon energies.

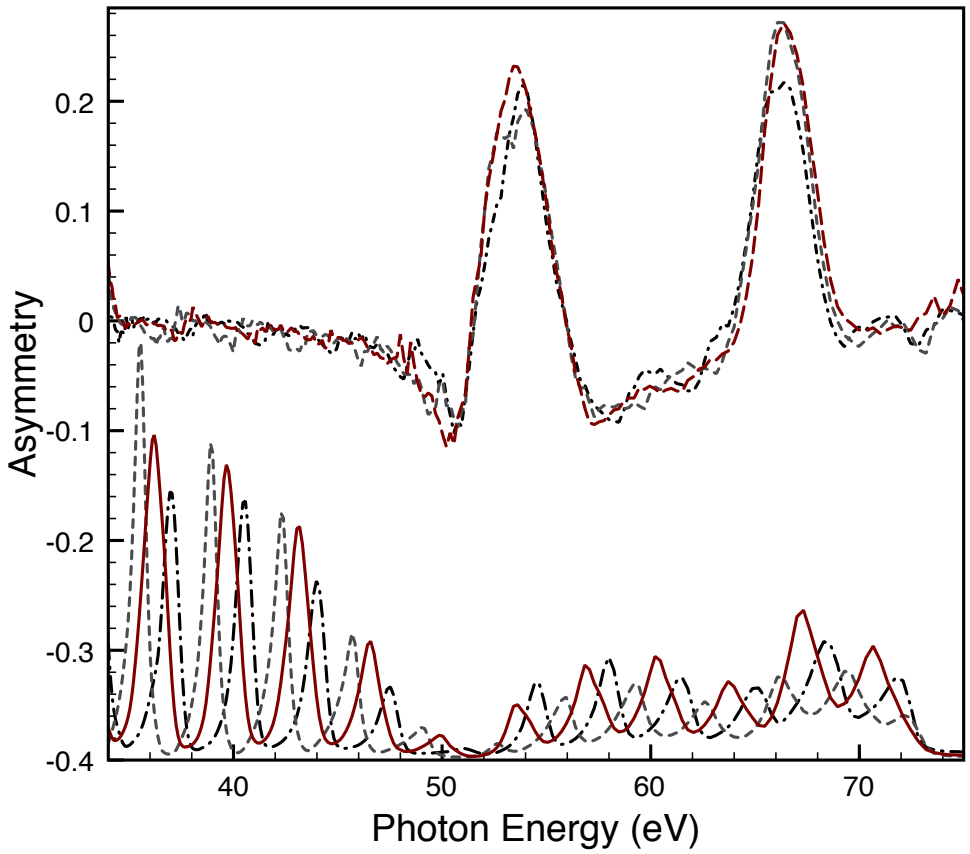

Figure 6.11: The wavelength tunability of high-harmonic generation. High-harmonic and asymmetry spectra are measured with three different sizes of an iris diaphragm. The iris reduces the peak intensity of the laser resulting in the blueshifting inside the capillary. We can tune the harmonic energies across the full range of high-harmonic comb.

6.5 Long-term Stability Test of High-harmonic Spectra

Because of the extreme nonlinearity involved in high-harmonic generation, the intensities and spectra of high harmonics change with a slight change in environmental conditions. Many conditions can be controlled, such as gas pressure and capillary alignment; while some parameters are more challenging to keep stable, such as room temperature, vibrations, and humidity. As a results, the high-harmonic intensities and spectra drift over time in these experiments. In this section, the intensity and photon energy of high harmonics are measured as function of time for 16 hours in order to monitor the stability of our light source at the present stage in its current implementation.

I collected a series of high-harmonic spectra over 16 hours (Figure 6.12). These spectra were collected as part of the time-resolved pump-probe measurement for a Permalloy-Cu grating (Chapter 7). Generally, the structure of the diffraction pattern remains relatively constant throughout the scan, but the spectra have some obvious discontinuities in intensities (e.g., at 1.75 and 13 hours), which result from our intentional efforts to adjust the laser timing, realign the high-harmonic capillary, and refill the liquid-nitrogen dewar for the laser crystal.

From this data, I calculated the photon energy of the high harmonics near the Fe and Ni M-edges (Figure 6.13) from the centroids of the reflected intensities. The high-harmonic photon energies are relatively stable (about 0.2 eV for Ni and 0.13 eV for Fe of RMS noise[3]) when compared to the photon energies of the Ni (68 eV) and Fe (53 eV) M-edges. The stability improves after the first two hours of data acquisition because the room temperature tends to be more stable at night. At these stable hours, the RMS noise reduces by one orders-of-magnitude to 0.01 eV.

By observing that the ratio between the RMS deviation of Ni to that of Fe ($\frac{0.2}{0.13} = 1.5$) is similar to the ratio of the harmonic orders ($\frac{39}{31} = 1.3$), the energy drift presumably

[3] Defined as $(\Delta y)_i = \sqrt{(y_i - \bar{y})^2}$ with $\bar{y} = \frac{\sum_{i=1}^{N}}{N}$.

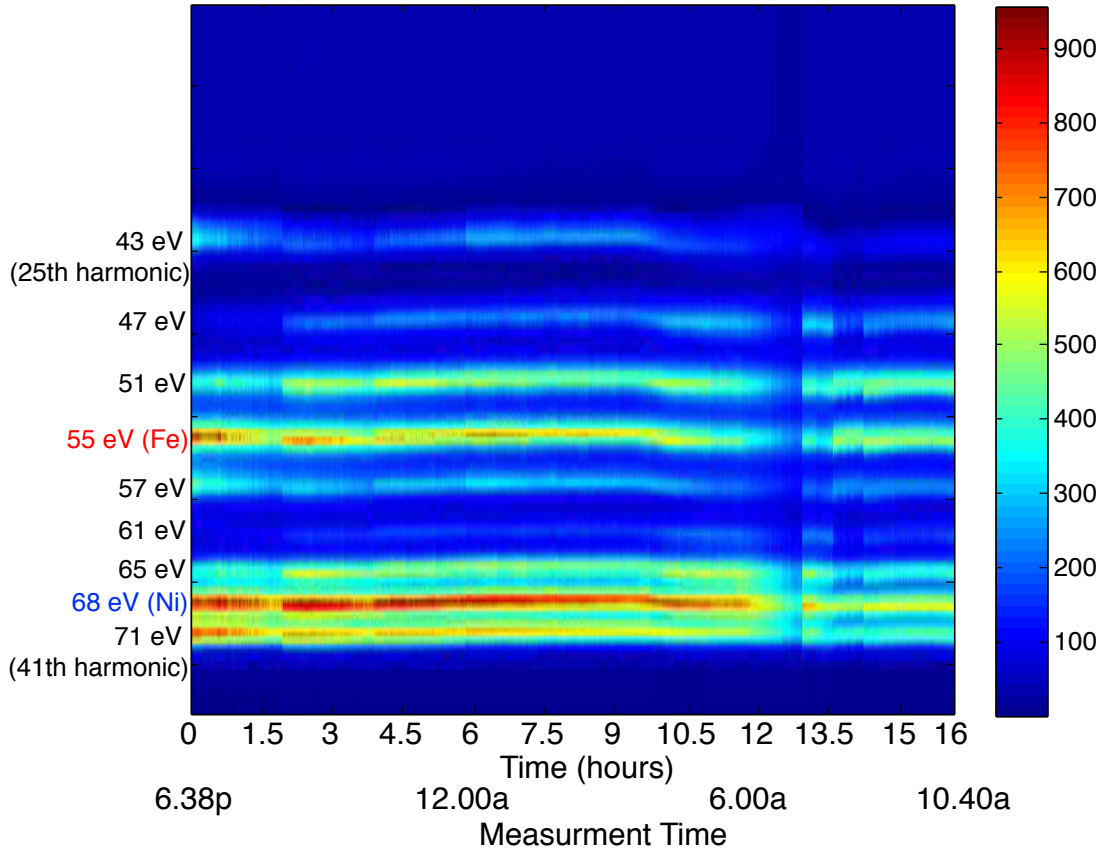

Figure 6.12: The long-term stability test of high-harmonic spectra reflected from PyCu grating over 16 hours.

originates from the shift of the fundamental energy of the pump laser for the high-harmonic generation. This shift can come directly from the drift of the laser center wavelength or indirectly from the variation in laser intensity via the blueshifting inside the capillary (Section 6.4).

Finally, I consider the intensities of the harmonics near the Fe and Ni M-edges as a function of time. The intensities of the harmonics (Figure 6.14) show a greater variation than the that of photon energy. The intensity reduces to about 70% of the initial value by the end to the scan. The reduction in the intensity at the 16th hour is irreversible. The intensity degradation might due to (1) permanent damage of the grating structure by continuous pumping for 16 hours[4] or (2) the slow condensation of a water film over the CCD surface after cooling down for a long time.

The stability of the high-harmonic signal is improved by making sure that the pump laser is perfectly mode-coupled to the inner diameter of the high-harmonic capillary, as demonstrated in Reference [162]. We solve this problem by use of a motorized mirror mount to keep the laser pointed at the same position. We use a CMOS camera (Mightex) to monitor the beam position from a small portion of the laser beam picked off by a pellicle beamsplitter. We implemented this pointing-stability setup in the experiment described in Reference [163], allowing us to take more data with a longer acquisition time and a constant pump-probe beam overlap.

6.6 Conclusions

In this chapter, I present measurement results of the static magnetization with high-harmonic-generation light source using T-MOKE. The asymmetry peaks at the expected photon energies near M-shell absorption edges. In Permalloy, we measure a maximum asymmetry of 30% near the M-shell absorption edges of Fe and Ni. The experimental results agree with an independent measurement that employed synchrotron

[4] Recall that I analyze this data set from a pump-probe measurement.

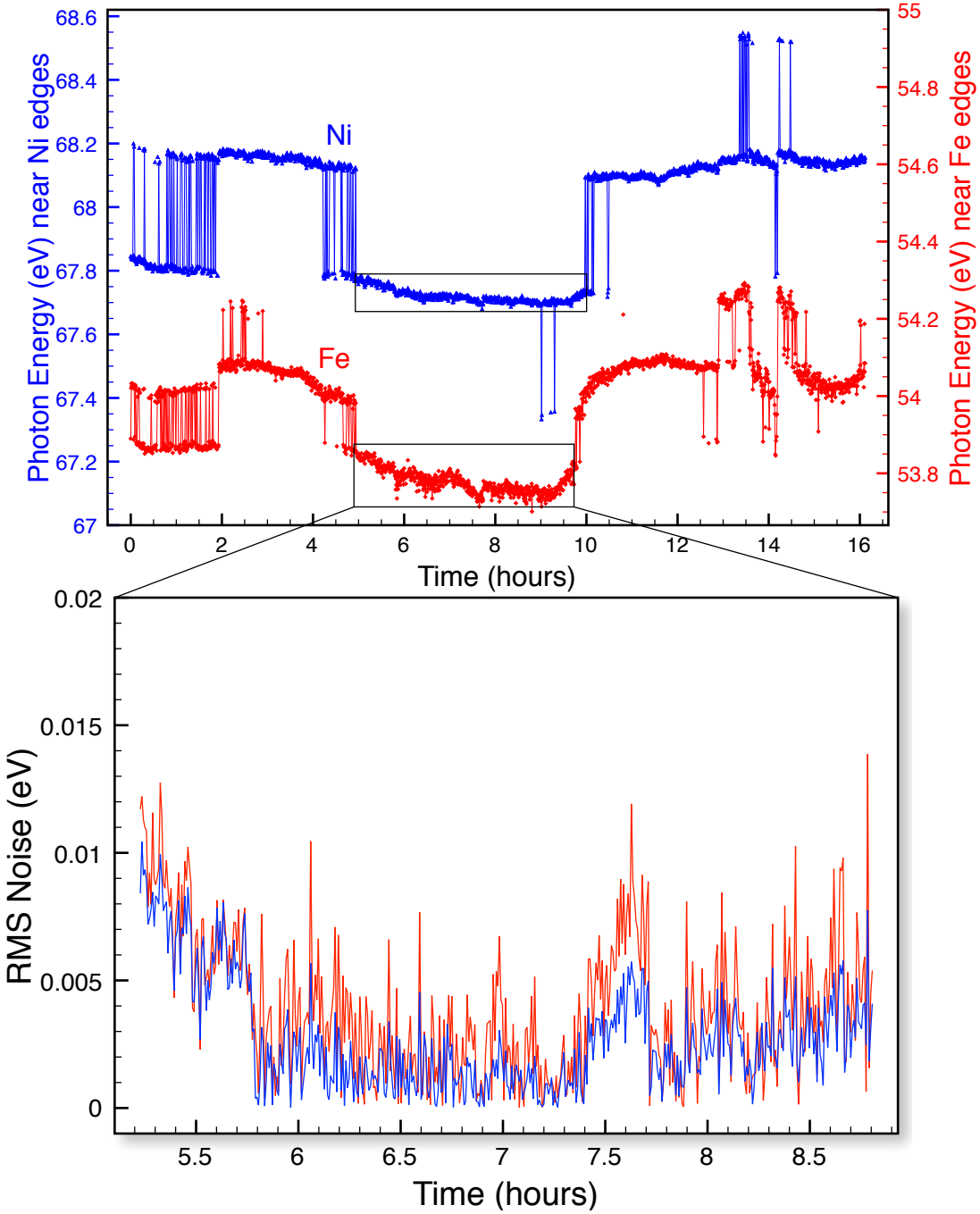

Figure 6.13: (Top) Photon energy of high harmonics calculated from the 'center-of-mass' of harmonics (Figure 6.12) near Ne (blue) and Fe (red) M-edges. The discontinuities in photon energies, e.g., at 5th or 10th hour, occur after the optimization of harmonic flux or laser timing. (Bottom) The RMS noise during the stable hours.

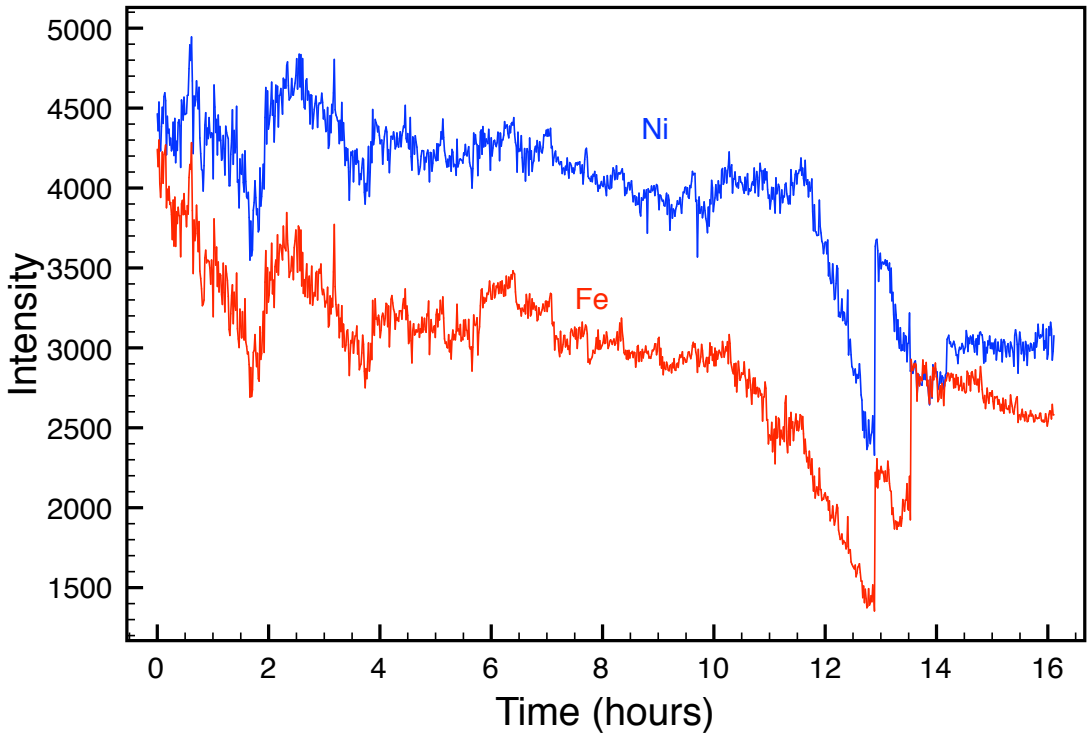

Figure 6.14: Intensities of the high harmonics near Ne (blue) and Fe (red) M-edges. The final intensity is only 70% of the starting level because of a permanent sample damage causing by constantly pumping with a laser beam.

radiation with a Permalloy. Then, static T-MOKE is used for an element-selective hysteresis measurement, a near-surface sensitivity probe of magnetic samples, and a measurement of different layers in magnetic multilayers. Moreover, I showed that photon energies of high harmonics are tunable by adjusting the laser peak power with an iris diaphragm. Finally, I analyze the stability of our high-harmonic light source. The high-harmonic photon energies are very stable as the spectra only drift by 0.3% during 16 hours of operation.

In the next two chapters, measurement of the T-MOKE magnetic asymmetries as a function of pump-probe time delay, the element-selective dynamics in Permalloys can be studied.

Chapter 7

Ultrafast Decoupling of Magnetization Dynamics for Fe and Ni in Permalloy

7.1 Introduction

In the previous chapter, I discuss the element-selective measurments of magnetizations from T-MOKE asymmetry at the photon energies near M-edges. By taking advantage of the broad photon-energy range of high-harmonic generation to cover all M-shell absorption edges of 3d ferromagnets, asymmetries from different elemental edges can be measured simultaneously, as demonstrated in the hysteresis loop measurement. In this chapter, the scope of the measurements is expanded from static to dynamic measurements by determining the magnetic asymmetry with respect to the pump-probe time delay.

This chapter covers the experimental results that compare the magnetization dynamics of Fe and Ni in Permalloy ($Ni_{0.8}Fe_{0.2}$) and Permalloy–Cu ($(Ni_{0.8}Fe_{0.2})_{0.6}Cu_{0.4}$). Our research team shows that the dynamics of the two elements are delayed with respect to each other, despite the strong exchange coupling that aligns their magnetic moments in thermodynamic equilibrium. These experimental results are fundamentally important and have not been addressed either theoretically or experimentally at the time of writing. Therefore, we introduce a phenomenological rate equation to describe the finite coupling in these materials. We interpret these delay times as the characteristic time scales of the exchange interaction.

At the time of writing, Radu et al. [130] recently reported a similar element-selective dynamics between Fe and Gd in a GdFeCo compound. This material has **ferrimagnetic** order, where the magnetic moments of Gd and Fe are oppositely aligned. The coupling between Fe and Gd sub-lattices is typically weak, and the distinct magnetization dynamics could be expected. Particularly, in GdFeCo, this material exhibits distinct temperature-dependent properties of the localized 4f ferromagnet (Gd) and the itinerant 3d ferromagnet (Fe) in thermodynamic equilibrium. As a result, the compensation point, which the magnetization of the two sub-lattices are perfectly cancel, exists. In contrast, this particular behavior does not exist in our **ferromagnetic** alloy samples. The moments for both Fe and Ni have the same temperature dependence; the delay between the two magnetic moments is not expected.

7.2 Samples: Permalloy and Permalloy–Copper

Our sample is Permalloy, which is the Ni–Fe alloy at the ratio close to 80-20. The crystal structure of Permalloy is face-center cubic with a random placement of Fe and Ni atoms. Permalloy has high magnetic permeability (μ), low coercivity (magnetic field to reduce magnetization to zero), small magnetostriction (the change of the material size when magnetized), large anisotropic magnetoresistance and giant magnetoresistance (GMR) in Permalloy/Cu/Co film [164, 165], and a good contrast between the conductivity of majority and minority electron spins [166, 167]. Because of these properties, Permalloy was used in the GMR read heads in hard-disk drives [168].

In our case, we choose Permalloy for three reasons. First, Permalloy is a soft ferromagnetic material, which only requires the small amount of magnetic field to switch the magnetization (40 Oe). We can switch the magnetic field quickly and use our Helmholtz coil with large field uniformity (Chapter 5). Second, the energy separation of M-edges of Fe and Ni in Permalloy are quite far apart (15 eV) [169] compared to the high-harmonic spacing (3 eV). As a result, the magnetic signals from both elements

do not interfere to each other, and two distinct harmonics can be assigned to Fe and Ni (Figure 6.5 and 6.6). Finally, because of it is a well-known and stable alloy, we are certain that Permalloy does not segregate into Fe and Ni-rich sections that can cause any artificial decoupled demagnetization dynamics.

We would like to study the role of the exchange coupling in the demagnetization dynamics of Fe and Ni. In the particular case of Permalloy, the interatomic exchange coupling is large as indicated by the Curie temperature (T_c) of 850 K. Therefore, the dynamics of Fe and Ni are expected to be similar. We repeat our measurements with Permalloy diluted by Cu (Permalloy–Cu). The alloying of Cu with Permalloy results in a reduction of the volume-averaged exchange parameter through the reduction of the number of ferromagnetic nearest-neighbor atoms. Such alloys also retain the high permeability associated from pure Permalloy and avoid any discontinuous crystallographic phase transitions with varying Cu content. This provides us with the ability to tune T_c over a broad temperature range (Figure 7.1). As a result, the exchange coupling is further reduced by the renormalization of the effective exchange integral near T_c [170, 171]. We choose a sample composition of $((Ni_{0.8}Fe_{0.2})_{0.6}Cu_{0.4})$ where T_c is just above the room temperature ($T_c \approx 400$ K). X-ray diffraction verifies that our samples are a solid solution of fcc phases.

The asymmetry is reduced even further at high temperature since the asymmetry is directly linked to magnetization. We measure the asymmetry as a function of temperature up to 425 K, which is above T_c. We choose to measure the asymmetry near both Fe and Ni M-edges from the harmonics at 55 eV and 68 eV, respectively (Figure 7.2). The measurement shows that the Fe and Ni asymmetries share the same temperature dependence and both asymmetries vanish at the same temperature. By fitting a power law ($A(T - T_c)^\beta$) to the magnetization curves, we can extract the Curie temperatures of Ni and Fe. The fit results give the Curie temperatures of Fe and Ni of 403.5 ± 1.1 K and 405.5 ± 3.7 K, respectively; therefore, within the error bars, Fe and

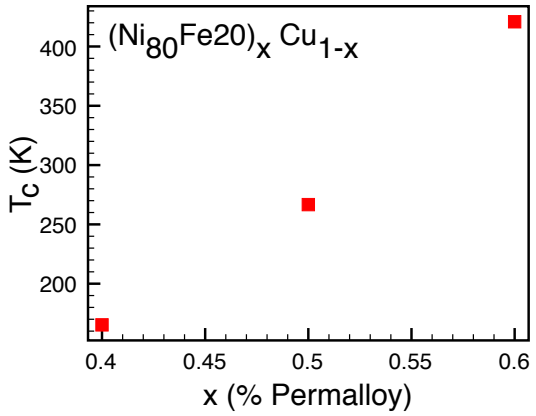

Figure 7.1: Tuning the Curie temperature of Permalloy by alloying with copper. Curie temperature is measured by superconducting quantum interference device (SQUID) magnetometry. (Data from Justin Shaw, Han Nembach, and Thomas Silva)

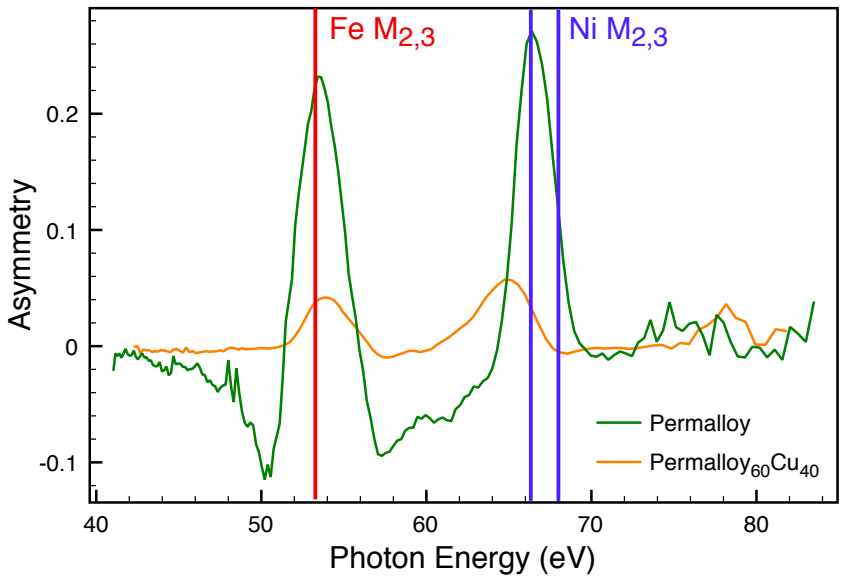

Figure 7.2: The static asymmetry spectra of Permalloy–Cu (60:40) (orange) and Permalloy (green). The asymmetry of Permalloy–Cu is six times less than that of Permalloy. Both measurements are performed at the room temperature.

Ni have the same T_c. The fact that both Fe and Ni have the same T_c in Permalloy–Cu (not 1043 K for bulk Fe and 631 K for bulk Ni, or 850K for Permalloy) implies that our sample is a single-phase alloy without any segregation between Fe, Ni and Cu. The other important fit parameter is the critical exponent β. Our fit results yield the critical exponents around 0.5 (0.467 ± 0.072 for Ni and 0.495 ± 0.084 for Fe), which is the value from Landau mean-field theory (Appendix 1).

7.3 Ultrafast Demagnetization Dynamics

To study the demagnetization dynamics, we measure magnetic asymmetry was a function of the time delay between pump and probe pulses (see the video in [172]). In Permalloy, the T-MOKE asymmetry for both Fe and Ni follows a typical shape after observed in demagnetization studies (Figure 7.4a) . Initially, the magnetization decreases rapidly down to about 30% within 500 fs, and followed by magnetization relaxation at a longer time scale of a few picoseconds. A closer inspection of the data on short timescales (Figure 7.9A) indicates that the demagnetization of Ni is delayed in comparison to that of Fe by approximately 10-20 fs. This delay for Ni in Permalloy was not previously observed in our early publication [63] because the temporal resolution in that experiment and the data quality were not sufficient enough to resolve such a small shift of the demagnetization. A delay of the demagnetization dynamics in Permalloy at ultrafast timescales was not expected as Fe and Ni are strongly coupled via exchange.

For Permalloy-Copper, the demagnetization dynamics of Fe and Ni are clearly different from that of Permalloy with the same pump fluence (Figure 7.4b) in four characteristics. (1) The demagnetization time is significantly slower. The asymmetries slowly reach their minima within a picosecond comparing to 500 fs in Permalloy. (2) The asymmetry recoveries are very slow, and cannot be resolved within the time window of our scan, although the scan range is extended to 150 ps (Figure 7.5). (3) The asymmetries of Fe and Ni are both quenched by 80%, which is significantly larger

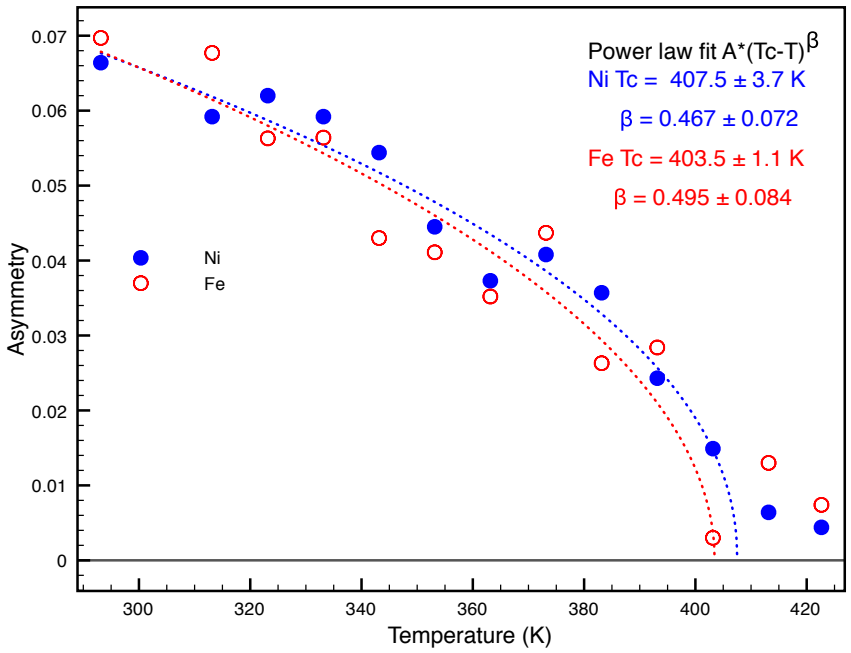

Figure 7.3: Static asymmetry of Permalloy–Cu as a function of temperature. Asymmetries near M-edges of Fe and Ni are presented in red and blue respectively. Power law fits give the direct determination of Curie temperature (T_c) and critical exponent (β), which have the same results for both Fe and Ni.

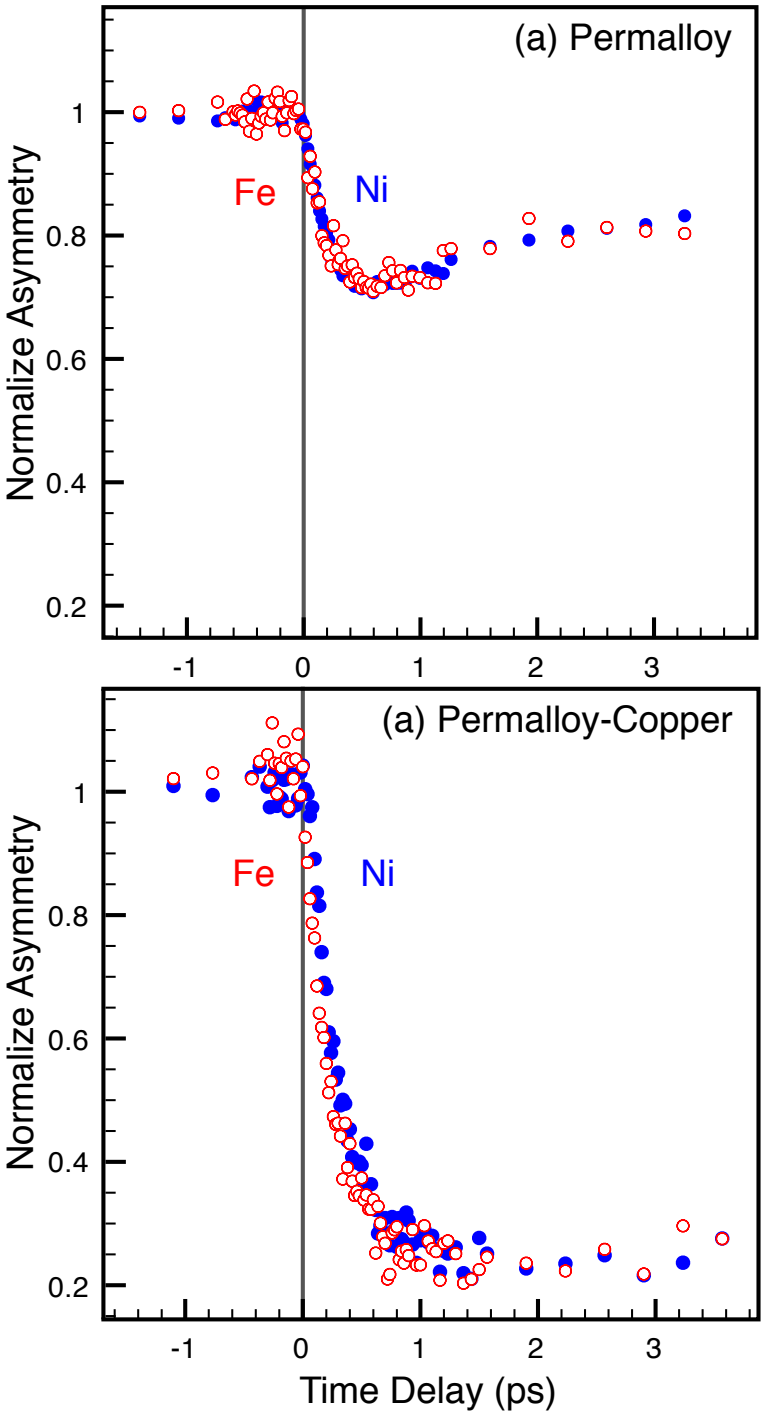

Figure 7.4: The ultrafast demagnetization dynamics of Ni (blue) Fe (red) in (a) Permalloy and (b) Permalloy–Cu. Both dynamics are measured with the same pump fluence ($2\ mJ/cm^2$).

than those of Permalloy. (4) Upon close inspection near time zero (Figure 7.8B), we unambiguously observe a delay in the dynamics between Ni and Fe, reenforcing the observation in Permalloy.

Characteistics (1-3) can be understood by the low Curie temperature of our Permalloy–Cu sample (T_c = 400 K) and thermodynamics. A larger amount of quenching for a give fluence is expected when the samples' temperature approaches the Curie point when the magnetization is a more sensitive function of temperature; a slight change in temperature causes a large reduction in magnetization. The slow-down of both the demagnetization and recovery times comes from the higher spin heat capacity near the Curie temperature (Figure 8.6). The closer the system is driven to Curie temperature, the more amount of heat is required to increase the spin temperature. Moreover, the slow down of dynamical behavior agrees with theoretical predictions of 'critical slowing-down' dynamics near Curie point [173, 146].

These explanations cannot account for the delayed demagnetization dynamics between Fe and Ni, and we attribute the larger demagnetization delay to the reduction of exchange coupling, which I will discuss in the next two sections. However, I would like to first argue that this observed delayed does not originate from three possible experimental errors. First, the distinct demagnetization dynamics are not the result of time-zero determination error because we extract the demagnetization dynamics for Fe and Ni simultaneously from the whole high-harmonic spectra. Second, chirp of the high-harmonic spectra, which might cause the time delay between every Fe and Ni probe pulses, cannot cause the delay because the observed delay of demagnetization dynamics in Permalloy–Cu (60 fs) is significantly larger than a typical high-harmonic pulse duration (<10 fs). Finally, our research group thoroughly characterize of our samples to prove that our samples are single-phase alloys with no segregation between Fe and Ni.

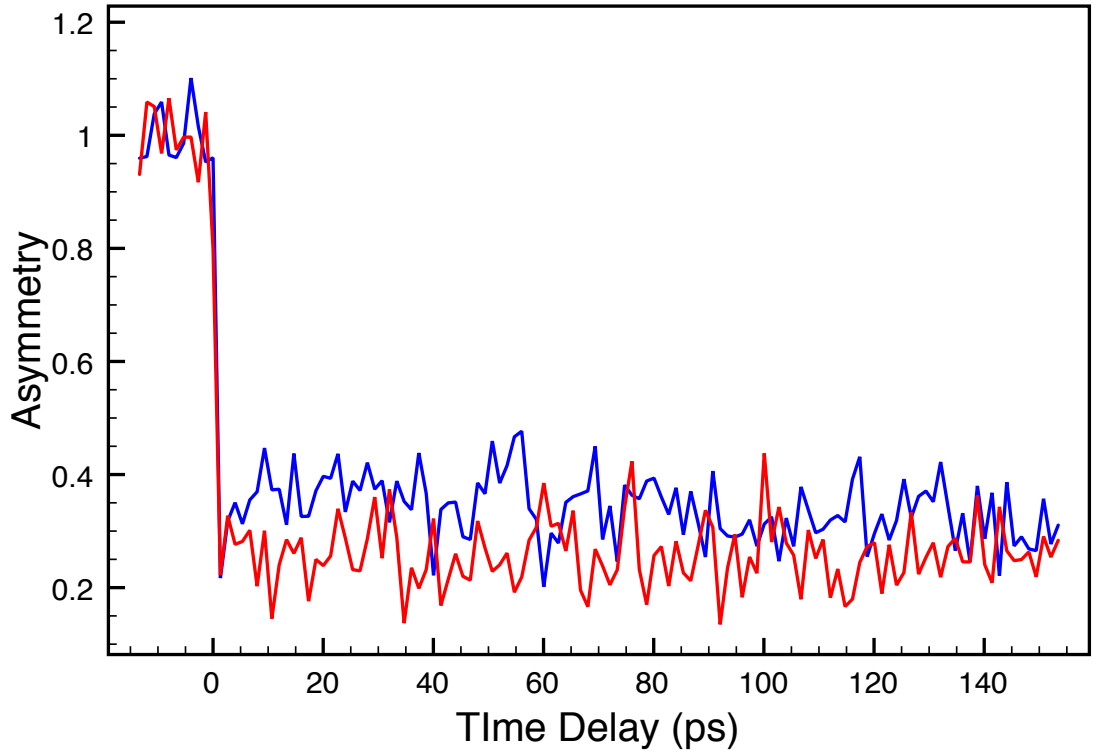

Figure 7.5: The long time scan of the asymmetry dynamics (up to 150 ps). Permalloy-Copper shows no recovery of the asymmetry indicating the slow down of the magnetization recovery time near Curie temperature.

7.4 Rate Equations for Coupled-demagnetization Dynamics

To my present knowledge, there is no theoretical approach to describe this delay dynamical behavior, and the behavior has never been observed by any experimental approach. In the work by Radu et al. [130], the demagnetization dynamics of Fe and Gd are also distinctive during the early time scale, but they demagnetize independently rather than the delayed behavior. To gain a more physical insight, Thomas Silva, from NIST Boulder, posited the following phenomenological model to describe our experimental data with coupled first-order rate equations,

$$\begin{aligned} \frac{dm_F}{dt} &= \frac{-m_F}{\tau_F} - \frac{m_F - m_N}{\tau_E} \\ \frac{dm_N}{dt} &= \frac{-m_N}{\tau_N} - \frac{m_N - m_F}{\tau_E}, \end{aligned} \tag{7.1}$$

where m_F and m_N are the normalized Fe and Ni magnetizations (asymmetries), τ_F and τ_N are the elemental decay times for Fe and Ni in the absence of exchange coupling, and τ_E is the characteristic **exchange time** described the coupling between Fe and Ni systems. The motivations of the model equations come from the following three observations:

(1) The model assumes that each elements have exponential dynamics. Phenomenologically, the demagnetization dynamics can be very well represented by exponential functions. For example in Reference [139], the transient MOKE signals were very well fit with the following function,

$$f(t) = A(1 - e^{-\frac{t}{\tau_M}})e^{-\frac{t}{\tau_R}} + B(1 - e^{-\frac{t}{\tau_R}}), \tag{7.2}$$

where τ_M is the demagnetization time, τ_R is the magnetization recovery time, A is the exponential amplitude to describe the amount of the demagnetization, and B is the amount magnetization at longer time delay which is typically a small number comparing to A (Figure 7.6).

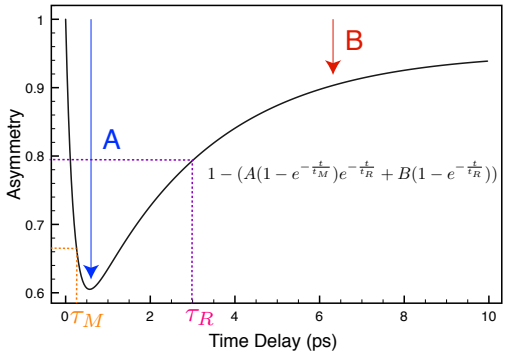

Figure 7.6: The phenomenological description of demagnetization dynamics by an exponential model.

The exponential-like shape of the demagnetization dynamics can be understood thermodynamically from a three-temperature model that has exponential solutions with some approximations (Equation 4.4).

(2) To account for distinct demagnetization dynamics between Fe and Ni at early time delay, we assign the element-specific demagnetization times for Fe and Ni (τ_F and τ_N).

(3) To consider the exchange coupling, we define the second exponential term to damp down any difference between m_F and m_N with a time constant τ_E.

7.4.1 Analytical Solutions

The rate equation can be solved analytically with a standard differential equation technique. First, I write the equation in the form of

$$\begin{pmatrix} \frac{dm_F}{dt} \\ \frac{dm_N}{dt} \end{pmatrix} = \begin{pmatrix} -\frac{1}{\tau_F}-\frac{1}{\tau_E} & \frac{1}{\tau_E} \\ \frac{1}{\tau_E} & -\frac{1}{\tau_N}-\frac{1}{\tau_E} \end{pmatrix} \begin{pmatrix} m_F \\ m_N \end{pmatrix} = \mathbf{A} \begin{pmatrix} m_F \\ m_N \end{pmatrix}. \tag{7.3}$$

Then, I diagonalize the matrix $\mathbf{A}$ to write the solutions in the term of its eigenvalues ($\lambda_\pm$) and eigenvectors ($\nu_\pm$) in the form of $\begin{pmatrix} m_F \\ m_N \end{pmatrix} = \mathbf{c_1}\nu_+ e^{-\lambda_+ t} + \mathbf{c_2}\nu_- e^{-\lambda_- t}$. The

final function is convenient by introducing the two "reduced time" parameters defined as:

$$\bar{\tau} = \frac{\tau_N \tau_F}{\tau_N + \tau_F} \tag{7.4}$$

$$\widetilde{\tau} = \frac{\tau_N \tau_F}{\tau_N - \tau_F}. \tag{7.5}$$

The eigenvalues and eigenvectors of $\mathbf{A}$ are

$$\lambda_{\pm} = \frac{1}{2}\left(\frac{1}{\bar{\tau}} + \frac{2}{\tau_E} \pm \frac{\sqrt{\tau_E^2 + 4\widetilde{\tau}^2}}{\tau_E \widetilde{\tau}}\right) \tag{7.6}$$

$$\begin{pmatrix} -\nu_+ \\ 1 \end{pmatrix}, \begin{pmatrix} -\nu_- \\ 1 \end{pmatrix} \tag{7.7}$$

where $\nu_{\pm} = \frac{\tau_E \mp \sqrt{\tau_E^2 + 4\widetilde{\tau}^2}}{2\widetilde{\tau}}$. Therefore, the solutions of Equation 7.1 are

$$\begin{aligned} m_F &= -c_1 \nu_- e^{-\lambda_+ t} - c_2 \nu_+ e^{-\lambda_- t} \\ m_N &= c_1 e^{-\lambda_+ t} + c_2 e^{-\lambda_- t}. \end{aligned} \tag{7.8}$$

The final step is to apply the initial condition to find the coefficients c_1 and c_2. The simplest way is to normalized the initial dynamics to unity ($m_F(t=0) = m_N(t=0) = 1$). These particular solutions for this initial condition are

$$\begin{aligned} m_F &= \frac{1+\nu_+}{\nu_- - \nu_+}\nu_- e^{-\lambda_+ t} - \frac{1+\nu_-}{\nu_- - \nu_+}\nu_+ e^{-\lambda_- t} \\ m_N &= -\frac{1+\nu_+}{\nu_- - \nu_+} e^{-\lambda_+ t} + \frac{1+\nu_-}{\nu_- - \nu_+} e^{-\lambda_- t}. \end{aligned} \tag{7.9}$$

In our publication [174], we write the solutions in different forms by use of the relations,

$$\begin{aligned} 1 - \nu_- &= -(1+\nu_+)\nu_- \\ -(1-\nu_+) &= -(1+\nu_-)\nu_+ \\ (1-\nu_-)\nu_+ &= 1+\nu_+ \\ (1-\nu_+)\nu_- &= 1+\nu_-. \end{aligned} \tag{7.10}$$

7.4.2 Special Cases

I consider three special cases for the solutions (Equation 7.9) to our model equations (Figure 7.7): short exchange time, long exchange time, and long intrinsic demagnetization time for Ni. Although the detailed dynamical behaviors are different in these special cases, they all have two common features. (1) Initially, the dynamics of Fe (red) and Ni (blue) behave independently for times shorter that the exchange time (green vertical lines). (2) At longer times, the elemental dynamics for both Ni and Fe converge to the same value as expected by the introduction of the term proportional to the exchange-time parameter.

In the first special case, when the exchange time is short comparing to τ_F and τ_N (Figure 7.7a), both elements behave almost identically except for the initial part. This behavior agrees with the experimental finding in the case of Permalloy.

Second, when the exchange time is long comparing to τ_F and τ_N (Figure 7.7b), both elemental dynamics become more clearly distinctive and behave almost as if they are independent. This behavior describes the systems with weak exchange coupling, such as when Fe and Ni are fully phase-segregated or, for this thesis, in the binary grating (Chapter 8).

Third, when the demagnetization time constant of one element, e.g. Ni, approaches infinity ($\tau_N \rightarrow \infty$), the dynamics behave such that the magnetization of the other element (Fe) reduces fairly quickly and then 'drags down' the other element by the exchange coupling. As a result, the dynamics of the slower element are simply 'delayed' with respect to the fast element. This type of dynamics fits our demagnetization results from Permalloy–Cu[1] . To put this special case into an extreme, I consider the limit of $\tau_N \rightarrow \infty$ and $\tau_E \ll \tau_F$ of the solutions of our model equations up to the first order in

[1] Also for Permalloy but since the exchange time is also short in this case, the dynamics also behave like in the first special case (short τ_E)

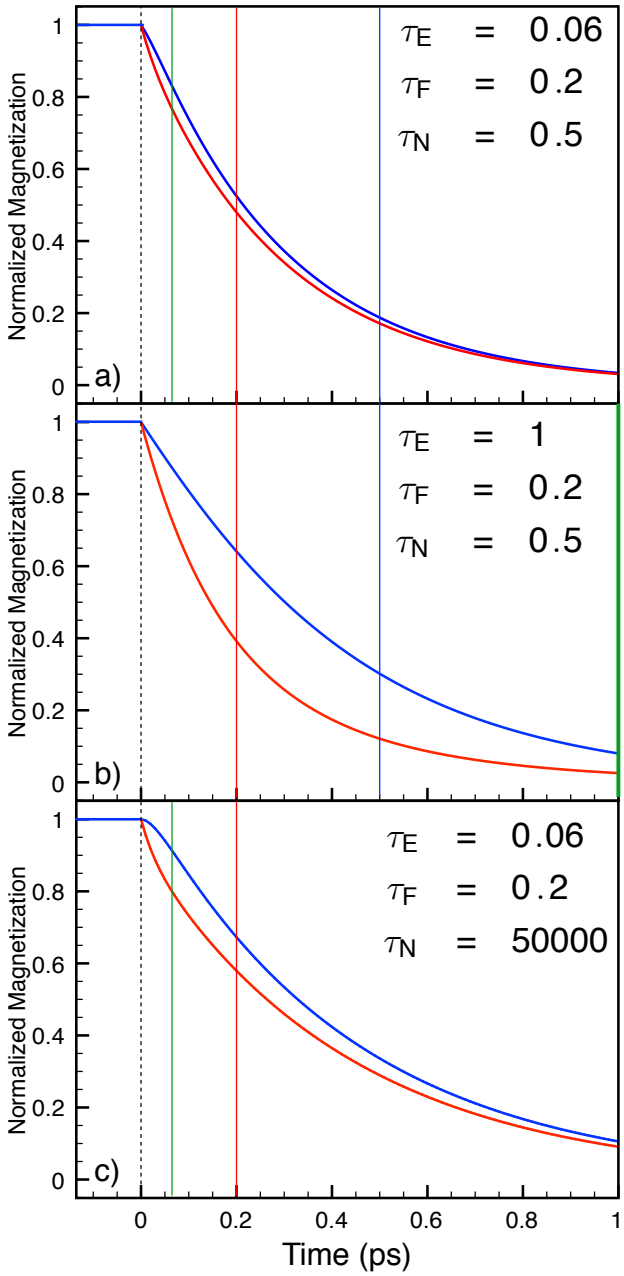

Figure 7.7: Solutions to the rate equation to describe the delayed demagnetization dynamics in three different special cases: (a) short exchange time τ_E, (b) long exchange time, and (c) long nickel demagnetization time (τ_N). The demagnetization dynamics of Ni and Fe are plotted in blue and red, respectively. The time constants for Ni, Fe and the exchange time are indicated by blue, red, and green vertical lines, respectively. The time zero is shown in the dashed line.

$\frac{\tau_E}{\tau_F}$ (Equation 7.9),

$$\bar{\tau} = \widetilde{\tau} = \tau_F \tag{7.11}$$

$$\lambda_+ = \frac{2}{\tau_E} + \frac{1}{2\tau_F}(1 + \frac{\tau_E}{4\tau_F}) \tag{7.12}$$

$$\lambda_- = \frac{1}{2\tau_F}(1 - \frac{\tau_E}{4\tau_F}) \tag{7.13}$$

$$\nu_\pm = \mp 1 + \frac{\tau_E}{2\tau_F} \tag{7.14}$$

$$m_F = \frac{\tau_E}{4\tau_F} e^{-\frac{2t}{\tau_E}(1+\frac{\tau_E}{4\tau_F})} + (1 - \frac{\tau_E}{4\tau_F}) e^{-\frac{t}{2\tau_F}} \tag{7.15}$$

$$m_N = -\frac{\tau_E}{4\tau_F} e^{-\frac{2t}{\tau_E}(1+\frac{\tau_E}{4\tau_F})} + (1 + \frac{\tau_E}{4\tau_F}) e^{-\frac{t}{2\tau_F}} \tag{7.16}$$

The special case (Equation 7.11 and 7.16) indicates that the dynamics are no longer controlled by Ni, and the dynamics will behave closely to exponential decay functions with the time constant of twice the demagnetization time constant of Fe after dropping all the first order terms in $\frac{\tau_E}{\tau_F}$.

Before moving on, this solution to the model equations only allows for a fully demagnetization (i.e. quenched by 100%). Moreover, the equations do not account for the magnetization recovery. Therefore, we need to include these extra phenomenological behaviors by modifying the solutions (Equation 7.9) such that

$$m_F \rightarrow A(m_F - 1)e^{(-\frac{t}{t_R})} + 1, \tag{7.17}$$

where A is the amount of demagnetization quenched and τ_R is the recovery time.

7.5 Analyzing the Demagnetization Dynamics

7.5.1 Extracting the Demagnetization Time from Exponential Fits: The Delay of Demagnetization Dynamics

Before considering the data fitting to the model equations, I start with the data analysis from a simple exponential equation (Equation 7.2) to show that this simple exponential equation cannot simultaneously describe the demagnetization dynamics of

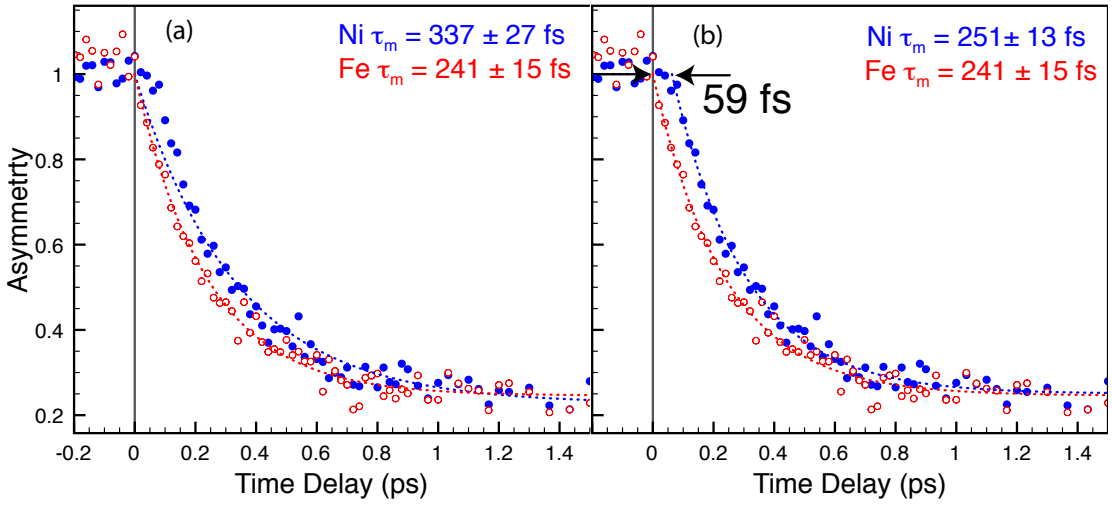

Figure 7.8: The delay of demagnetization dynamics of Fe (red) and Ni (blue) in Permalloy–Cu. (a) The time zero is set to Fe data. During the short time delay, exponential equation can only describe Fe data. In this case, Ni demagnetizes slower than Fe by about 100 fs. (b) When the time zero from Ni is 'delayed' by 59 fs with respect to Fe, the exponential fit to Ni is improved. In this case, both elements have the same demagnetization time.

Table 7.1: Permalloy Fit Results by Exponential Equation

	Fe		Ni	
Parameters	Results	Errors	Results	Errors
A	0.3221	0.0243	0.3475	0.0126
$\tau_M(fs)$	199	34	222	17
$\tau_R(ps)$	5.0	1.4	4.1	0.4
Δt (fs)			19	0.4
$\tau_M(fs)$			197	13

Fe and Ni. I present only results from Permalloy–Cu because of the much more visible amount of the delay between Fe and Ni. Since the Permalloy–Cu data show no recovery of the magnetization at long times, the recovery time is set to infinity without disrupting the fit results (Figure 7.8a). From the fit, only Fe follows the exponential trend; while Ni is poorly fit with the model, as can be measured from its error bar size.

Alternatively, an improvement of the fitting result to the Ni data can be achieved by moving the time zero of the exponential fit equation of Ni with respect to Fe 59 fs (Figure 7.8b). This time shift can be calculated by minimizing the mean square error of the fit to the Ni data. After delaying Ni with respect to Fe, the error bar size of Ni is reduced the same level as Fe, and the demagnetization times of Fe and Ni become very similar. Although the fit results are improved, this arbitrary shift of the time zero is unphysical since our measurement technique locks the time axis for Fe and Ni together.

This delay behavior also exists in Permalloy but the time shift is smaller (19 fs). Table 7.1 and 7.2 summarize the fit results for Permalloy and Permalloy–Cu, respectively. The top parts of both tables show the fit results when no time zero is shifted

Table 7.2: Permalloy-Copper Fit Results by Exponential Equation

	Fe		Ni	
Parameters	Results	Errors	Results	Errors
A	0.7609	0.0115	0.7817	0.0190
$\tau_M(fs)$	241	15	337	27
Δt (fs)			59	0.6
$\tau_M(fs)$			251	13

Table 7.3: Permalloy Fit Results by Model Equations

Parameters	Results	Errors
A	0.345	0.007
$\tau_E(fs)$	14	6
$\tau_F(fs)$	94	6
$\tau_N(10^4$ ps)	10	0.3
τ_R (ps)	6.45	0.57
τ_M (fs)	151	15

between Fe and Ni; while the bottom parts show the results when the zero of Ni is delayed by Δt with respect to Ni. Again for Permalloy, the demagnetization time of Fe and Ni becomes equal after considering the shift of time zero.

7.5.2 Extracting the Exchange Time through the Model Equations

In addition to the model with exponential fits with time shift (Δt), our differential equation (Equation 7.1) can reproduce the behaviors found in both Permalloy and Permalloy–Cu (Figure 7.9). The fit parameters are summarized in Table 7.3 and 7.4. For Permalloy and Permalloy–Cu, both fits give fast time constants for Fe ($\sim$ 100 fs) and infinitely large time constants for Ni ($\sim 10^6$ ps), i.e. $\tau_N \gg \tau_F$. The fits to the model show that, after the characteristic exchange time τ_E, the Ni magnetization, which is initially nearly unaffected by the pump pulse, is dragged down by the rapidly demagnetizing Fe. The intrinsic demagnetization time of Fe (τ_F) is close to one half of the time scale of the exponential-decay demagnetization time as discussed above from a proper limit of the analytic equation (Equation 7.16).

By considering the exchange-time constant (τ_E), it is very tempting to relate this exchange times to the exchange energy (E_{Ex}) of ferromagnetic systems via the time-energy product $E_{Ex}\tau_E = h$. To estimate the ratio of the exchange energy, the ratio of the Curie temperature for Permalloy to Permalloy–Cu is 2.1, which is the ratio of exchange energy at 0 K ($\frac{E_{ExPermalloy}}{E_{ExPermalloy--Cu}}$). At room-temperature, we also need to account for the renormalization of exchange by scaling the magnetization ratio $\frac{M(T)}{M(T=0)}$. The ratio of this

Table 7.4: Permalloy-Copper fit Results by Model Equations

Parameters	Results	Errors
A	0.77	0.01
$\tau_E(fs)$	66	6
$\tau_F(fs)$	112	5
$\tau_N(10^6$ ps)	1.45	0.03
τ_R (ps)	115	103
τ_M (fs)	199	34

quantity is 1.56 for Permalloy–Cu, according to the SQUID data; therefore, the ratio of exchange energies between Permalloy and Permalloy–Cu at **room temperature** is about $1.56 \times 2.1 = 3.3$. The ratio of the exchange times (τ_E) extracted from our data for Permalloy–Cu to Permalloy is $4.7^{+4.3}_{-1.7}$. Thus, the scaling of the exchange energy and the exchange time τ_E between Permalloy and Permalloy–Cu are compatible with our interpretation. Moreover, to numerically estimate the exchange energy directly from the time-energy product, the exchange energy is about 0.3 eV for Permalloy, which is in the right order of magnitude [11].

Our interpretation is very promising; the exchange time can be extracted from a simple phenomenological model, and a simple inverse relationship between exchange time and the exchange energy. However, we only measure two samples with two distinctive ranges of the exchange coupling. In the future, it would be interesting to repeat the study for samples with a broader range of exchange coupling by alloying Permalloy with different amount of copper or by elevating the sample temperature to reduce the exchange coupling via exchange renormalization.

7.6 Fluence-Dependent Demagnetization Dynamics and the Role of Hot Electrons

To understand more concerning the microscopic mechanism of delayed magnetization dynamics, we consider the role of hot electrons, which are directly related to a microscopic picture of demagnetization dynamics. Initially, a laser pulse coherently

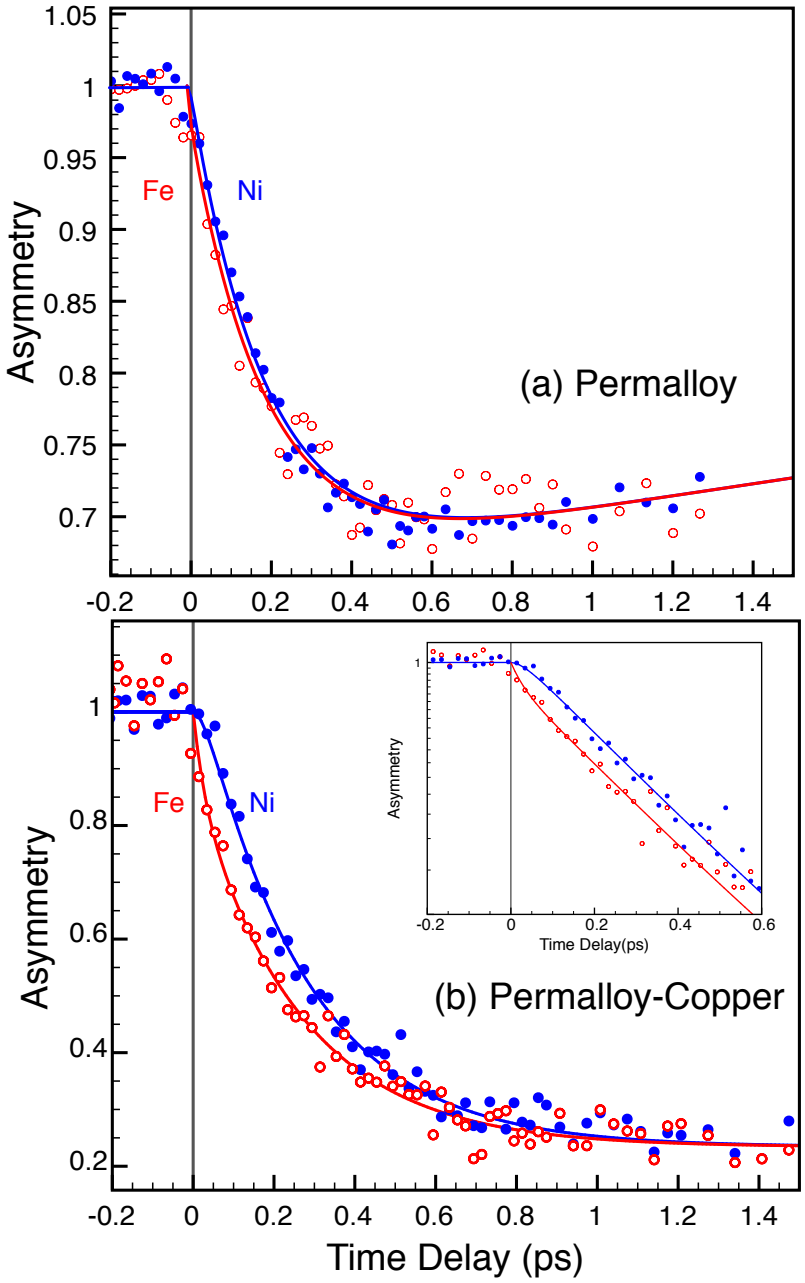

Figure 7.9: Explaining the dynamics of Permalloy and Permalloy–Cu by the model equations (Equation 7.1). The model describes both data very well without assuming the time zero shift between Fe and Ni as in Figure 7.8b. The inset shows the log-scale plot to visualize that Fe and Ni demagnetize at the same rate after the exchange time ($\tau_{Ex} = 66 \pm 6$ fs).

interacts with electrons in the material within $\approx 0 - 50$ fs [10], creating hot electrons. Subsequently, the hot electrons relax to a thermalized population, accompanied by a spin-flip scattering process that lead to ultrafast demagnetization on timescales of $\approx$ 100 - 500 fs [9, 142, 21, 148]. The details of the scattering process remain the subject of an intense debate (Chapter 4). Since the time-scale for hot-electron dynamics is about the same time scale of the measured exchange times (Permalloy $\tau_E = 14$ fs, Permalloy–Cu $\tau_E = 66$ fs), it is therefore important to include the laser-induced hot electrons in the discussion of the magnetic dynamics at such ultrashort < 100 fs time scales. Hot electrons can screen the Coulomb potentials on femtosecond time scales [175, 57]. Such screening might also reduce the exchange interaction in ferromagnetic conductors [176]. If the screening really reduces the exchange coupling, we would expect a strong dependence of the exchange time on the pump fluence.

We study the fluence-dependent demagnetization dynamics for Permalloy-Copper by attenuating the pump power (Figure 7.10). By slightly decreasing the pump power (350 mw to 250 mw), the quenching of the T-MOKE magnetic asymmetry is significantly reduced (80 % to 50 %). With the exponential fit equation, we observe a linear relationship between the pump fluence and the demagnetization amplitude (A) (Figure 7.11). On the other hand, the demagnetization time constants, τ_M, have a weakly decreasing trend with fluence.

By performing the model-equation fit, we can extract the exchange time parameter τ_E to quantitatively account for the delay of Fe and Ni dynamics. For our fluence-dependent dynamics, the exchange time does not show any large dependence on the pump fluence (Figure 7.12). All fiting results report similar values if around 80 fs for τ_E, as opposed to a strongly decreasing trend with the fluence, as would be expected if hot-electron screening really reduces the exchange coupling. Therefore, we rule out the hot-electron screening mechanism for the demagnetization delay between Ni and Fe.

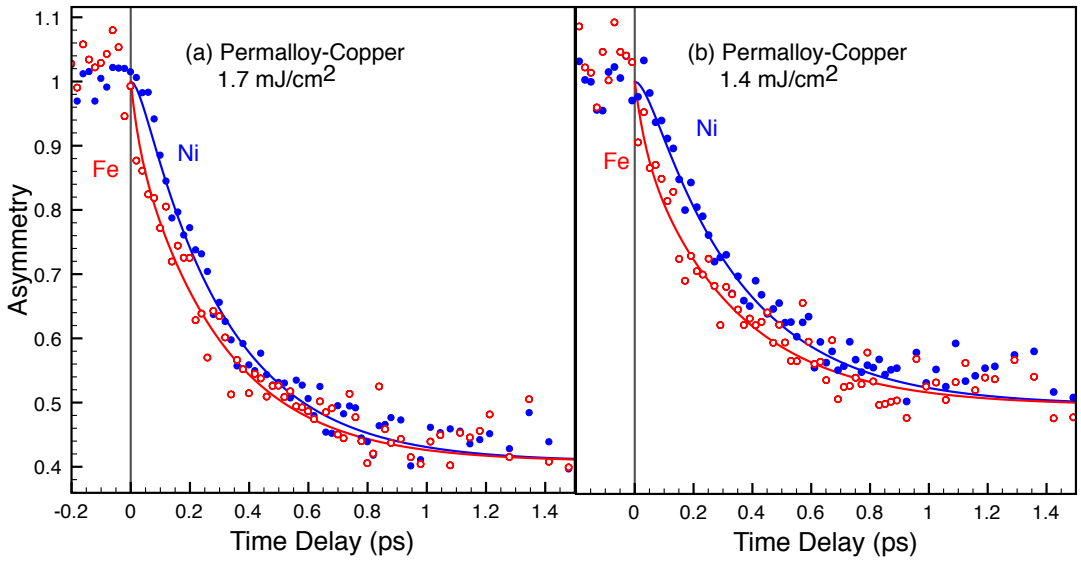

Figure 7.10: Fluence-dependent demagnetization dynamics of Ni (blue) Fe (red) in Permalloy–Cu with the fluences of (a) 1.7 and (b) 1.4 mJ/cm^2.

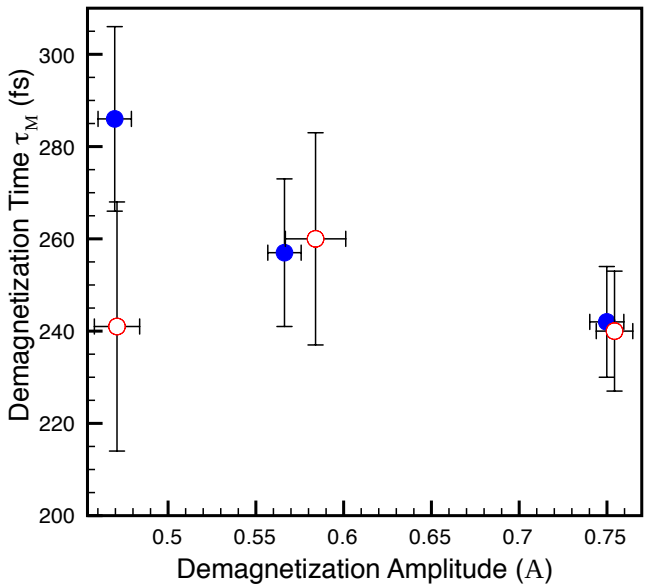

Figure 7.11: Demagnetization time (τ_M) as a function of demagnetization amplitude of Fe (red) and Ni (blue) in Permalloy–Cu.

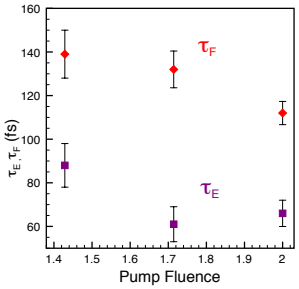

Figure 7.12: Intrinsic demagnetization time for Fe (τ_F) and exchange Time (τ_E) (defined in Equation 7.1) as a function of pump fluence. Both parameters are not the strong increasing functions of laser fluence, and we can rule out the hot-electron screening mechanism for the decoupling of demagnetization delay between Ni and Fe.

7.7 Grating Artifacts

Besides hot-electron screening effects, the observed dynamics might originate from the grating structure fabricated into our samples. These grating structures may alter the magneto-optical measurements, as evident in the hysteresis measurements from various diffraction orders [177]. In this section, I present convincing results showing that the grating structures do not change the observed ultrafast dynamics reported earlier. I compare the demagnetization dynamics measured from the two orders of diffraction from Permalloy. Earlier, the demagnetization dynamics is analyzed from the first order diffraction ($m = 1$). The dynamics is compared with that measured from the second order diffraction ($m = 2$) at identical photon energies. The two diffraction orders give the same dynamics within the error bars (Figure 7.13). This measurement confirms that the grating structures do not contribute any spurious signal to our time-resolved measurements. The same comparison is repeated for Fe in Permalloy–Cu by comparing between the $m = \pm 1$ orders (Figure 7.14).

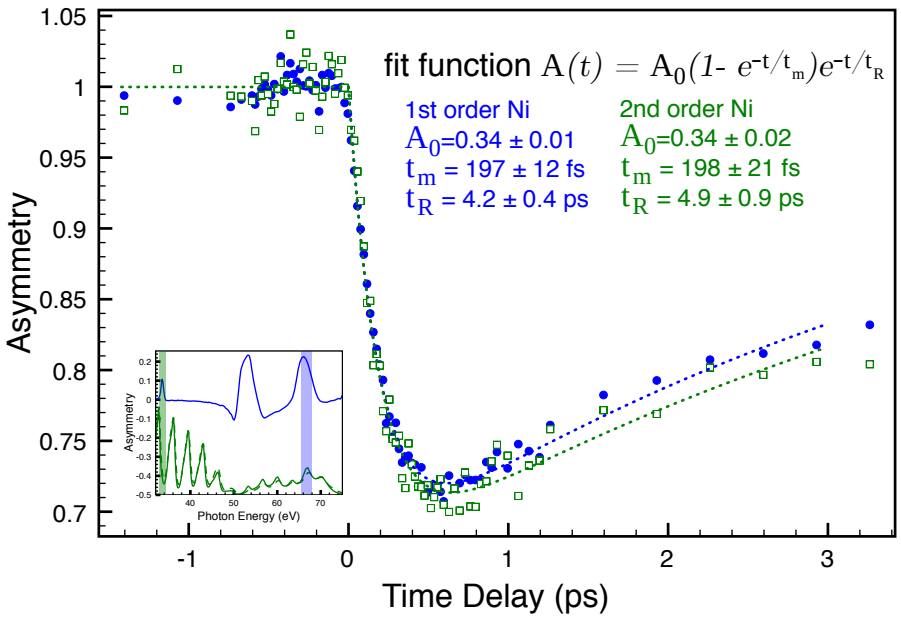

Figure 7.13: The grating structure does not artificially contribute to the time-resolved dynamics. The demagnetization dynamics of Ni in Permalloy are extracted from the first (blue) and second order (green) of the 65.6 eV harmonic. Both fit results are identical within the error bars.

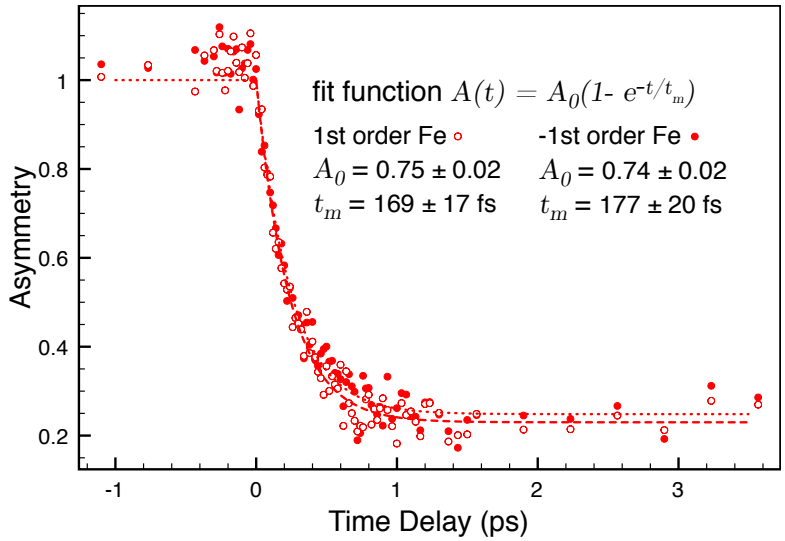

Figure 7.14: A similar comparison between the demagnetization dynamics of Fe in Permalloy–Cu extracted from the $m = +1$(blue) and $m = -1$ order (green) of the 54 eV harmonic.

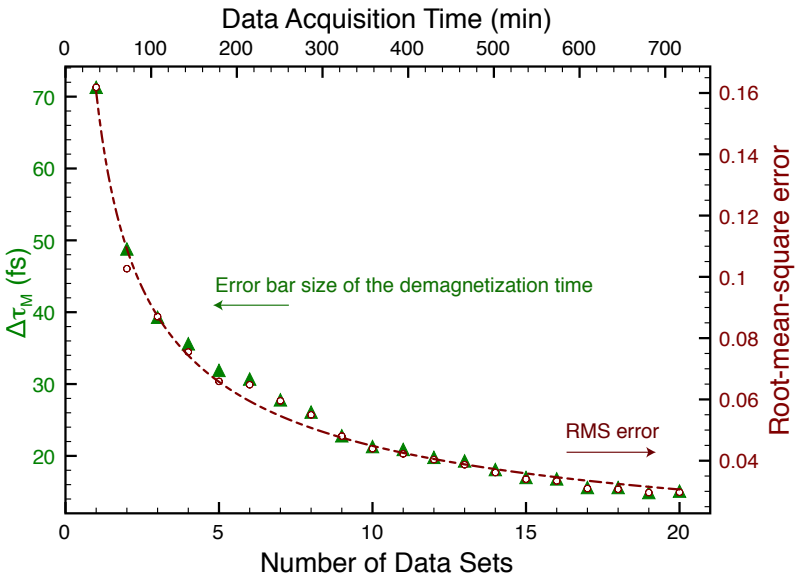

Figure 7.15: Error-bar size from the exponential fit of the demagnetization time (τ_M) (green triangles) and the corresponding RMSE (brown open circles) as a function of the number of data and total acquisition time. The power law fit to the data gives almost an inverse-square relationship between the error and acquisition time. The data set is from Ni in Permalloy–Cu (Figure 7.8b).

7.8 Signal-to-noise Analysis

I would like to conclude the chapter with the error analysis of our time-resolved data to to estimate the required acquisition time needed for our measurements at the present stage. I estimate the error by calculating two parameters: (1) the error bars of the demagnetization time (τ_M) and (2) root-mean-square error (RMSE)[2] of the fit. Both parameters are ploatted as a function of data acquisition time (Figure 7.15). For Permalloy–Cu dynamics, presented earlier (Figure 7.8b), both error parameters behave in a similar way; therefore, they can both represent the quality of data. By fitting both curves with a power law, $y = \frac{A}{x^n}$, the errors scale down almost as an inverse square ($n \approx 0.55$). This means that to decrease the error bars by a factor of two, the acquisition time must be prolonged by a factor of four. For the present experimental conditions, we require at least ten hours of acquisition to determine demagnetization times with the errors within 20%. In the future, we wish to reduce the acquisition time by upgrading the laser to give higher high-harmonic flux by operating at higher repetition rate.

7.9 Conclusions

We observe that the demagnetization dynamics of Fe and Ni in Permalloy and Permally-Cu are delayed with respect to each other at the early times (<100 fs). This delayed behavior of magnetization dynamics has not been previously predicted or observed in any metallic alloys. We prove that the observed delays do not originate from hot-electron screening or experimental errors such as time error, sample phase segregation, and grating artifact. We propose a phenomenological model to describe this surprising behavior by introducing an extra factor involving the exchange time. We

[2] The RMSE is defined as

$$RMSE = \sqrt{\frac{\sum_i^N ((y_i(x_i) - y_{fit}(x_i))^2}{N}} \tag{7.18}$$

where $y_{fit}(x_i)$ is the resultant fit function evaluated at each data point, x_i. For our case, the function is in the form of Equation 7.2.

estimate the exchange time of 14 fs for Permalloy and 66 fs for Permalloy-Copper. To interpret this exchange time as a characteristic time of the exchange energy, we point out that our measured exchange times are reasonable values when assuming that it is inversely proportional to the exchange energy. However, to confirm this observation, we need to perform additional systematic studies on Permalloy with different Cu concentrations or at elevated sample temperatures.

In additional, our phenological approach cannot explain why the intrinsic demagnetization times extracted for Ni (τ_N) are significantly larger when compared to Fe (τ_F). We can only point out that, for some unknown reasons, Fe spins are strongly affected by hot electrons, while the effect on the Ni moment is much weaker. To confirm our measurement results, I present results in the next chapter that give a direct comparison between the demagnetization dynamics of elemental Fe and Ni to show that Fe indeed demagnetizes faster than Ni in its elemental form.

Chapter 8

A Direct Comparison between the Ultrafast Demagnetization Dynamics of Fe and Ni

8.1 Introduction

In this chapter, I present an experimental comparison between the demagnetization times (τ_M) of pure Fe and Ni. No systematic experiment has compared both dynamics with identical experimental conditions. In the past, many studies focused on Ni because of its low Curie temperature of 627 K, comparing to that of Fe of 1043 K, and the reported demagnetization times of Ni span from 70 to 300 fs (Figure 8.1). In contrast, to my knowledge, there is only one reference for the demagnetization time of Fe, varying from 50 to 80 fs [178].

We employed the element selectivity of extreme ultraviolet light from high-harmonic generation to probe demagnetization dynamics of Fe and Ni with identical experimental conditions. We measured the magnetizations of both elements in parallel with identical pump fluence, time zero, probe pulse duration and sample structures. These identical experimental conditions ensure that Fe and Ni dynamics are equivalent since the measured demagnetization rate is affected by all of those factors. First, demagnetization time depends significantly on pump fluence: the stronger pump fluence, the slower the demagnetization time. Second, experimental errors, such as zero-delay determination and probe-pulse duration, can contribute to the demagnetization-time measurement. Finally, the models used to extract the demagnetization dynamics by fitting to the data

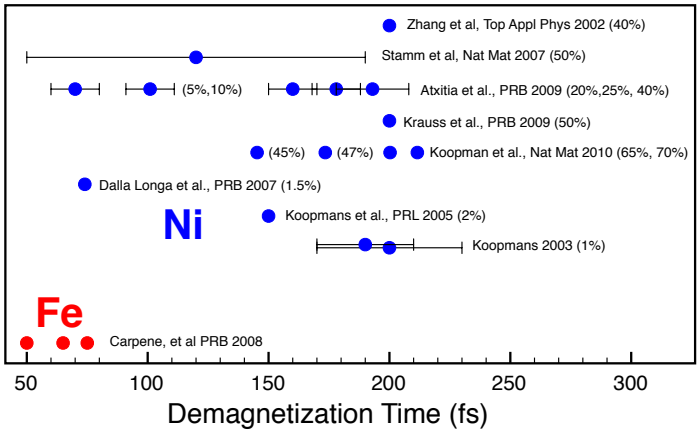

Figure 8.1: A non-exhaustive list of demagnetization times of Ni and Fe reported in literatures. The amplitude of demagnetization is indicated in the parentheses. No experiment has compared the demagnetization time of Fe and Ni in the same experimental conditions.

can affect the demagnetization time.

Another motivation to compare the demagnetization dynamics between Fe and Ni is from our observed dynamics in Permalloy and Permalloy–Cu (Chapter 7). Our measurement results indicate that Fe demagnetizes before Ni suggesting the Fe has a better spin-flip efficiency than Ni, and it is interesting to compare the trend of demagnetization time of Fe and Ni in their elemental forms.

In addition to the comparison between Fe and Ni dynamics, this chapter covers the study of fluence-dependent dynamics of Ni. The dynamical behavior as a function of fluence is in agreement with past results. I compare the observed results with two theoretical models based on a three-temperature model and the experimental results reported by Koopmans, et al [21]. All results benchmark our measurement technique with high-harmonic generation light source.

8.2 The Samples: Fe–Ni Binary Gratings

To compare elemental demagnetization dynamics between Fe and Ni simultaneously, our research team developed grating samples that consist of alternating stripes of pure Fe and pure Ni. (Figure 8.2). These samples are fabricated by Justin Shaw from NIST. The samples are made from 1 μm stripes of Ni with 4-μm center-to-center spacing. The second lithography step is used to pattern 1-μm wide Fe stripes in-between the previously fabricated Ni stripes, yielding alternating stripes of Fe and Ni with a centre-to-centre spacing of 2 μm. In both cases, the thicknesses of the individual Ni and Fe layers are 10 nm, and a 2-nm Ta seed layer was initially deposited for adhesion. After removal from the deposition chamber, these samples are quickly transferred to a vacuum storage chamber to minimize the surface oxidation and the corrosion of Fe.

With this sample geometry, the spacing between each element is 2 μm, which ensures no ferromagnetic coupling between Fe and Ni. However, the overall grating period is doubled from the work described earlier in Chapter 6-7, and the harmonic spacing measured on the CCD camera are twice as closer. As a result, the determination of the harmonic orders is more complicated. The photon energy of each harmonics is identified by fitting to the diffracted formula described in Chapter 5 (Figure 8.2). The harmonic energies can be labeled accurately up to the forth-order diffraction pattern. The diffraction patterns from Ni and Fe can be located. The results match the large measured asymmetries observed in the spectrum. We choose the magnetic asymmetries from the second-order diffraction patterns, which provide the best signal-to-noise ratio.

By pumping the grating with the same pump pulse, energy from a laser pulse is deposited equally on Fe and Ni. Since both elements absorb the same amount of light at 780 nm (42% for Fe and 40% for Ni calculated from the website in [179]), the same amount of hot electrons are created in each element to initiate the demagnetization dynamics.

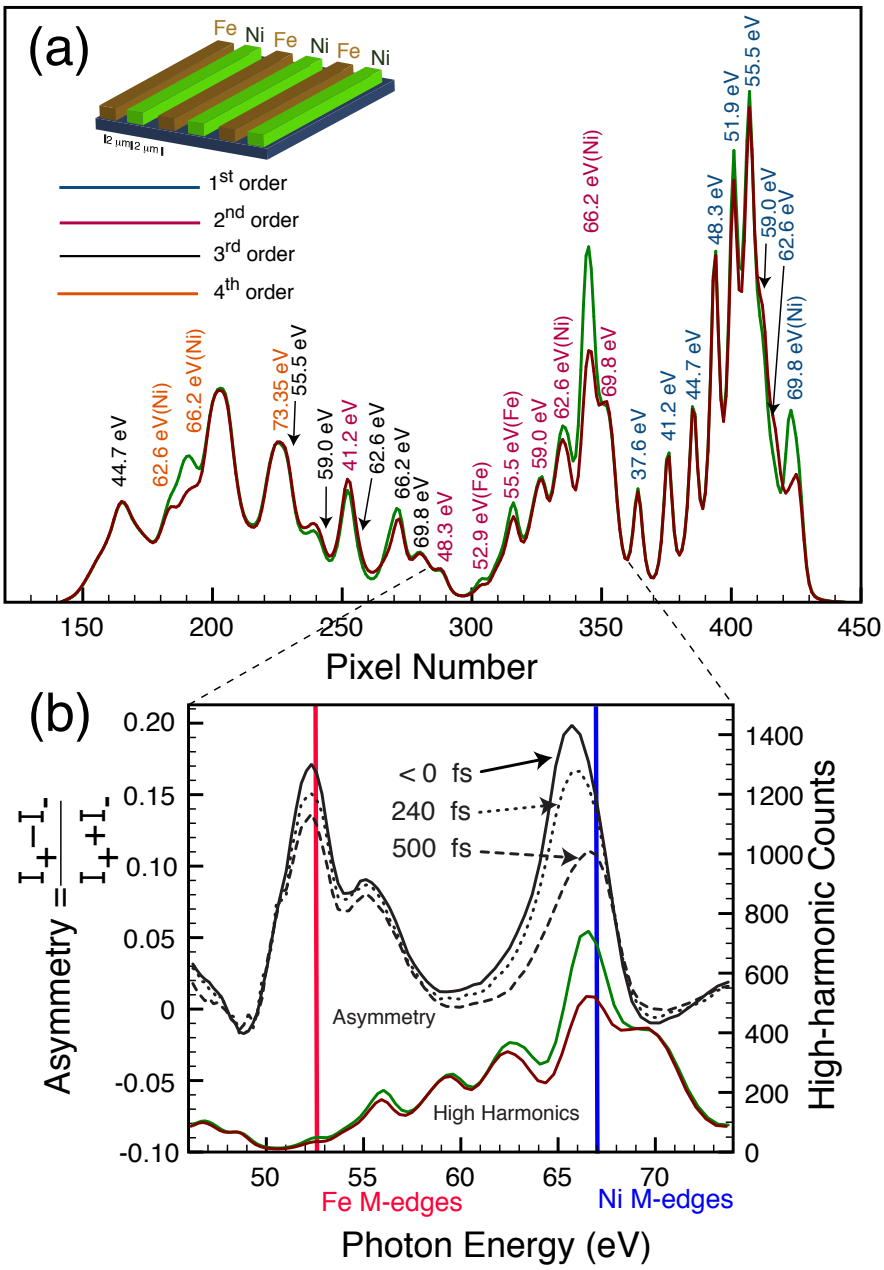

Figure 8.2: (a) Diffraction pattern from a Fe–Ni binary grating. The spectra of high harmonics from the two signs of magnetization are shown in green and brown. The energies of harmonics up to the forth order are labeled with their photon energy and dedicated Fe or Ni absorption M-edges. (b) A calibrated spectrum (green and brown) and the corresponding asymmetry (black). The asymmetry is quenched (dashed and dotted lines) following the demagnetization by a laser pulse.

(a)A medium scan: up to 3 ps (Figure 8.3, top)

Elements and Photon Energy	A	τ_M (fs)	τ_R (ps)
Ni (66.2 eV)	0.45 ± 0.01	157 ± 9	9.0 ± 1.3
Fe (55.5 eV and 52.9 eV)	0.19 ± 0.01	98 ± 26	10.9 ± 7.4

(b) A short scan: up to 600 fs (Figure 8.3, bottom)
τ_R is set to infinite.

Elements and Photon Energy	A	τ_M (fs)
Ni (62.6 eV)	0.37 ± 0.01	122 ± 7
Fe (55.5 eV and 52.9 eV)	0.111 ± 0.0004	77 ± 16

Table 8.1: Curve-Fitting Results to the Demagnetization Dynamics of Ni and Fe from a Fe–Ni grating. The parameters are defined in Equation 8.1

8.3 Demagnetization Dynamics

Demagnetization dynamics are measured from the harmonics with the largest asymmetries near M-shell absorption edges of Fe and Ni. Both Fe and Ni demagnetize independently immediately after the laser excitation (Figure 8.3). The dynamics differ noticeably from pure Permalloy, which show the delay of dynamics between Fe and Ni (Chapter 7). Independent demagnetization is expected when no coupling exists each element. From exponential fits, the demagnetization time of Fe is less than that of Ni by 59 ± 28 fs (Table 8.1). The trend of the demagnetization times agrees with the response from Fe and Ni in Permalloys, where Fe demagnetizes before Ni. The large error bar results solely from the Fe dynamics, which have worse data quality than Ni, resulting from various sources: the lower amplitude of demagnetization, sample oxidation, and the stronger absorption at the Fe M-edges with respect to the Ni M-edges. To reduce down the error bar, the data from Fe has been averaged over two different harmonics (photon energies at $h\nu$ = 55.5 and 52.9 eV) as indicated in Table 8.1.

At the long time delay, the demagnetization quenching are different for Fe and Ni, which is a different behavior from that observed with Permalloys. Ni demagnetizes more than Fe by a factor of 2.5. The amount of demagnetization can be understood from the spin density of Fe comparing to Ni at equilibrium. Fe has a larger magnetic

moment per atom than Ni by about the factor of 3.5 [20]. Therefore, there are more spins to be flipped in optical-induced–spin-flip scatterings for Fe than Ni. Consequently, Fe demagnetizes by a smaller percentage than Ni given that each material absorbs the same number of photons from the same light pulse.

The measured demagnetization times can be confirmed by comparing the results from different diffraction orders. By repeating the analysis on the 1st and 4th order diffraction of the harmonics at photon energy of 66.2 eV, we found that the demagnetization times of Ni ($\tau_M^{1st} = 150 \pm 13$ fs, $\tau_M^{4th} = 149 \pm 10$ fs) are still in agreement with the second-order diffraction value ($\tau_M^{2nd} = 157 \pm 9$ fs from Table 8.1).

The measurements were repeated with short time scans (only up to 600 fs). The magnetization recovery becomes less critical comparing to the demagnetization part. Therefore, the magnetization recovery time, τ_R, can be set to infinity. The demagnetization time is slightly smaller comparing to when the magnetization recovery time is finite (157 vs 122 fs for Ni). The reduction in the demagnetization time is understandable from the constraint to put the magnetization-recovery time to infinite. The dynamics at short time scales clearly show that the dynamics of the two elements are independent from each other.

8.4 Fluence-Dependent Demagnetization Dynamics

8.4.1 Experimental Results

Ultrafast demagnetization dynamics depend critically on the pump fluence. To systematically study the dependence of the dynamical parameters on the pump fluence, we attenuate the pump-beam power and repeat the demagnetization measurements. The laser fluence is reduced from 2.4 to 0.3 mJ/cm^2 (Figure 8.4). The measurements are performed continuously to make sure that the laser conditions are equivalent for all scans. We choose difference time steps for the two lowest fluences by having more data

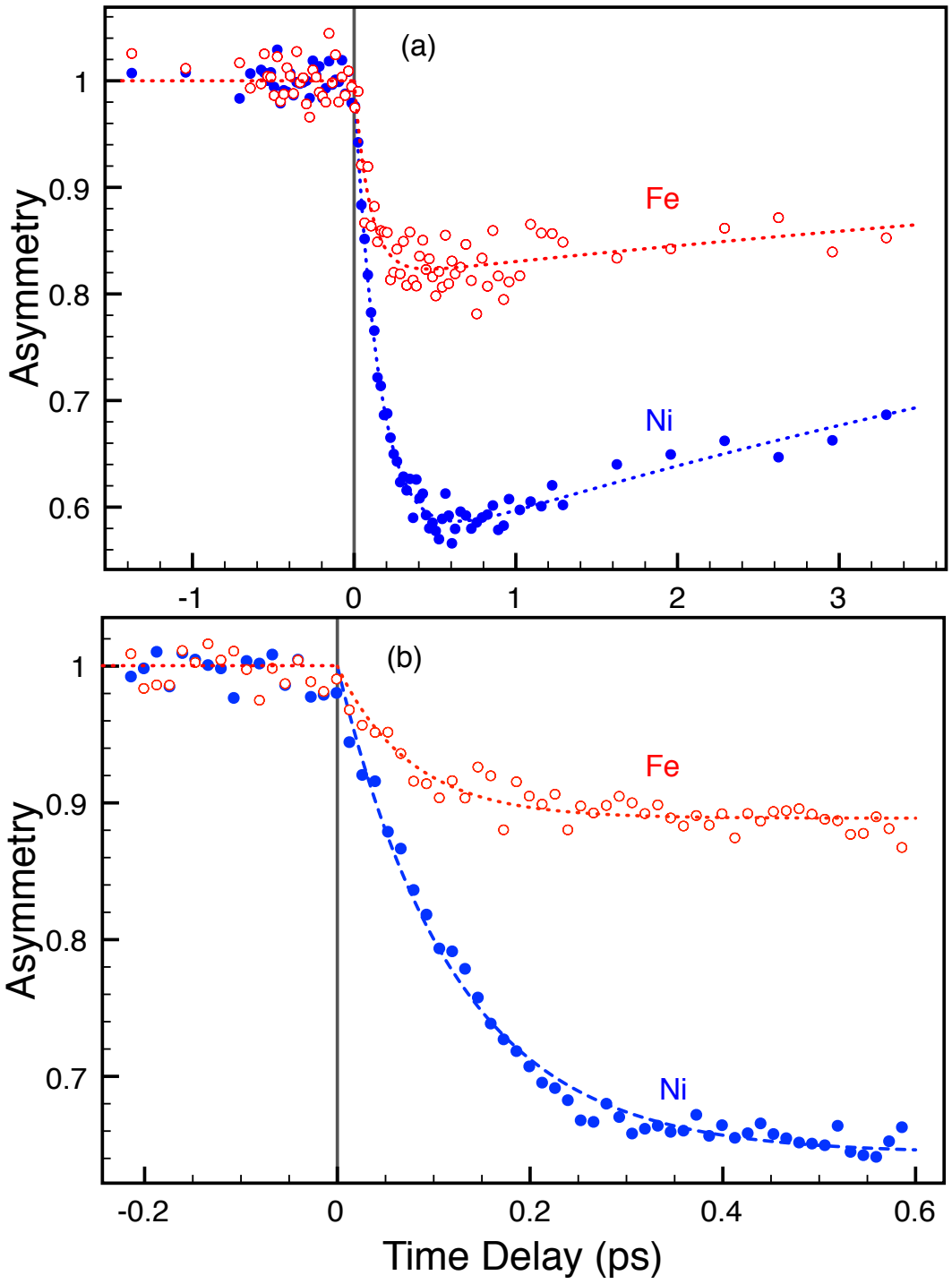

Figure 8.3: The comparison of laser-induced demagnetization dynamics between Fe (photon energies at 55.5 and 52.9 eV) and Ni (photon energy at 66.2 eV) in Fe–Ni grating for the time delay up to (a) 3 ps (top) and 600 ps (bottom). For both ranges, Fe demagnetizes faster than Ni and has less quenching.

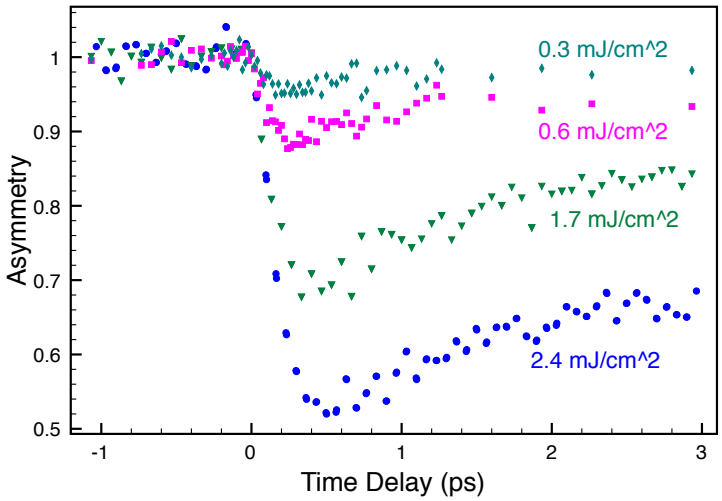

Figure 8.4: Fluence-dependent demagnetization dynamics of Ni in Fe–Ni grating.

points at short delay times because the demagnetization time is expected to be faster at the lower fluence.

The asymmetry is clearly quenched by a larger amount at higher fluences. Quantitatively, this trend can be understood by performing an exponential fit to the data. We choose the phenomenological equation:

$$f(t) = 1 - A(1 - e^{-\frac{t}{\tau_M}})e^{-\frac{t}{\tau_R}} \tag{8.1}$$

where A is demagnetization amplitude, τ_M is the demagnetization time, and τ_R is the magnetization-recovery time. The demagnetization amplitude shows a linear trend in fluence (Figure 8.5a). The error bars of the fit, however, increase at the low fluences as the demagnetization approaches the noise level of 3.5%. By performing a linear fit to the fluence (J) in mJ/cm^2 and demagnetization amplitude (A), we get the function $A = (0.21 \pm 0.04)J + (0.01 \pm 0.05)$. The relation is reasonable because the function extrapolates to zero at the zero fluence. Since the demagnetization amplitude depends linearly on fluence, the fluence value can be mapped to demagnetization amplitude. By presenting the data with the amplitude instead of fluence, the measurement results will be more general, and we can compare the results between different measurements. To

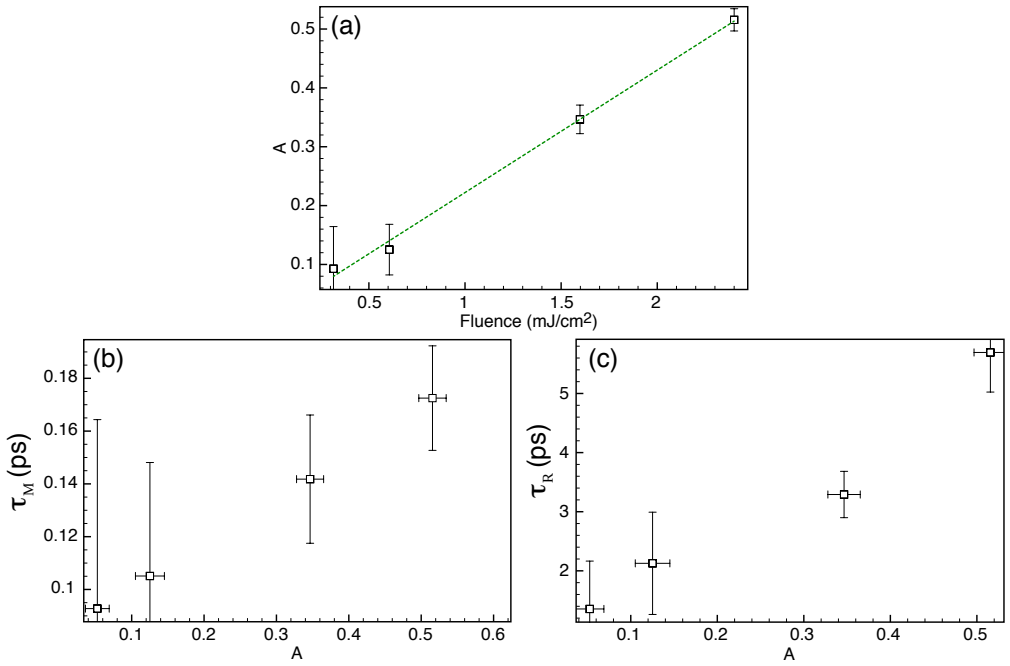

Figure 8.5: (a) Demagnetization amplitude (A), (b) demagnetization time (τ_M), and (c) magnetization recovery time (τ_R) describing fluence-dependent demagnetization dynamics (Figure 8.4) in a Ni–Fe grating.

show that fluence information is not comparable between different published results, I use Reference [148] and [21] as an example. Both papers report the demagnetization dynamics of Ni with about the same amount of quenching (40%). However, the fluences reported are an order-of-magnitude different, i.e. 50 mJ/cm^2 in Reference [148] and 2.2 mJ/cm^2 in Reference [21].

The magnetization recovery time (τ_R) in the order of a few picoseconds is an increasing function of the demagnetization amplitude. In the same manner, the demagnetization time (τ_M) is also an increasing function of the demagnetization amplitude or fluence varying from 80 to 170 fs, which is the same trend given by past results [21, 180]. By performing a linear extrapolation down the the zero demagnetization amplitude, the data give the minimum demagnetization time of 78.4 ± 9 fs, which agrees with the calculation in Reference [21] and the experimental results at low fluence limit [181]. In the next section, I will reproduce this relation between demagnetization time (τ_M) and amplitude (A) using a three-temperature-model calculation.

8.4.2 Three-Temperature-Model Simulation

Some properties of the observed fluence-dependent demagnetization dynamics can be reconstructed by use of three-temperature model (Chapter 4). Three-temperature model describes the heat transfer between three systems, i.e. electrons, lattice and spins, by assigning a temperature for each system (T_e, T_l, T_s). The model does not include any microscopic scattering physics, describing a more fundamental picture of demagnetization dynamics, but only through thermodynamic consideration. This formalism is the first approach to describe the temperature dynamics for ultrafast demagnetization [9], to consider the precession dynamics induced by a laser pulse [182], and recently to predict two regimes of demagnetization dynamics by incorporating the model with the microscopic Elliot-Yafet scattering [21].

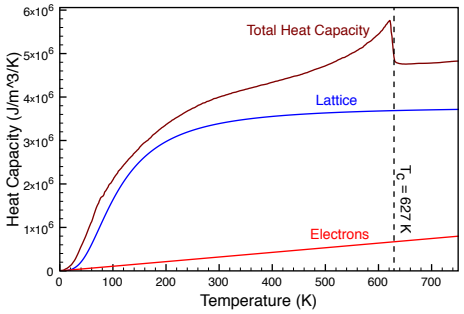

Figure 8.6: Heat capacities of Nickel composing of three contributions: electron (red), lattice (blue) and spins. Electron heat capacity is linear in temperature from the free-electron approximation (Equation 8.4). Lattice heat capacity is estimated from Debye's theory (Equation 8.5). The contribution from the spin system can be seen from an abrupt reduction in total heat capacity at Curie temperature. Data from [20]

Three-temperature model can be written as

$$\begin{aligned} C_e(T_e)\frac{\partial T_e}{\partial t} &= G_{el}(T_l - T_e) + G_{es}(T_s - T_e) + P(\mathbf{r}, t) \\ C_l(T_l)\frac{\partial T_l}{\partial t} &= G_{el}(T_e - T_l) + G_{sl}(T_s - T_l) - \kappa\nabla^2 T_l(\mathbf{r}, t) \\ C_s(T_s)\frac{\partial T_s}{\partial t} &= G_{es}(T_e - T_s) + G_{sl}(T_l - T_s), \end{aligned} \tag{8.2}$$

where C_e, C_l and C_s are heat capacities of electrons, lattice and spins, respectively, κ is thermal conductivity, $P(t)$ is a laser heating function. The coupling constants, G_{el}, G_{es}, and G_{sl}, are introduced to the model as empirical parameters. In this simulation, some assumptions are needed for these parameters.

8.4.2.1 Heat Capacities

Heat capacity of magnetic material is composed of the heat capacities from electron, lattice and spins (Figure 8.6 for Nickel),

$$C = C_e + C_l + C_s. \tag{8.3}$$

Specifically, the contribution from spins is obvious from an abrupt drop of the heat capacity at the Curie point of nickel ($T_c = 628K$) (Figure 8.6).

The electron heat capacity is linear in temperature:

$$C_e = C_{e0} T e, \tag{8.4}$$

where the heat capacity constant C_{e0} is 6000 $\mathrm{Jm^{-3}K^{-2}}$ for Co [182], 1064 $\mathrm{Jm^{-3}K^{-2}}$ for Ni [9] and 750 $\mathrm{Jm^{-3}K^{-2}}$ for Pt. The linearity of the electron heat capacity comes from a free-electron approximation [110, 183].

The heat capacity of the lattice sub-system can be described by Debye's theory [110, 183]:

$$C_l = 9 N_A k (\frac{T}{T_D})^3 \int_0^{\frac{T_D}{T}} \frac{x^4 e^x}{(e^x - 1)^2} \mathrm{d}x \tag{8.5}$$

where N_A is Avogadro's number, T_D is the Debye temperature (420 K for Fe, 385 K for Co and 375 K for Ni [110]), and k is the Boltzmann constant (Figure 8.6).

Finally, the heat capacity of the spin system is estimated by subtracting electron and lattice heat capacities from the total heat capacity (Equation 8.3).

8.4.2.2 Coupling Constants

The constants G_{el}, G_{es}, G_{sl} are empirical parameters for coupling between electron, lattice and spin sub-systems together. These parameters are material-specific and do not depend on experimental conditions such as pump fluence or pump-probe laser wavelength [184, 185]. The coupling constants are free parameters to optimize to the experimental data.

8.4.2.3 Laser-Heating Term

I assume that the pulse profile has a Gaussian shape in time and is exponentially-decaying through the sample thickness because of the sample absorption [184]:

$$P(t) = 0.94 \frac{1 - R - T}{\tau_p \delta} J \exp(-\frac{x}{\delta} - 2.77(\frac{t}{\tau_p})^2), \tag{8.6}$$

where R is sample reflectivity, T is sample transmission, τ_p is pulse duration, δ is penetration depth, x is the probe thickness inside the sample and J is the laser fluence. The reflectivity, transmission and penetration data of various materials can be found from Reference [179, 186]. In this simulation, I choose the parameters as the following: $T = 0.38, R = 0.22, \tau_p = 30$ fs, $\delta = 14$ nm for Ni interaction with 780 nm light. The probe thickness is set to 9 nm corresponding to the attenuation of high-harmonics near Ni M-edges from an x-ray database [13].

8.4.2.4 Heat Transportation Term

The term $\kappa\nabla^2 T_l$ describes heat transportation via phonons through substrate or environment. However, phonon heat transport is usually on a nanosecond time scale, which is too slow to consider in this simulation [58].

8.4.3 The Comparision between Experiment and Simulation Results

After applying all of the information above, I can initially calculate the temperatures of electrons, lattice and spins (Figure 8.7). The electron temperature is quickly elevated because of the laser pulse. Then, electrons cool down by thermalizing with the lattice and spins. From the value of coupling constants used in this simulation, spins are more efficient for the energy transfer than lattice. As a result, spin temperature is raised quickly comparing to lattice.

To relate temperatures to magnetization, I map the spin temperature to magnetization with a spontaneous magnetization curve calculated by Weiss's model (Appendix 1). Then, the simulation can be adjusted to the experimental data by optimizing the coupling constants (G_{es}, G_{el}) to experimental data. Here I use a nonliner curve-fitting routine (`nonlinfit` in Matlab) to search for the best coupling constants. In addition, the pump fluence is set as a free parameter.

From the fitting results, I found the spin-lattice (G_{sl}) coupling constant is not

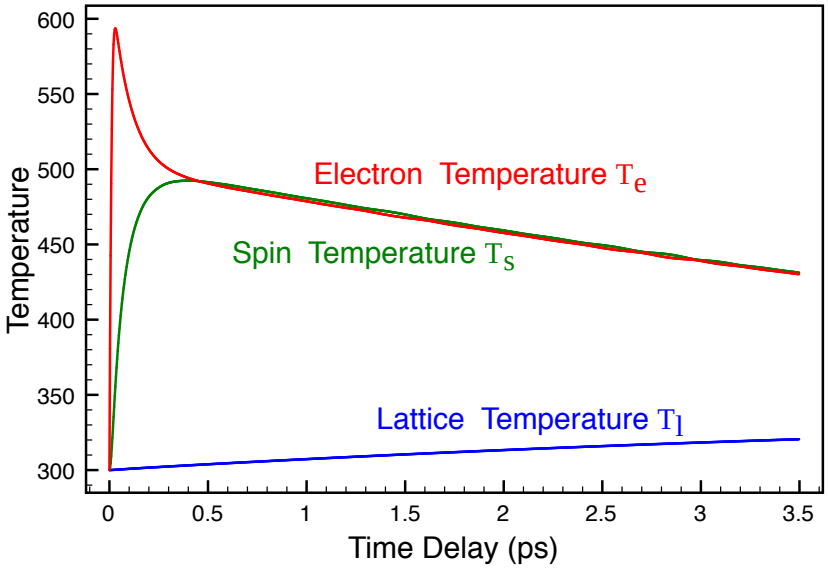

Figure 8.7: Temperatures of electron, lattice and spin in nickel after an excitation by a 2.25 mJ/cm^2 pump pulse. The demagnetization dynamics are a consequence from the temperature rise of the spin system.

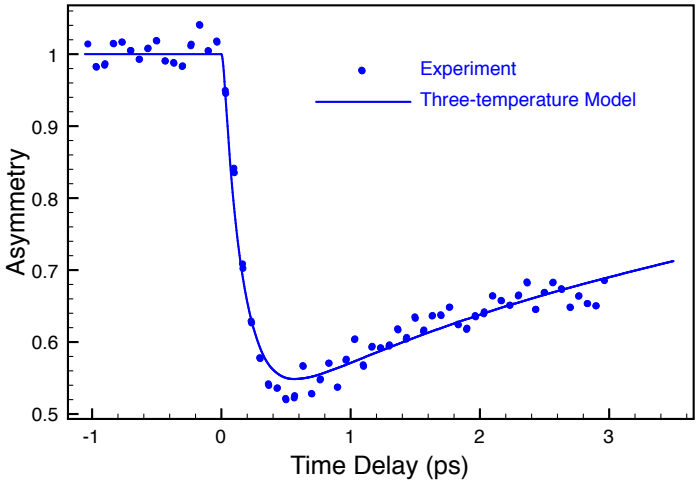

Figure 8.8: The best optimized simulation result to fit the demagnetization dynamics data. The best fit coupling parameters are $G_{el} = (0.93 \pm 0.13) \times 10^{16}$ Wm^{-3}K^{-1}, $G_{es} = (27.0 \pm 2.5) \times 10^{18}$ Wm^{-3}K^{-1}, $G_{sl} = 3 \times 10^{16}$ W m^{-3} K^{-1} (fixed), and laser fluence $(J) = 1.61 \pm 0.02$ mJ/cm^2. The measured pomp fluence is 2.4 mJ/cm^2.

orthogonal to the electron-lattice (G_{el}) constant, i.e. both parameters cannot fit simultaneously to receive good error bounds of both parameters, which control the magnetization recovery parameter (τ_R). One of them has to be determined as a constant. On the other hand, electron-spin coupling constants (G_{es}) and pump fluence (J) are orthogonal because the former controls the demagnetization time (τ_M), and the latter determines the demagnetization amplitude (A).

The best fit coupling parameters are $G_{el} = (0.93 \pm 0.13) \times 10^{16}$ $\mathrm{Wm^{-3}K^{-1}}$, $G_{es} = (27.0 \pm 2.5) \times 10^{18}$ $\mathrm{Wm^{-3}K^{-1}}$, and laser fluence is 1.61 ± 0.02 $\mathrm{mJ/cm^2}$. I set the spin-lattice coupling G_{sl} to $3 \times 10^{16} Wm^{-3}K^{-1}$ according to Beaurepaire et al [9]. Among these coupling parameters, spin-lattice coupling constant (G_{sl}) is the smallest since the spin-lattice scatting is the least efficient relaxation channel [11].

With the same set of the coupling constants, I compare the calculated demagnetization dynamics with the experimental data from Ni–Fe grating described earlier in this chapter (Figure 8.8) . The simulated demagnetization dynamics are in reasonably good agreement with the trend of the measurements. This agreement is not too surprising because there are three free parameters to adjust to the experimental data, which are the same as the three degrees of freedom to the demagnetization dynamcics (τ_M, τ_R, A).

After calculating the appropriate values of coupling parameters, I would like to calculate the dynamics as a function of pump fluences. I use the same set of coupling constants because they are independent of pump fluence [184]. The amplitude of the demagnetization (A) and the demagnetization times (τ_M) are calculated as functions of fluence from 1-4 mJ/cm^2.

The simulation results are compared with the experimental data. I choose the experimental data from four independent sources: our data from Ni–Fe grating (Section 3 and Section 4.1), our data from Ni grating, and the literature data by Koopmans et al[21]. Moreover, this calculation matches with the theoretical result from Koopmans

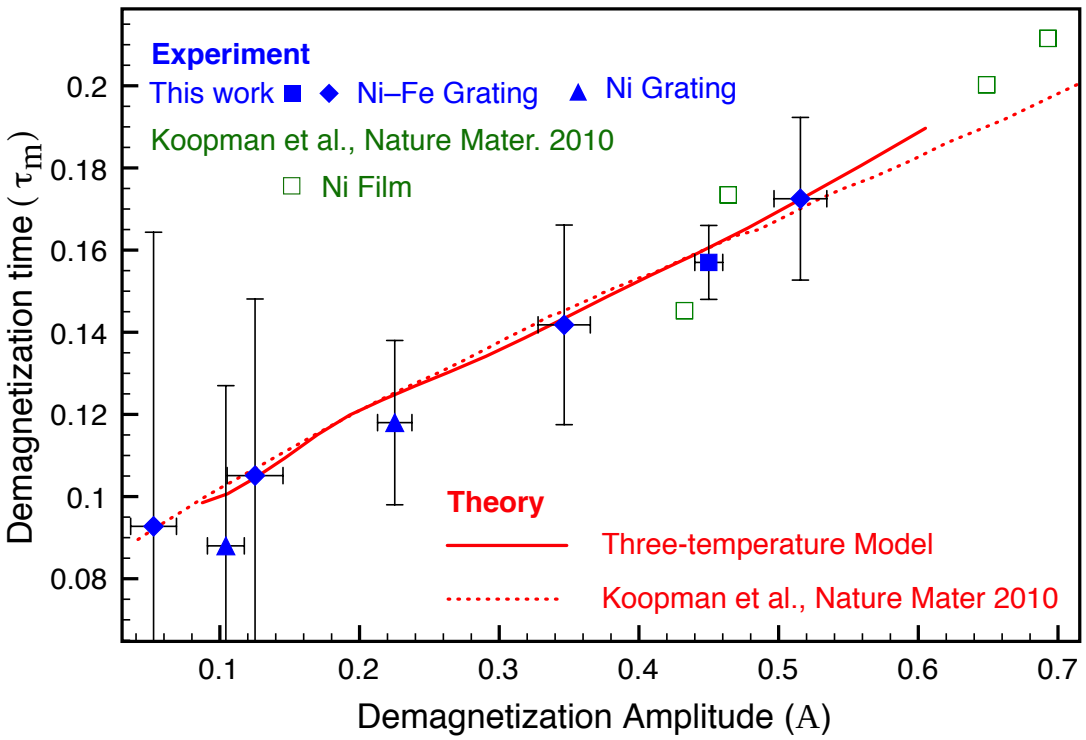

Figure 8.9: Demagnetization time (τ_M) as a function of demagnetization amplitude (A) from two theoretical and three experimental results. The experimental data are from two different samples, Ni–Fe grating (blue square and diamond) and Ni grating (blue triangles), and a literature result from Ni thin film (green squares) measured with visible L-MOKE technique [21]. From the same reference, I extract the theoretical prediction described by Elliot-Yafet mechanism (red dashed line) to compare with three-temperature model calculation presented here (red line).

et al. although the three-temperature model simulation shown here is only based on thermodynamic considerations. The agreement between the two independent calculations is due to the close relationship between the two formalisms. Koopmans et al. treated electron-lattice relaxation and dynamics in the same way as presented here by using an empirical coupling constant (G_{el}). One of the major differences is the spin relaxation part. The authors of Reference **??** employed the microscopic Elliot-Yafet mechanism to cause the spin-flip scattering and conserve angular momentum during the demagnetization. In contrast, I simplify the analysis by introducing the spin-lattice and spin-electron coupling constants.

The agreement between the four independent data sets benchmarks all of our results from time-resolved demagnetization measurements in three ways. First, the data confirm our high-harmonic identification technique at Ni M-edges from the diffraction patterns containing both Fe and Ni (Figure 8.2), which is the same technique used to distinguish between Ni and Fe in Permalloy. Second, the agreement with the data in the literature proves that the gratings do not interfere with the ultrafast time dynamics, and it is legitimate to use gratings as magnetic samples. Finally, we have a benchmark for our measurement technique with the well-established MOKE technique in visible wavelength. The results are in a good agreement despite the difference in the probe-wavelength of light (60 eV vs 3 eV), electronic states involved (3p core levels vs 3d valence levels), and experimental geometry (T-MOKE vs L-MOKE).

8.5 Conclusions

In conclusion, in the first half of this chapter, I compare the demagnetization dynamics between Fe and Ni from Ni–Fe gratings. The result confirms our experimental finding in Permalloy and Permalloy–Cu that the demagnetization dynamics of Ni are delayed with respect to that of Fe. We observe that with identical optical excitations on both elements, Fe demagnetizes faster than Ni. The results suggests that Fe is

intrinsically more efficient for hot-electron-driven–spin-flip processes. Moreover, Fe and Ni demagnetize independently, in contrast to the delay behavior found in Permalloy and Permalloy–Cu because of the lack of exchange interaction to lock Fe and Ni together.

In the second half of this chapter, I present the fluence-dependent demagnetization dynamics for Ni–Fe gratings. The demagnetization times agree with the simulation results based on three-temperature model and a more advanced three-temperature model given by Koopmans et al. [21]. In additional, experimental results from different sources, i.e. Ni grating and Ni thin film from Reference [21] measured with optical laser pulse, also follow the prediction by our model. These results provide an important foundation for future magnetization dynamics studies with extreme-ultraviolet light from high-harmonic generation.

Chapter 9

Conclusions and Magnetic Imaging

9.1 Conclusions

In this thesis, I report the first combined application of two well-established fields: high-harmonic generation (Chapter 2) and extreme-ultraviolet magneto-optics (Chapter 3) to explore one of the most exciting problems in magnetism: the laser-induced demagnetization dynamics (Chapter 4). In previous chapters,

- I discuss the method and experimental apparatus for measuring the element-selective magnetization dynamics with extreme-ultraviolet high harmonics (Chapter 5).

- By use of the transverse magneto-optical Kerr effect, magnetic asymmetries in reflectivity up to 30% are detected near M-shell absorption edges of Fe and Ni in Permalloy (Chapter 6). With this large contrast, our group measured hysteresis loops for Fe and Ni in Permalloy, which are identical because of the strong ferromagnetic exchange coupling. In addition, we show that the magnetic asymmetry decays exponentially with the metallic over-layer thickness in a few nanometers corresponding to the penetration of harmonics into palladium. This technique demonstrates the near-surface sensitivity of our probe light.

- We took advantage of the ultrafast time resolution and element-selectivity to

study laser-induced demagnetization dynamics in Permalloy, Permalloy–Cu (Chapter 7), and Fe–Ni binary grating (Chapter 8).

- We report that the asymmetry dynamics of Fe and Ni are delayed relative to each other (Chapter 7). The amount of the delay time is significantly enhanced when the exchange coupling is reduced by diluting copper into Permalloy. Exponential fits to the data reveal that demagnetization of Ni is delayed with respect to Fe by ∼10 fs in Permalloy and by ∼60 fs in Permalloy-Copper. We confirm that the observed delays do not originate from (1) phase segregation in our alloy samples, (2) hot-electron screening, and (3) experimental errors such as time-zero determination.

- We describe the delayed magnetization dynamics by a simple model that incorporates a finite exchange-time factor into the magnetization rate equations (Chapter 7). The data analysis indicates that Fe demagnetizes first after the interval of the laser pulse while Ni remains unaffected until after the exchange time. Afterwards, the magnetization of Ni is dragged down by Fe because of the exchange coupling.

- We compare the demagnetization dynamics between Fe and Ni with identical experimental conditions (Chapter 8) in Fe–Ni grating. Fe still demagnetizes faster than Ni in qualitative agreement with our observations for Permalloy and Permalloy–Cu.

- We measured fluence-dependent demagnetization dynamics. The demagnetization times agree with the simulation results based on three-temperature model. In addition, the experimental results are compared with both theoretical and experimental magneto-optical Kerr effect in visible [21]. The agreement benchmarks our technique for probing ultrafast demagnetization dynamics with a

high-harmonic generation light source.

9.2 Magnetic Imaging

From the results presented earlier, we took advantage of two features of high-harmonic generation and M-edge T-MOKE: element-selectivity and ultrafast time-resolution. However, our studies do not take advantage of the potential for high spatial resolution imaging. That is a consequence of the short wavelength of high harmonics. As mentioned in the introduction (Chapter 1), future studies will require the incorporation of nanomagnetic imaging with dynamical studies.

Beforehand, magnetic imaging with high-harmonic generation light source must be demonstrated. Previously, our research group has shown that high harmonics are capable of lensless microscopy by the coherent diffractive imaging technique [59, 187, 188]. We scattered high-harmonic beams from nanostructure samples and recorded the diffraction patterns in the far field. Since the phase information is lost during intensity measurements with light detectors (e.g. CCD), the phase must be retrieved by iterative algorithms [189, 190, 191, 192] or alternatively by encoding the phase into holograms [193, 194, 195, 188]. Both methods allow for a complete image reconstruction by a single Fourier transform. In the past, a single high harmonic with photon energy near 42 eV from argon [59] or near 90 eV from helium [196] must be selected by multilayer-mirror monochrometers. Multiple-wavelength diffractive imaging bypasses this requirement and improves the photon flux [61, 197]. Moreover, single-shot experiments were recently demonstrated [198, 60]. Although, much attention has been brought to the field, the imaging of magnetic materials with high-harmonic generation light source has not yet been demonstrated.

In the synchrotron community, however, magnetic diffractive imaging is still an active field because of two reasons; first, circular polarized x-rays are common in synchrotrons through helical undulaters [199] or bending magnets [96]. With the accessibil-

ity to circular-polarized radiation, the contrast for diffractive imaging in a transmission geometry is provided by x-ray–magnetic-circular dichroism (Chapter 3). Second, the contrast level provided by x-ray–magnetic-circular dichroism is large at L-shell absorption edges at soft x-ray wavelengths that are available in many synchrotrons worldwide. The reported contrast levels are up to 50% for iron, cobalt and nickel [200]. X-ray microscopes have been built based upon photo-emission electron spectroscopy [201] or zone-plate microscopy [200]. In addition, lensless holography experiments have been demonstrated [202, 203].

From these existing ideas, magnetic microscopy with a table high-harmonic light source can be achieved in three ways. First, similar the all of the results described in this thesis, the transverse magneto-optical Kerr effect can be employed as a contrast mechanism. The experiment must be conducted in reflection geometry, in contrast to the transmission geometry used in all of the past microscopy efforts with the high-harmonic light source. Lensless imaging in a reflection geometry is possible as recently demonstrated in a synchrotron [204].

Second, an alternative approach is to first convert the polarization of high harmonics to circular polarization. Unfortunately, there is not an efficient 'quarter waveplate' at extreme ultraviolet wavelength because of the strong absorption of any materials. One idea is to induce some degree of ellipticity be use of the Faraday effect (Chapter 3) as demonstrated with soft x-rays at L-edges [205]. However, at M-edges, the applications of this conversion technique are impractical since the light transmission and the Faraday effects are significantly weaker. From the calculation presented in Chapter 3, to convert a linearly polarized beam to a perfect circular-polarization at 55 eV, ones need an Fe film that is 1125 nm thick[1] . At this thickness, no harmonic can transmit through any sample (the transmission is in the order of 10^{-35}!). A more reasonable method to achieve circular polarization is by use of quadruple reflectors [99, 116] or

[1] From the calculated value of about 2° of ellipticity induced per 50 nm Fe film at 55 eV.

multilayer optics [206].

Finally, magnetic imaging in a transmission geometry with linearly polarized light is possible by use of different physics from the magneto-optical effects. Recently, magnetic imaging is demonstrated by taking advantage of magnetic scattering with linearly polarized synchrotron radiation [207, 208]. The experiments employ the well-known technique of small-angle magnetic scattering [209, 210, 211, 212, 213, 214, 215, 216, 217], used in the past to estimate the size and correlation of magnetic domains from the angular distributions of the scattering patterns. In the past, the magnetic scattering experiments were only limited in synchrotrons at L-edges, but recently experiments were demonstrated in free-electron laser [218] and high-harmonic generation [219] at M-edges. This approach is the most efficient and promising among the three proposed methods.

Another challenge to overcome for the future magnetic-imaging experiment is to reduce the wavelength of high-harmonic generation. For high harmonics at extreme ultraviolet, the diffraction limit only allows for the spatial resolution that suits for imaging magnetic nanostructures up to the areal density of $\sim$1 Tbits/in^2. However, in 2020, the industry expects the areal density to be in 10 Tbits/in^2 (Chapter 1). To be able to image such small nanostructures, harmonics must be in soft x-rays at L-shell absorption edges. To demonstrate this ability, our group recently reported high-harmonic generation at soft x-ray wavelengths by driving the conversion with an intense mid-infrared laser. The long wavelength driving laser extends the cut-off of high-harmonic generation (Chapter 2) [84, 83, 75]. The generated photons cover the L-shell absorption edges of Fe, Co and Ni [64]. However, improvement of the soft x-ray flux for actual applications is still a great engineering challenge.

But if all off these barriers can be overcome in the near future, we may see

the combination of ultrafast time resolution, nanoscale spatial resolution, and element selectivity in a magnetic experiment with a tabletop light source.

Bibliography

[1] J. M. D. Coey. Magnetism and Magnetic Materials. Cambridge University Press, Cambridge, United Kingdom, 2010.

[2] S. M. Thompson. The discovery, development and future of GMR: The Nobel Prize 2007. Journal of Physics D: Applied Physics, 41(9):093001, 2008.

[3] A. Moser, K. Takano, D. T. Margulies, M. Albrecht, Y. Sonobe, Y. Ikeda, S. H. Sun, and E. E. Fullerton. Magnetic recording: advancing into the future. Journal of Physics D: Applied Physics, 35(19):R157, 2002.

[4] Hitachi Global Storage Technologies. Patterned magnetic media, https://www1.hitachigst.com/hdd/research/storage/pm/index.html.

[5] L. Pan and D. B. Bogy. Heat-assisted magnetic recording. Nature Photonics, 3(4):186, 2009.

[6] Wikipedia. Earth's magnetic field, http://en.wikipedia.org/wiki/earth's_magnetic_field, 2011.

[7] Hitachi Global Storage Technologies. Ultrastar 7k3000 http://www.hitachigst.com/internal-drives/enterprise/ultrastar/ultrastar-7k3000.

[8] Wikipedia. Transformer http://en.wikipedia.org/wiki/transformer, 2011.

[9] E. Beaurepaire, J. C. Merle, A. Daunois, and J. Y. Bigot. Ultrafast spin dynamics in ferromagnetic nickel. Physical Review Letters, 76(22):4250, 1996.

[10] J. Y. Bigot, M. Vomir, and E. Beaurepaire. Coherent ultrafast magnetism induced by femtosecond laser pulses. Nature Physics, 5(7):515, 2009.

[11] J. Stöhr and H. C. Siegmann. Magnetism: From Fundamentals to Nanoscale Dynamics (Springer Series in Solid-State Sciences). Springer, Berlin, Germany, 2006.

[12] H. Hochst, D. Rioux, D. Zhao, and D. L. Huber. Magnetic linear dichroism effects in reflection spectroscopy: A case study at the Fe M_2,M_3 edge. Journal of Applied Physics, 81(11):7584, 1997.

[13] E. Gullikson. X-ray interactions with matter, http://henke.lbl.gov/optical_constants/.

[14] J. Mathon and A. Umerski. Physics of Low Dimensional Systems. Springer, 2001.

[15] Maarten van Kampen. Ultrafast spin dynamics in ferromagnetic metals. pages 1–147, May 2003.

[16] C. Stamm, N. Pontius, T. Kachel, M. Wietstruk, and H. A. Dürr. Femtosecond x-ray absorption spectroscopy of spin and orbital angular momentum in photoexcited ni films during ultrafast demagnetization. Physical Review B, 81(10):104425, 2010.

[17] F. Dalla Longa, J. T. Kohlhepp, W. J. M. de Jonge, and B. Koopmans. Influence of photon angular momentum on ultrafast demagnetization in nickel. Physical Review B, 75(22):224431, 2007.

[18] Newport Corporation. Google sketup, 3D collections.

[19] Andor Technology. X-ray cameras, http://www.andor.com, August 2011.

[20] R. M. Bozorth. Ferromagnetism. Wiley-IEEE Press, Hoboken, NJ, 1993.

[21] B. Koopmans, G. Malinowski, F. Dalla Longa, D. Steiauf, M. Faehnle, T. Roth, M. Cinchetti, and M. Aeschlimann. Explaining the paradoxical diversity of ultrafast laser-induced demagnetization. Nature Materials, 9(3):259, 2010.

[22] M. G. Siegler. Eric Schmidt: Every 2 days we create as much information as we did up to 2003, http://techcrunch.com/2010/08/04/schmidt-data/, 2010.

[23] Hitachi Global Storage Technologies. HDD technology overview charts, https://www1.hitachigst.com/hdd/technolo/overview/storagetechchart.html, 2010.

[24] G. E. Moore. Cramming more components onto integrated circuits. Electronics, 38(8):114, 1965.

[25] M. H. Kryder and R. W. Gustafson. High-density perpendicular recording–advances, issues, and extensibility. Journal of Magnetism and Magnetic Materials, 287:449, 2005.

[26] S. H. Charap, P. L. Lu, and Y. He. Thermal stability of recorded information at high densities. IEEE Transactions on Magnetics, 33(1):978, 1997.

[27] D. Weller and A. Moser. Thermal effect limits in ultrahigh-density magnetic recording. IEEE Transactions on Magnetics, 35(6):4423, 1999.

[28] S. Iwasaki and Y. Nakamura. The magnetic field distribution of a perpendicular recording head. IEEE Transactions on Magnetics, 14(5):436, 1978.

[29] S. I. Iwasaki. Perpendicular magnetic recording focused on the origin and its significance. IEEE Transactions on Magnetics, 38(4):1609, 2002.

[30] S. N. Piramanayagam. Perpendicular recording media for hard disk drives. Journal of Applied Physics, 102(1):011301, 2007.

[31] H. Saga, H. Nemoto, H. Sukeda, and M. Takahashi. New recording method combining thermo-magnetic writing and flux detection. Japanese Journal of Applied Physics, 38(3B):1839, 1999.

[32] J. J. M. Ruigrok, R. Coehoorn, S. R. Cumpson, and H. W. Kesteren. Disk recording beyond 100 Gb/in^2: Hybrid recording? Journal of Applied Physics, 87(9):5398, 2000.

[33] T. W. McDaniel. Ultimate limits to thermally assisted magnetic recording. Journal of Physics: Condensed Matter, 17(7):R315, 2005.

[34] M. H. Kryder, E. C. Gage, T. W. McDaniel, W. A. Challener, R. E. Rottmayer, Ga. Ju, Y. T. Hsia, and M. F. Erden. Heat-assisted magnetic recording. Proceedings of the IEEE, 96(11):1810, 2008.

[35] A. Sakdinawat and D. Attwood. Nanoscale x-ray imaging. Nature Photonics, 4(12):840, 2010.

[36] G. Tallents, E. Wagenaars, and G. Pert. Lithography at EUV wavelengths. Nature Photonics, 4(12):809, 2010.

[37] J. Kirz, C. Jacobsen, and M. Howell. Soft x-ray microscopes and their biological applications. Quarterly Reviews of Biophysics, 28(1):33, 1995.

[38] C. Jacobsen. Soft x-ray microscopy. Trends in Cell Biology, 9(2):44–47, 1999.

[39] C. D. Stanciu, F. Hansteen, A. V. Kimel, A. Kirilyuk, A. Tsukamoto, A. Itoh, and Th. Rasing. All-optical magnetic recording with circularly polarized light. Physical Review Letters, 99(4):047601, 2007.

[40] M. Van Kampen, C. Jozsa, J. T. Kohlhepp, P. LeClair, L. Lagae, W. J. M. de Jonge, and B. Koopmans. All-optical probe of coherent spin waves. Physical Review Letters, 88(22):227201, 2002.

[41] C. Stamm, T. Kachel, N. Pontius, R. Mitzner, T. Quast, K. Holldack, S. Khan, C. Lupulescu, E. F. Aziz, M. Wietstruk, et al. Femtosecond modification of electron localization and transfer of angular momentum in nickel. Nature Materials, 6(10):740, 2007.

[42] E. Beaurepaire, G. M. Turner, S. M. Harrel, M. C. Beard, J. Y. Bigot, and C. A. Schmuttenmaer. Coherent terahertz emission from ferromagnetic films excited by femtosecond laser pulses. Applied Physics Letters, 84(18):3465, 2004.

[43] A. A. Zholents and M. S. Zolotorev. Femtosecond x-ray pulses of synchrotron radiation. Physical Review Letters, 76(6):912, 1996.

[44] R. W. Schoenlein, S. Chattopadhyay, H. H. W. Chong, T. E. Glover, P. A. Heimann, C. V. Shank, A. A. Zholents, and M. S. Zolotorev. Generation of femtosecond pulses of synchrotron radiation. Science, 287(5461):2237, 2000.

[45] S . Khan, K. Holldack, T. Kachel, R. Mitzner, and T. Quast. Femtosecond undulator radiation from sliced electron bunches. Physical Review Letters, 97(7):074801, 2006.

[46] D. A. G. Deacon, L. R. Elias, J. M. J. Madey, G. J. Ramian, H. A. Schwettman, and T. I. Smith. First operation of a free-electron laser. Physical Review Letters, 38(16):892, 1977.

[47] J. Andruszkow, B. Aune, V. Ayvazyan, N. Baboi, R. Bakker, V. Balakin, D. Barni, A. Bazhan, M. Bernard, A. Bosotti, J. C. Bourdon, et al. First observation of self-amplified spontaneous emission in a free-electron laser at 109 nm wavelength. Physical Review Letters, 85(18):3825, 2000.

[48] W. Ackermann, G. Asova, V. Ayvazyan, A. Azima, N. Baboi, J. Bähr, V. Balandin, B. Beutner, A. Brandt, A. Bolzmann, et al. Operation of a free electron laser from the extreme ultraviolet to the water window. Nature Photonics, 1, 2007.

[49] B. W. J. Mcneil and N. R. Thompson. X-ray free-electron lasers. Nature Photonics, 4(12):814, 2010.

[50] H. N. Chapman, A. Barty, M. J. Bogan, S. Boutet, M. Frank, S. P. Hau-Riege, S. Marchesini, B. W. Woods, S. Bajt, W. H. Benner, et al. Femtosecond diffractive imaging with a soft-x-ray free-electron laser. Nature Physics, 2(12):839, 2006.

[51] K. Nakajima. Towards a table-top free-electron laser. Nature Physics, 4(2):92, 2008.

[52] P. Emma, R. Akre, J. Arthur, R. Bionta, C. Bostedt, J. Bozek, A. Brachmann, P. Bucksbaum, R. Coffee, F.J. Decker, et al. First lasing and operation of an ångstrom-wavelength free-electron laser. Nature Photonics, 4(9):641, 2010.

[53] J. Itatani, J. Levesque, D. Zeidler, H. Niikura, H. Pépin, J. C. Kieffer, P. B. Corkum, and D. M. Villeneuve. Tomographic imaging of molecular orbitals. Nature, 432(7019):867, 2004.

[54] W. Li, X. Zhou, R. Lock, S. Patchkovskii, A. Stolow, H. C. Kapteyn, and M. M. Murnane. Time-resolved dynamics in N_2O_4 probed using high harmonic generation. Science, 322(5905):1207, 2008.

[55] E. Goulielmakis, Z. H. Loh, A. Wirth, R. Santra, N. Rohringer, V. S. Yakovlev, S. Zherebtsov, T. Pfeifer, A. M. Azzeer, M. F. Kling, et al. Real-time observation of valence electron motion. Nature, 466(7307):739, 2010.

[56] A. L. Cavalieri, N. Muller, T. Uphues, V. S. Yakovlev, A. Baltuška, B. Horvath, B. Schmidt, L. Blumel, R. Holzwarth, S. Hendel, et al. Attosecond spectroscopy in condensed matter. Nature, 449(7165):1029, 2007.

[57] T. Rohwer, S. Hellmann, M. Wiesenmayer, C. Sohrt, A. Stange, B. Slomski, A.Carr, Y. Liu, L. Miaja Avila, M. Kalläne, et al. Collapse of long-range charge order tracked by time-resolved photoemission at high momenta. Nature, 471(7339):490, 2011.

[58] M. E. Siemens, Q. Li, R. Yang, K. A. Nelson, E. H. Anderson, M. M Murnane, and H. C. Kapteyn. Quasi-ballistic thermal transport from nanoscale interfaces observed using ultrafast coherent soft x-ray beams. Nature Materials, 9(1):26, 2010.

[59] R. L. Sandberg, A. Paul, D. A. Raymondson, S. Haedrich, D. M. Gaudiosi, J. Holtsnider, R. I. Tobey, O. Cohen, M. M. Murnane, and H. C. Kapteyn. Lensless diffractive imaging using tabletop coherent high-harmonic soft-x-ray beams. Physical Review Letters, 99(9):098103, 2007.

[60] A. Ravasio, D. Gauthier, F. R. N. C. Maia, M. Billon, J.-P Caumes, D. Garzella, M. Geleoc, O. Gobert, J. F Hergott, A. M Pena, et al. Single-shot diffractive imaging with a table-top femtosecond soft x-ray laser-harmonics source. Physical Review Letters, 103(2):028104, 2009.

[61] B. Chen, R. A. Dilanian, S. Teichmann, Br. Abbey, A. G. Peele, G. J. Williams, P. Hannaford, L. Van Dao, H. M. Quiney, and K. A. Nugent. Multiple wavelength diffractive imaging. Physical Review A, 79(2):023809, 2009.

[62] R. Berlasso, C. Dallera, F. Borgatti, C. Vozzi, G. Sansone, S. Stagira, M. Nisoli, G. Ghiringhelli, P. Villoresi, L. Poletto, et al. High-order laser harmonics and synchrotron study of transition metals $M_{2,3}$ edges. Physical Review B, 73(11):115101, January 2006.

[63] C. La-O-Vorakiat, M. Siemens, M. M. Murnane, H. C. Kapteyn, S. Mathias, M. Aeschlimann, P. Grychtol, R. Adam, C. M. Schneider, J. M. Shaw, et al. Ultrafast demagnetization dynamics at the M edges of magnetic elements observed using a tabletop high-harmonic soft x-ray source. Physical Review Letters, 103(25):257402, 2009.

[64] T. Popmintchev, M. Chen, D. Popmintchev, S. Alisauskas, G. Andriukaitis, T. Balciunas, A. Pugzlys, A. Baltuska, M. M. Murnane, and H. C. Kapteyn. Bright coherent attosecond-to-zeptosecond kiloelectronvolt x-ray supercontinua. In CLEO:2011 - Laser Applications to Photonic Applications, page PDPC12. Optical Society of America, 2011.

[65] T. H. Maiman. Stimulated optical radiation in ruby. Nature, 187:493, 1960.

[66] P. A. Franken, A. E. Hill, C. W. Peters, and G. Weinreich. Generation of optical harmonics. Physical Review Letters, 7(4):118, 1961.

[67] J. A. Armstrong, N. Bloembergen, J. Ducuing, and P. S. Pershan. Interactions between light waves in a nonlinear dielectric. Physical Review, 127(6):1918, 1962.

[68] R. W. Boyd. Nonlinear Optics. Academic Press, Waltham, Massachusetts, third edition, 2008.

[69] M. M. Choy and R. L. Byer. Accurate second-order susceptibility measurements of visible and infrared nonlinear crystals. Physical Review B, 14(4):1693, 1976.

[70] T. Brabec and F. Krausz. Intense few-cycle laser fields: Frontiers of nonlinear optics. Reviews of Moden Physics, 72(2):545, 2000.

[71] M. Protopapas, C. H. Keitel, and P. L. Knight. Atomic physics with super-high intensity lasers. Reports on Progress in Physics, 60(4):389, 1997.

[72] H. C. Kapteyn, M. M. Murnane, and I. R. Christov. Extreme nonlinear optics: A coherent x rays from lasers. Physics Today, 58(3):39, 2005.

[73] T. Pfeifer, C. Spielmann, and G. Gerber. Femtosecond x-ray science. Reports on Progress in Physics, 69:443, 2006.

[74] H. Kapteyn, O. Cohen, I. Christov, and M. Murnane. Harnessing attosecond science in the quest for coherent x-rays. Science, 317(5839):775, 2007.

[75] T. Popmintchev, M. Chen, P. Arpin, M. M. Murnane, and H. C. Kapteyn. The attosecond nonlinear optics of bright coherent X-ray generation. Nature Photonics, 4(12):822, 2010.

[76] N. H. Burnett, H. A. Baldis, M. C. Richardson, and G. D. Enright. Harmonic generation in CO_2 laser target interaction. Applied Physics Letters, 31(3):172, 1977.

[77] M. Ferrat, A. L'Huillier, X. F. Li, L. A. Lompre, G. Mainfray, and C. Manus. Multiple-harmonic conversion of 1064-nm radiation in rare-gases. Journal of Physics B, 21(3):L31, 1988.

[78] A. Mcpherson, G. Gibson, H. Jara, U. Johann, T. S. Luk, I. A. Mcintyre, K. Boyer, and C. K. Rhodes. Studies of multiphoton production of vacuum ultraviolet-radiation in the rare-gases. Journal of the Optical Society of America B, 4(4):595, 1987.

[79] P. B. Corkum. Plasma perspective on strong-field multiphoton ionization. Physical Review Letters, 71(13):1994, 1993.

[80] M. V. Ammosov, N. B. Delone, and V. P. Krainov. Tunnel ionization of complex atoms and atomic ions by an alternating electromagnetic field. Soviet Physics - JETP, 64:1191, 1986.

[81] L. V. Keldysh. Ionization in the field of a strong electromagnetic wave. Soviet Physics - JETP, 20:1307, 1965.

[82] P. B. Corkum, N. H. Burnett, and F. Brunel. Above-threshold ionization in the long-wavelength limit. Phys. Rev. Lett., 62(11):1259–1262, Mar 1989.

[83] M. Chen, P. Arpin, T. Popmintchev, M. Gerrity, B. Zhang, M. Seaberg, D. Popmintchev, M. M. Murnane, and H. C. Kapteyn. Bright, coherent, ultrafast soft x-ray harmonics spanning the water window from a tabletop light source. Physical Review Letters, 105(17):173901, 2010.

[84] T. Popmintchev, M. Chen, A. Bahabad, M. Gerrity, P. Sidorenko, O. Cohen, I. P. Christov, M. M. Murnane, and H. C. Kapteyn. Phase matching of high harmonic generation in the soft and hard X-ray regions of the spectrum. Proceedings of the National Academy of Sciences, 106(26):10516, 2009.

[85] A. L. Cavalieri, E. Goulielmakis, B. Horvath, W. Helml, M. Schultze, M. Fieß, V. Pervak, L. Veisz, V. S. Yakovlev, M. Uiberacker, A. Apolonski, F. Krausz, and R. Kienberger. Intense 1.5-cycle near infrared laser waveforms and their use for the generation of ultra-broadband soft-x-ray harmonic continua. New Journal of Physics, 9:242, 2007.

[86] U. Graf, M. Fieß, M. Schultze, R. Kienberger, F. Krausz, and E. Goulielmakis. Intense few-cycle light pulses in the deep ultraviolet. Optics Express, 16:18956, 2008.

[87] E. Goulielmakis, M. Schultze, M. Hofstetter, V. S. Yakovlev, J. Gagnon, M. Uiberacker, A. L. Aquila, E. M. Gullikson, D. T. Attwood, R. Kienberger, F. Krausz, and U. Kleineberg. Single-cycle nonlinear optics. Science, 320:1614, 2008.

[88] L. Misoguti, I. P. Christov, S. Backus, M. M. Murnane, and H. C. Kapteyn. Nonlinear wave-mixing processes in the extreme ultraviolet. Physical Review A, 72(6):063803, 2005.

[89] A. Rundquist, C. G. Durfee, Z. H. Chang, C. Herne, S. Backus, M. M. Murnane, and H. C. Kapteyn. Phase-matched generation of coherent soft X-rays. Science, 280(5368):1412, 1998.

[90] A. Paul, E. A. Gibson, X. S. Zhang, A. Lytle, T. Popmintchev, X. B. Zhou, M. M. Murnane, I. P. Christov, and H. C. Kapteyn. Phase-matching techniques for coherent soft X-ray generation. IEEE Journal of Quantum Electronics, 42(1-2):14, 2006.

[91] F. U. Hillebrecht, T. Kinoshita, D. Spanke, J. Dresselhaus, C. Roth, H. B. Rose, and E. Kisker. New magnetic linear dichroism in total photoelectron yield for magnetic domain imaging. Physical Review Letters, 75(11):2224, 1995.

[92] M. Sacchi, G. Panaccione, J. Vogel, A. Mirone, and G. van der Laan. Magnetic dichroism in reflectivity and photoemission using linearly polarized light: 3p core level of Ni(110). Physical Review B, 58(7):3750, 1998.

[93] M. Hecker, P. M. Oppeneer, S. Valencia, H. C. Mertins, and C. M. Schneider. Soft x-ray magnetic reflection spectroscopy at the 3p absorption edges of thin Fe films. Journal of Electron Spectroscopy, 144–147:881, 2005.

[94] H. C. Mertins, S. Valencia, D. Abramsohn, A. Gaupp, W. Gudat, and P. M. Oppeneer. X-ray Kerr rotation and ellipticity spectra at the 2p edges of Fe, Co, and Ni. Physical Review B, 69(6):064407, 2004.

[95] S. Ruegg, G. Schutz, P. Fischer, R. Wienke, W. B. Zeper, and H. Ebert. Spin-dependent x-ray absorption in Co/Pt multilayers. Journal of Applied Physics, 69(8):5655, 1991.

[96] C. T. Chen, F. Sette, Y. Ma, and S. Modesti. Soft-x-ray magnetic circular-dichroism at the $L_{2,3}$ edges of nickel. Physical Review B, 42(11):7262, 1990.

[97] T. Kiode, T. Shidara, H. Fukutani, K. Yamaguchi, A. Fujimori, and S. Kimura. Strong magnetic circular-dichroism at the $M_{2,3}$ edges in ferromagnetic Ni and ferrimagnetic Fe3O4. Physical Review B, 44(9):4697, 1991.

[98] T. Boske, W. Clemens, C. Carbone, and W. Eberhardt. Circular magnetic-x-ray dichroism of 3d impurities in Ni. Physical Review B, 49(6):4003, 1994.

[99] H. Hochst, D. Zhao, and D. L. Huber. $M_{2,3}$ magnetic circular dichroism (MCD) measurements of Fe, Co and Ni using a newly developed quadruple reflection phase shifter. Surface Science, 352:998, 1996.

[100] P. Kuiper, B. G. Searle, P. Rudolf, L. H. Tjeng, and C. T. Chen. X-ray magnetic dichroism of antiferromagnet Fe_2O_3 - the orientation of magnetic-moments observed by Fe 2p x-ray absorption-spectroscopy. Physical Review Letters, 70(10):1549, 1993.

[101] M. M. Schwickert, G. Y. Guo, M. A. Tomaz, W. L. O'Brien, and G. R. Harp. X-ray magnetic linear dichroism in absorption at the L edge of metallic Co, Fe, Cr, and V. Physical Review B, 58(8):R4289, 1998.

[102] H. C. Mertins, F. Schafers, X. Le Cann, A. Gaupp, and W. Gudat. Faraday rotation at the 2p edges of Fe, Co, and Ni. Physical Review B, 61(2):R874, 2000.

[103] H. C. Mertins, F. Schafers, and A. Gaupp. Soft-x-ray magneto-optical faraday effect on Fe and Co films. Europhysics Letters, 55(1):125, 2001.

[104] H. C. Mertins, F. Schafers, A. Gaupp, W. Gudat, J. Kunes, and P. M. Oppeneer. Soft X-ray magnetic dichroism and Faraday rotation measured with linearly polarised light. Nuclear Instruments and Methods in Physics Research A, 467–468:1407, 2001.

[105] J. Kunes, P. M. Oppeneer, H. C. Mertins, F. Schafers, A. Gaupp, W. Gudat, and P. Novak. X-ray Faraday effect at the L_2,L_3 edges of Fe, Co, and Ni: Theory and experiment. Physical Review B, 64(17):174417, 2001.

[106] S. Valencia, A. Gaupp, W. Gudat, H. C. Mertins, P. M. Oppeneer, D Abramsohn, and C. M Schneider. Faraday rotation spectra at shallow core levels: 3p edges of Fe, Co, and Ni. New Journal of Physics, 8:254, 2006.

[107] M. J. Freiser. A survey of magnetooptic effects. IEEE Transactions on Magnetics, MAG4(2):152, 1968.

[108] A. K Zvezdin and V. A. Kotov. Modern Magnetooptics and Magnetooptical Materials. Taylor and Francis, 1997.

[109] H. C. Mertins, S. Valencia, A. Gaupp, W. Gudat, P. M. Oppeneer, and C. M. Schneider. Magneto-optical polarization spectroscopy with soft X-rays. Applied Physics A, 80(5):1011, 2005.

[110] N. W. Ashcroft and N. D. Mermin. Solid State Physics. Brooks Cole, Florence, KY, first edition, 1976.

[111] David Attwood. Soft X-Rays and Extreme Ultraviolet Radiation. Cambridge University Press, Cambridge, United Kingdom, 2007.

[112] John Kerr. On rotation of the plane of the polarization by reflection from the pole of a magnet. Philosophical Magazine, 3(19), 1877.

[113] F. Schafers, H. C. Mertins, A. Gaupp, W. Gudat, M. Mertin, I. Packe, F. Schmolla, S. Di Fonzo, G. Soullie, W. Jark, et al. Soft-x-ray polarimeter with multilayer optics: complete analysis of the polarization state of light. Applied Optics, 38(19):4074, 1999.

[114] P. Antoine, B. Carre, A. L'Huillier, and M. Lewenstein. Polarization of high-order harmonics. Physical Review A, 55(2):1314, 1997.

[115] X. Zhou, R. Lock, N. Wagner, W. Li, H. C. Kapteyn, and M. M. Murnane. Elliptically polarized high-order harmonic emission from molecules in linearly polarized laser fields. Physical Review Letters, 102(7):073902, 2009.

[116] B. Vodungbo, A. B. Sardinha, J. Gautier, G. Lambert, C. Valentin, M. Lozano, G. Iaquaniello, F. Delmotte, S. Sebban, J. Luening, et al. Polarization control of high order harmonics in the EUV photon energy range. Optics Express, 19(5):4346, 2011.

[117] E. Hecht. Optics. Addison Wesley, Boston, 2001.

[118] A. Valterlaus, T. Beutler, and F. Meier. Spin-lattice relaxation-time of ferromagnetic gadolinium determined with time-resolved spin-polarized photoemission. Physical Review Letters, 67(23):3314, 1991.

[119] J. Hohlfeld, E. Matthias, R. Knorren, and K. H. Bennemann. Nonequilibrium magnetization dynamics of nickel. Physical Review Letters, 78(25):4861, 1997.

[120] A. Scholl, L. Baumgarten, R. Jacquemin, and W. Eberhardt. Ultrafast spin dynamics of ferromagnetic thin films observed by fs spin-resolved two-photon photoemission. Physical Review Letters, 79(25):5146, 1997.

[121] G. P. Ju, A. Vertikov, A. V. Nurmikko, C. Canady, G. Xiao, R. F. C. Farrow, and A. Cebollada. Ultrafast nonequilibrium spin dynamics in a ferromagnetic thin film. Physical Review B, 57(2):R700, 1998.

[122] U. Conrad, J. Gudde, V. Jahnke, and E .Matthias. Ultrafast electron and magnetization dynamics of thin Ni and Co films on cu(001) observed by time-resolved SHG. Applied Physics B, 68(3):511, 1999.

[123] J. Gudde, U. Conrad, V. Jahnke, J. Hohlfeld, and E. Matthias. Magnetization dynamics of Ni and Co films on Cu(001) and of bulk nickel surfaces. Physical Review B, 59(10):R6608, 1999.

[124] B. Koopmans, M. van Kampen, J. T. Kohlhepp, and W. J. M. de Jonge. Femtosecond spin dynamics of epitaxial Cu(111)/Ni/Cu wedges. Journal of Applied Physics, 87(9):5070, 2000.

[125] G. Malinowski, F. Dalla Longa, J. H. H. Rietjens, P. V. Paluskar, R. Huijink, H. J. M. Swagten, and B. Koopmans. Control of speed and efficiency of ultrafast demagnetization by direct transfer of spin angular momentum. Nature Physics, 4(11):855, 2008.

[126] F. Dalla Longa, J. T Kohlhepp, W. J. M de Jonge, and B Koopmans. Laser-induced magnetization dynamics in co/irmn exchange coupled bilayers, Jan 2008.

[127] F. Dalla Longa, J. T Kohlhepp, W. J. M de Jonge, and B Koopmans. Resolving the genuine laser-induced ultrafast dynamics of exchange interaction in ferromagnet/antiferromagnet bilayers. Phys Rev B, 81(9):094435, Jan 2010.

[128] G. M. Mueller, J. Walowski, M. Djordjevic, G. X. Miao, A. Gupta, A. V. Ramos, K. Gehrke, V. Moshnyaga, K. Samwer, J. Schmalhorst, et al. Spin polarization in half-metals probed by femtosecond spin excitation. Nature Materials, 8(1):56, 2009.

[129] J. Wang, C. Sun, J. Kono, A. Oiwa, H. Munekata, L. Cywinski, and L. J. Sham. Ultrafast quenching of ferromagnetism in InMnAs induced by intense laser irradiation. Physical Review Letters, 95(16):167401, 2005.

[130] I. Radu, K. Vahaplar, C. Stamm, T. Kachel, N. Pontius, H. A. Dürr, T. A. Ostler, J. Barker, R. F. L. Evans, R. W. Chantrell, et al. Transient ferromagnetic-like state mediating ultrafast reversal of antiferromagnetically coupled spins. Nature, 472:205, 2011.

[131] D. Steil, S. Alebrand, T. Roth, M. Krauss, T. Kubota, M. Oogane, Y. Ando, H. C. Schneider, M. Aeschlimann, and M. Cinchetti. Band-structure-dependent demagnetization in the heusler alloy co2mn1-xfexsi. Physical Review Letters, 105(21):217202, 2010.

[132] C. Boeglin, E. Beaurepaire, V. Halte, V. Lopez-Flores, C. Stamm, N. Pontius, H. A. Dürr, and J.-Y Bigot. Distinguishing the ultrafast dynamics of spin and orbital moments in solids. Nature, 465(7297):458, 2010.

[133] S. I. Anisimov, B. L. Kapeliovich, and T. L. Perelman. Electron-emission from surface of metals induced by ultrashort laser pulses. Soviet Physics - JETP, 39:375, 1974.

[134] F. Dalla Longa. Laser-induced magnetization dynamics - an ultrafast journey among spins and light pulses -. PhD thesis, Technische Universiteit Eindhoven, Jun 2008.

[135] Y. Yafet. Solid State Physics, volume 14. Academic, New York, 1963.

[136] I. Zutic, J. Fabian, and S. Das Sarma. Spintronics: Fundamentals and applications. Review of Moden Physics, 76(2):323, 2004.

[137] B. Koopmans, J. J. M. Ruigrok, F. Dalla Longa, and W. J. M. de Jonge. Unifying ultrafast magnetization dynamics. Physical Review Letters, 95(26):267207, Jan 2005.

[138] B. Koopmans, H. H. J. E. Kicken, M. van Kampen, and W. J. M. de Jonge. Microscopic model for femtosecond magnetization dynamics. Journal of Magnetism and Magnetic Materials, 286:271, 2005.

[139] I. Radu, G. Woltersdorf, M. Kiessling, A. Melnikov, U. Bovensiepen, J. U. Thiele, and C. H. Back. Laser-induced magnetization dynamics of lanthanide-doped Permalloy thin films. Physical Review Letters, 102(11):117201, 2009.

[140] J. Walowski, G. Mueller, M. Djordjevic, M. Muenzenberg, M. Klaeui, C. A. F Vaz, and J. A. C Bland. Energy equilibration processes of electrons, magnons, and phonons at the femtosecond time scale. Physical Review Letters, 101(23):237401, 2008.

[141] A. Einstein and W. J. de Haas. Experimenteller nachweis der ampereschen molekularströme. Verhandlungen der Deutschen Physikalischen Gesellschaft, 17:152, 1915.

[142] M. Krauss, T. Roth, S. Alebrand, D. Steil, M. Cinchetti, M. Aeschlimann, and H. C. Schneider. Ultrafast demagnetization of ferromagnetic transition metals: The role of the Coulomb interaction. Physical Review B, 80(18):180407, 2009.

[143] G. P. Zhang and W. Hubner. Laser-induced ultrafast demagnetization in ferromagnetic metals. Physical Review Letters, 85(14):3025, 2000.

[144] M. Lisowski, P. Loukakos, A. Melnikov, I. Radu, L. Ungureanu, M. Wolf, and U. Bovensiepen. Femtosecond electron and spin dynamics in Gd(0001) studied by time-resolved photoemission and magneto-optics. Physical Review Letters, 95(13):137402, 2005.

[145] L. Cywinski and L. J. Sham. Ultrafast demagnetization in the sp-d model: A theoretical study. Physical Review B, 76(4):045205, 2007.

[146] O. Chubykalo-Fesenko, U. Nowak, R. W. Chantrell, and D. Garanin. Dynamic approach for micromagnetics close to the Curie temperature. Physical Review B, 74(9):094436, 2006.

[147] D. A. Garanin. Fokker-Planck and Landau-Lifshitz-Bloch equations for classical ferromagnets. Physical Review B, 55(5):3050, 1997.

[148] U. Atxitia, O. Chubykalo-Fesenko, J. Walowski, A. Mann, and M. Muenzenberg. Evidence for thermal mechanisms in laser-induced femtosecond spin dynamics. Physical Review B, 81(17):174401, 2010.

[149] U. Atxitia, O. Chubykalo-Fesenko, N. Kazantseva, D. Hinzke, U. Nowak, and R. W. Chantrell. Micromagnetic modeling of laser-induced magnetization dynamics using the landau-lifshitz-bloch equation. Applied Physics Letters, 91(23):232507, 2007.

[150] N. Kazantseva, U. Nowak, R. W. Chantrell, J. Hohlfeld, and A. Rebei. Slow recovery of the magnetisation after a sub-picosecond heat pulse. Europhysics Letters, 81(2):27004, 2008.

[151] S. Backus, C. G. Durfee, M. M. Murnane, and H. C. Kapteyn. High power ultrafast lasers. Review of Scientific Instruments, 69(3):1207, 1998.

[152] R. Trebino, K. W. DeLong, D. N. Fittinghoff, J. N. Sweetser, M. A. Krumbugel, B. A. Richman, and D. J. Kane. Measuring ultrashort laser pulses in the time-frequency domain using frequency-resolved optical gating. Review of Scientific Instruments, 68(9):3277, 1997.

[153] R Abrams. Coupling losses in hollow waveguide laser resonators. IEEE Journal of Quantum Electronics, 8(11):838, 1972.

[154] Ariel J. Paul. Coherent EUV Light from High-Order Harmonic Generation: Enhancement and Applications to Lensless Diffractive Imaging. PhD thesis, University of Colorado, 2007.

[155] Z. H. Loh, M. Khalil, R. E. Correa, and S. R. Leone. A tabletop femtosecond time-resolved soft x-ray transient absorption spectrometer. Review of Scientific Instruments, 79(7):073101, 2008.

[156] M Siemens. Nanoscale thermal, acoustic, and magnetic dynamics probed with soft x-ray light. PhD thesis, University of Colorado, 2009.

[157] The ARRL Handbook for Radio Communications. The American Radio Relay League, Inc., Newington, CT, 89th edition, 2010.

[158] C. Tannous and J. Gieraltowski. The stoner–wohlfarth model of ferromagnetism. European Journal of Physics, 29(3):475, 2008.

[159] SA Wolf, DD Awschalom, RA Buhrman, JM Daughton, S von Molnar, ML Roukes, AY Chtchelkanova, and DM Treger. Spintronics: A spin-based electronics vision for the future, Jan 2001.

[160] J. Zhou, J. Peatross, M. M. Murnane, H. C. Kapteyn, and I. P. Christov. Enhanced high-harmonic generation using 25 fs laser pulses. Physical Review Letters, 76(5):752, 1996.

[161] C.-G. Wahlström, J. Larsson, A. Persson, T. Starczewski, S. Svanberg, P. Salières, Ph. Balcou, and Anne L'Huillier. High-order harmonic generation in rare gases with an intense short-pulse laser. Physical Review A, 48(6):4709, 1993.

[162] T. Kanai, A. Suda, S. Bohman, M. Kaku, S. Yamaguchi, and K. Midorikawa. Pointing stabilization of a high-repetition-rate high-power femtosecond laser for intense few-cycle pulse generation. Applied Physics Letters, 92(6):061106, 2008.

[163] L. Miaja-Avila, G. Saathoff, S. Mathias, J. Yin, C. La-o vorakiat, M. Bauer, M. Aeschlimann, M. M. Murnane, and H. C. Kapteyn. Direct measurement of core-level relaxation dynamics on a surface-adsorbate system. Physical Review Letters, 101(4):046101, 2008.

[164] B. Dieny. Quantitative interpretation of giant magnetoresistance properties of Permalloy-based spin-valve structures. Europhysics Letters, 17(3):261, 1992.

[165] W. P. Pratt, Q. Yang, L. L. Henry, P. Holody, W.C. Chiang, P. A. Schroeder, and J. Bass. How predictable is the current perpendicular to plane magnetoresistance? Applied Physics Letters, 79(8):5811, 1996.

[166] D. M. C. Nicholson, W. H. Butler, W. A. Shelton, Y. Wang, X.-G. Zhang, G. M. Stocks, and J. M. MacLaren. Magnetic structure and electronic transport in permalloy. Journal of Applied Physics, 81(8):4023, 1997.

[167] B. A. Gurney, V. S. Speriosu, J. P. Nozieres, H. Lefakis, D. R. Wilhoit, and O. U. Need. Direct measurement of spin-dependent conduction-electron mean free paths in ferromagnetic metals. Physical Review Letters, 71(24):4023, 1993.

[168] F. J. Himpsel, J. E. Ortega, G. J. Mankey, and R. F. Willis. Magnetic nanostructure. Advances in Physics, 47(4):511, 1998.

[169] A. C. Thompson, D. T. Attwood, E. M. Gullikson, M. R. Howells, J. B. Kortright, A L. Robinson, J. H. Underwood, K. J. Kim, J. Kirz, I. Lindau, et al. X-ray Data Booklet. Center for X-ray Optics and Advanced Light Source, second edition edition, 2001.

[170] H. B. Callen. Green function theory of ferromagnetism. Physical Review, 130(3):890, 1963.

[171] M. F. Collins, V. J. Minikiewicz, R. Nathans, L. Passell, and G. Shirane. Critical and spin-wave scattering of neutrons from iron. Physical Review, 179(2):417, 1969.

[172] Time-resolved Magnetic Asymmetry of Permalloy-Cu, http://www.youtube.com/watch?v=AALfi21Gx_E, 2011.

[173] K. Chen and D. P. Landau. Spin-dynamics study of the dynamic critical behavior of the three-dimensional classical Heisenberg ferromagnet. Physical Review B, 49(5):3266, 1994.

[174] S. Mathias, C. La-O-Vorakiat, P. Grychtol, J. M. Shaw, R. Adam, H. T. Nembach, M. E. Siemens, S. Eich, C. M. Schneider, T. J. Silva, et al. Ultrafast decoupling of magnetization dynamics in an alloy. submitted, 2011.

[175] R. Huber, F. Tauser, A. Brodschelm, M. Bichler, G. Abstreiter, and A. Leitenstorfer. How many-particle interactions develop after ultrafast excitation of an electron–hole plasma. Nature, 414(286), 2001.

[176] H. S. Rhie, H. A. Dürr, and W. Eberhardt. Femtosecond electron and spin dynamics in Ni/W(110) films. Physical Review Letters, 90(24):247201, 2003.

[177] M. Grimsditch and P. Vavassori. The diffracted magneto-optic Kerr effect: what does it tell you? Journal of Physics: Condensed Matter, 16(9):R275, 2004.

[178] E. Carpene, E. Mancini, C. Dallera, M. Brenna, E. Puppin, and S. De Silvestri. Dynamics of electron-magnon interaction and ultrafast demagnetization in thin iron films. Physical Review B, 78(17):174422, 2008.

[179] Luxpop Inc. Thin film and bulk index of refraction and photonics calculations, http://www.luxpop.com/, August 2011.

[180] M. Cinchetti, M. Sanchez Albaneda, D. Hoffmann, T. Roth, J.-P. Wuestenberg, M. Krauss, O. Andreyev, H. C. Schneider, M. Bauer, and M. Aeschlimann. Spin-flip processes and ultrafast magnetization dynamics in Co: Unifying the microscopic and macroscopic view of femtosecond magnetism. Physical Review Letters, 97(17):177201, 2006.

[181] M. van Kampen, J. T. Kohlhepp, W. J. M. de Jonge, B. Koopmans, and R. Coehoorn. Sub-picosecond electron and phonon dynamics in nickel. Journal of Physics: Condensed Matter, 17(43):6823, 2005.

[182] J. Y. Bigot, M. Vomir, L. H. F. Andrade, and E. Beaurepaire. Ultrafast magnetization dynamics in ferromagnetic cobalt: The role of the anisotropy. Chemical Physics, 318(1-2):137, 2005.

[183] C. Kittel. Introduction to Solid State Physics. Wiley, Hoboken, NJ, eighth edition, Nov 2004.

[184] A. P. Caffrey, P. E. Hopkins, J. M. Klopf, and P. M. Norris. Thin film non-noble transition metal thermophysical properties. Microscale Thermophysical Engineering, 9(4):365, 2005.

[185] P. M. Norris, A. P. Caffrey, R. J. Stevens, J. M. Klopf, J. T. McLeskey, and A. N. Smith. Femtosecond pump-probe nondestructive examination of materials. Rev Sci Instrum, 74(1):400, 2003.

[186] P. B. Johnson and R. W. Christy. Optical constants of transition metals: Ti, V, Cr, Mn, Fe, Co, Ni, and Pd. Physical Review B, 9(12):5056, 1974.

[187] R. L. Sandberg, C. Song, P. W. Wachulak, D. A. Raymondson, A. Paul, B. Amirbekian, E. Lee, A. E. Sakdinawat, C. La-O-Vorakiat, M. C Marconi, et al. High numerical aperture tabletop soft x-ray diffraction microscopy with 70-nm resolution. Proceedings of the National Academy of Sciences, 105(1):24, 2008.

[188] R. L Sandberg, D. A. Raymondson, C. La o Vorakiat, A. Paul, K. S. Raines, J. Miao, M. M. Murnane, H. C. Kapteyn, and W. F. Schlotter. Tabletop soft-x-ray Fourier transform holography with 50 nm resolution. Optics Letters, 34(11):1618, 2009.

[189] J. R. Fienup. Phase retrieval algorithms - a comparison. Applied Optics, 21(15):2758, 1982.

[190] B. Abbey, K. A. Nugent, G. J. Williams, J. N. Clark, A. G. Peele, M. A. Pfeifer, M. De Jonge, and I. McNulty. Keyhole coherent diffractive imaging. Nature Physics, 4(5):394, 2008.

[191] P. Thibault, M. Dierolf, A. Menzel, O. Bunk, C. David, and F. Pfeiffer. High-resolution scanning x-ray diffraction microscopy. Science, 321(5887):379, 2008.

[192] H. N. Chapman and K. A. Nugent. Coherent lensless x-ray imaging. Nature Photonics, 4(12):833, 2010.

[193] I. McNulty, J. Kirz, C. Jacobsen, E. H. Anderson, M. R. Howells, and D. P. Kern. High-resolution imaging by fourier transform x-ray holography. Science, 256(5059):1009, 1992.

[194] S. Eisebitt, M. Lorgen, W. Eberhardt, J. Luning, S. Andrews, and J. Stöhr. Scalable approach for lensless imaging at x-ray wavelengths. Applied Physics Letters, 84(17):3373, 2004.

[195] W. F. Schlotter, R. Rick, K. Chen, A. Scherz, J. Stöhr, J. Luening, S. Eisebitt, Ch. Guenther, W. Eberhardt, O. Hellwig, and I. McNulty. Multiple reference fourier transform holography with soft x rays. Applied Physics Letters, 89(16):163112, 2006.

[196] M. D. Seaberg, D. E. Adams, W. F. Schlotter, Y. Liu, C. Menoni, M. Murnane, and H. C. Kapteyn. Sub-30nm spatial resolution imaging using a tabletop 13nm high harmonic source. In CLEO:2011 - Laser Applications to Photonic Applications, page CTuH3. Optical Society of America, 2011.

[197] R. A. Dilanian, B. Chen, G. J. Williams, H. M. Quiney, K. A. Nugent, S. Teichmann, P. Hannaford, L. V. Dao, and A. G. Peele. Diffractive imaging using a polychromatic high-harmonic generation soft-x-ray source. Journal of Applied Physics, 106(2):023110, 2009.

[198] D. Gauthier, M. Guizar-Sicairos, X. Ge, W. Boutu, B. Carre, J. R. Fienup, and H. Merdji. Single-shot femtosecond x-ray holography using extended references. Physical Review Letters, 105(9):093901, 2010.

[199] M. R. Weiss, R. Follath, K. J. S. Sawhney, F. Senf, J. Bahrdt, W. Frentrup, A. Gaupp, S. Sasaki, M. Scheer, H. C. Mertins, D. Abramsohn, F. Schafers, W. Kuch, and W. Mahler. The elliptically polarized undulator beamlines at bessy ii. Nuclear Instruments and Methods in Physics Research Section A, 467:449, 2001.

[200] P. Fischer, T. Eimuller, G. Schutz, G. Denbeaux, A. Pearson, L. Johnson, D. Attwood, S. Tsunashima, M. Kumazawa, N. Takagi, et al. Element-specific imaging of magnetic domains at 25 nm spatial resolution using soft x-ray microscopy. Review of Scientific Instruments, 72(5):2322, 2001.

[201] A. Scholl, H. Ohldag, F. Nolting, J. Stöhr, and H. A. Padmore. X-ray photoemission electron microscopy, a tool for the investigation of complex magnetic structures. Review of Scientific Instruments, 73(3):1362, 2002.

[202] S. Eisebitt, J. Luning, W. F. Schlotter, M. Lorgen, O. Hellwig, W. Eberhardt, and J. Stöhr. Lensless imaging of magnetic nanostructures by x-ray spectroholography. Nature, 432(7019):885, 2004.

[203] O. Hellwig, S. Eisebitt, W. Eberhardt, W. F. Schlotter, J. Luning, and J. Stöhr. Magnetic imaging with soft x-ray spectroholography. Journal of Applied Physics, 99(8):08H307, 2006.

[204] S. Roy, D. Parks, K. A. Seu, R. Su, J. J. Turner, W. Chao, E. H. Anderson, S. Cabrini, and S. D. Kevan. Lensless x-ray imaging in reflection geometry. Nature Photonics, 5(4):243, 2011.

[205] B. Pfau, C. M. Guenther, R. Koennecke, E. Guehrs, O. Hellwig, W. F. Schlotter, and S. Eisebitt. Magnetic imaging at linearly polarized x-ray sources. Optics Express, 18(13):13608, 2010.

[206] G. Vampa, A. Simoncig, B. Ressel, A. Aquila, E. Gullikson, F. Salmassi, D. Attwood, M. Malvestuto, L. Stebel, and F. Parmigiani. Multilayer optics for time resolved euv-magnetic circular dichroism experiments with hhg sources. submitted, 2011.

[207] A. Tripathi, J. Mohanty, S. Dietze, O. G. Shpyrko, E. Shipton, E. E. Fullerton, S. S. Kim, and I. McNulty. Dichroic coherent diffractive imaging. Proceedings of the National Academy of Sciences, 10.1073/pnas.1104304108, 2011.

[208] J. Turner, X. Huang, O. Krupin, K. Seu, D. Parks, S. Kevan, E. Lima, K. Kisslinger, I. McNulty, R. Gambino, et al. X-ray diffraction microscopy of magnetic structures. Physical Review Letters, 107(3):033904, 2011.

[209] J. B. Kortright, S. K. Kim, G. P. Denbeaux, G. Zeltzer, K. Takano, and E. E. Fullerton. Soft-x-ray small-angle scattering as a sensitive probe of magnetic and charge heterogeneity. Physical Review Bl, 64(9):092401, 2001.

[210] J. B. Kortright, O. Hellwig, D. T. Margulies, and E. E. Fullerton. Resolving magnetic and chemical correlations in coptcr films using soft x-ray resonant scattering. Journal of Magnetism and Magnetic Materials, 240(1-3):325, 2002.

[211] E. E. Fullerton, O. Hellwig, Y. Ikeda, B. Lengsfield, K. Takano, and J. B. Kortright. Soft x-ray characterization of perpendicular recording media. IEEE Transactions on Magnetics, 38(4):1693, 2002.

[212] O. Hellwig, G. P. Denbeaux, J. B. Kortright, and E. E. Fullerton. X-ray studies of aligned magnetic stripe domains in perpendicular multilayers. Physica B, 336(1-2):136, 2003.

[213] O. Hellwig, T. L. Kirk, J. B. Kortright, A. Berger, and E. E. Fullerton. A new phase diagram for layered antiferromagnetic films. Nature Materials, 2(2):112, 2003.

[214] J. B. Kortright, O. Hellwig, K. Chesnel, S. H. Sun, and E. E. Fullerton. Interparticle magnetic correlations in dense co nanoparticle assemblies. Physical Review B, 71(1):012402, 2005.

[215] O. Hellwig, A. Berger, J. B. Kortright, and E. E. Fullerton. Domain structure and magnetization reversal of antiferromagnetically coupled perpendicular anisotropy films. Journal of Magnetism and Magnetic Materials, 319(1-2):13, 2007.

[216] M. S. Pierce, C. R. Buechler, L. B. Sorensen, S. D. Kevan, E. A. Jagla, J. M. Deutsch, T. Mai, O. Narayan, J. E. Davies, K. Liu, et al. Disorder-induced

magnetic memory: Experiments and theories. Physical Review B, 75(14):144406, 2007.

[217] S. Mangin, T. Hauet, P. Fischer, D. H. Kim, J. B. Kortright, K. Chesnel, E. Arenholz, and E. E. Fullerton. Influence of interface exchange coupling in perpendicular anisotropy [pt/co](50)/tbfe bilayers. Physical Review B, 78(2):024424, 2008.

[218] C. Gutt, S. Streit-Nierobisch, L.-M. Stadler, B. Pfau, C. M. Günther, R. Könnecke, R. Frömter, A. Kobs, D. Stickler, H. P. Oepen, et al. Single-pulse resonant magnetic scattering using a soft x-ray free-electron laser. Physical Review B, 81(10):100401, 2010.

[219] B. Vodungbo, A. Barszczak Sardinha, J. Gautier, G. Lambert, M. Lozano, S. Sebban, E. Meltchakov, F. Delmotte, V. Lopez-Flores, J. Arabski, et al. Table-top resonant magnetic scattering with extreme ultraviolet light from high-order harmonic generation. Europhysics Letters, 94(5):54003, 2011.

[220] L. Landau. On the theory of phase transitions. Soviet Physics - JETP, 7:19, 1937.

Appendix A

Mean Field Theories

A.1 The Landau theory

In this chapter, a mean field theory by Landau will be summarized [220]. The theory is useful for explaining the critical phenomena when the temperature of ferromagnetic materials approaches to Curie temperatures. The analysis starts with the free energy that is defined as

$$G(H,T) = F(M,T) - \mu_0 HM. \tag{A.1}$$

The magnetization (M) at equilibrium can be derived from this free energy by finding M that minimizes the function. First, the free energy ($G(H,T)$) is expanded by a Taylor series of magnetization M. Only the even-order terms are in the expansion because of the time reversal symmetry, i.e. without any external magnetic field ($G(H=0,T)$), the free energy should be identical regardless of the magnetization sign: $F(M,T) = F(-M,T)$:

$$G(H,T) = AM^2 + BM^4 + CM^6 + ... - \mu_0 HM \tag{A.2}$$

where $A, B, C...$ are dependent from the temperature. To simplify the algebra, the series is expanded up to 4th order in M. The zeroth order in M is set to zero since it is just an energy offset. The function form of the free energy can be deduced from three observations (Figure A.1);

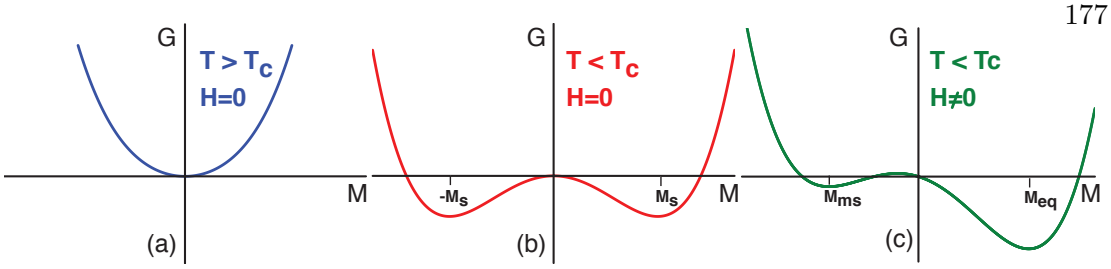

Figure A.1: Gibbs free energy from three special cases: with zero external magnetic field $H = 0$ at (a) $T > T_c$ (b)$T > T_c$, and (c) with applied magnetic field below T_c. The magnetization at thermal equilibrium can be found from the minima of each free energy curve. In (b), the two possible states of spontaneous magnetization are marked as M_s. And, in (c), the magnetic field distorts the free energy curve resulting in only one global minimum labeled as M_{eq}. The other possible magnetization is in the metastable state, M_{ms}

(1) No spontaneous magnetization should be present above T_c. When $T > T_c$ and $H = 0$, G should have only one global minimum at $M = 0$.

(2) Magnetization should exist when $T < T_c$ and $H = 0$. However, there is no constraint for the magnetization to align at any particular direction, and both states should have identical energy. Then G should have two local minima at $\pm M_s$ when $T < T_c$ and $H = 0$.

(3) If the magnetic field is applied blelow T_c, the symmetry of the free energy function should be broken. And the magnetization, M, should have oriented along the magnetic-field direction. And G should have only one global minima because of the distortion in $F(M, T)$ by the term $\mu_0 HM$.

In order to achieve the first two requirements, the second-order explansion constant A has to be negative when $T < T_c$ and positive when $T > T_c$, if B is always positive. At this condition, A should change sign at $T = T_c$ and can be written in the form of $a(T - T_c)$ as $a > 0$. Then Equation A.2 can be written as

$$G(H, T) = a(T - T_c)M^2 + BM^4 - \mu_0 HM \tag{A.3}$$

To search for magnetization at equilibrium without an external magnetic field,

i.e. spontaneous magnetization (M_s), we need to solve for the local minima from the free-energy function when $\frac{\partial G}{\partial M} = 0$, which is

$$2a(T - T_c)M_{eq} + 4BM_{eq}^3 = \mu_0 H, \tag{A.4}$$

where eq is label to indicate the equilibrium state but with the presence of magnetic field. By setting $H = 0$, the spontaneous magnetization becomes

$$M_{s,eq} = \pm\sqrt{\frac{a(T - T_c)}{2B}}. \tag{A.5}$$

Here, we have derived an important equation showing that by the Laudau's theory, the spontaneous magnetization approaches Curie temperature by a square-root function. However, with an external magnetic field, the magnetization is not exactly zero above the Curie temperature. And this small amount of magnetization at the Curie temperature can be found from Equation A.4,

$$M_{eq}(T = T_c) = (\frac{\mu_0 H}{4B})^{\frac{1}{3}}. \tag{A.6}$$

In general, the equilibrium magnetization cannot be written in an analytical form, and only numerical solution can be obtained (Figure A.2) by solving Equation A.4 numerically.

A.2 Weiss Molecular-Field Theory

The first attempt to explain ferromagnetic phenomena has been dedicated to Pierre Weiss. He made an assumption about the existence of the"molecular magnetic field," which is proportional to magnetization:

$$\mathbf{H}_w = n_w \mathbf{M}. \tag{A.7}$$

The proportional constant n_w is typically in the range of 10-100, and this field is added to the contribution from the applied magnetic field H.

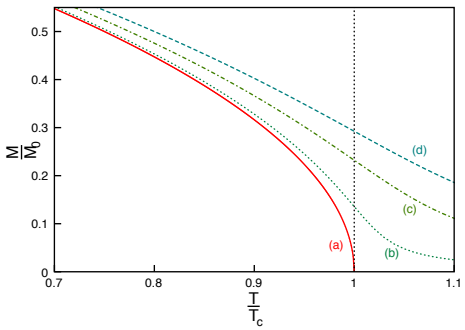

Figure A.2: Equilibrium magnetization calculated from Landau's theory normalized by the value at $T = 0K$ as a function of temperature normalized to T_c. The plots show four different cases when the magnetic field H is increased from zero in (a) to (d).

To calculate the magnetization, the amount of magnetic moment per unit volume, we need to perform the thermodynamic average,

$$\langle m_z \rangle = \frac{\sum_i m_i exp(-\varepsilon_i / k_B T)}{\sum_i exp(-\varepsilon_i / k_B T)} \tag{A.8}$$

where i is summed over all possible J quantum number. The states are labeled by quantum numbers M_J and have $2J + 1$ in total. The energy of each state ε_i can be written as

$$\varepsilon_i = \varepsilon_{M_J} = \mu_0 m_i H_{tot} = \mu_0 g \mu_B M_J (n_w M + H) \tag{A.9}$$

These summations can be executed analytically [1], and the result is

$$\langle m_z \rangle = m_0 B_J(x) \tag{A.10}$$

where

$$B_J(x) = \frac{2J+1}{2J} \coth \frac{2J+1}{2J} x - \frac{1}{2J} \coth \frac{x}{2J}, \tag{A.11}$$

where

$$x = \frac{\mu_0 g \mu_B (n_w M + H) J}{k_B T}, \tag{A.12}$$

and $m_0 = g \mu_B J$, which is the maximum magnetic moment allowed in each state.

The magnetization which is a macroscopic version of $\langle m_z \rangle$ can be found by scaling the parameter by the number of atoms per volume,

$$M = n\langle m_z \rangle = M_0 B_J(\frac{\mu_0 g \mu_B (n_w M + H) J}{k_B T}). \tag{A.13}$$

With the presence of Weiss field ($n_w M$), the average M becomes a transcendental equation, and M is need to be solved numerically. For the spontaneous magnetization, where H is set to zero, this equation is simplified to

$$\frac{M_s}{M_0} = B_J(x_0), \tag{A.14}$$

where $x_0 = \frac{\mu_0 g \mu_B n_w M_s J}{k_B T} = \frac{\mu_0 m_0 n_w M_s}{k_B T}$. And by defining $M_0 = n m_0$, as magnetization at $T = 0K$, the ratio becomes

$$\frac{M_s}{M_0} = \frac{k_B T x_0}{\mu_0 n_w n m_0^2}. \tag{A.15}$$

By solving these two equations numerically, we can calculate the spontaneous magnetization; however, the Equation (A.15) can be parameterized with the paramagnetic Curie constant (C) by considering the high temperature limit of the function $B_J(x)$ with $x \ll 1$:

$$B(J) \approx \frac{J(J+1)}{3J} x. \tag{A.16}$$

At high temperature limit, the Weiss's term n_w is not very important since we will see in the short coming that this term is small at high temperature (and zero above T_C) as the ferromagnetic contribution to the magnetization is small. The magnetization then becomes

$$M = n\langle m_z \rangle = n(m_0 \frac{(J+1)}{3J}) \frac{\mu_0 m_0 H}{k_B T} = \frac{\mu_0 g^2 n J (J+1) \mu_B^2}{3 k_B T} H. \tag{A.17}$$

Near Curie temperature, the (paramagnetic) magnetization is linear in H and inversely proportion to temperature T. This follows form of the Curie's law where the susceptibility $\chi = \frac{\partial M}{\partial H}$ can be written as

$$\chi = \frac{C}{T}, \tag{A.18}$$

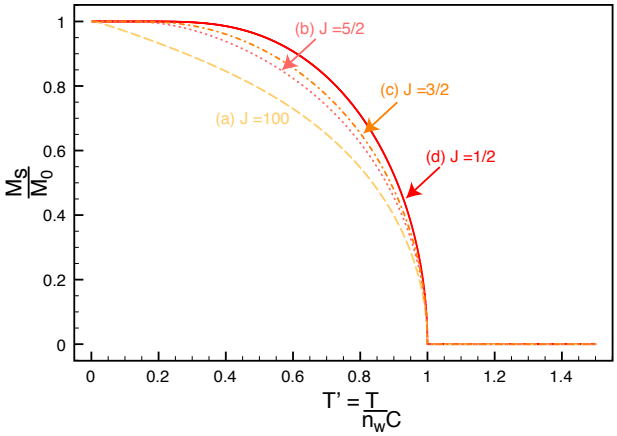

Figure A.3: Spontaneous magnetization normalized by the maximum possible value of magnetization, $M_0 = ng\mu_B J$ of the giving J quantum number, when all of the spin states on all atoms are identical at the absolution zero. The temperature is scaled by Curie temperature $T_C = n_w C$.

where the Curie's constant C is $\frac{\mu_0 g^2 n J(J+1)\mu_B^2}{3k_B}$. Equation A.15 is then converted to

$$\frac{M_s}{M_0} = \frac{T(J+1)}{3JCn_w} x_0. \tag{A.19}$$

After writing the temperature in the reduced unit of $T' = \frac{T}{Cn_w}$, the solutions to the simultaneous equations (Equation A.14 and A.19), for various values J is shown in Figure A.3

Weiss's model can reproduce the temperature function form of the spontaneous magnetization curves of ferromagnets. The theory predicts the disappearance of magnetization at the temperature $T' = 1$. Therefore, it is appropriate to define the Curie temperature as

$$T_c = Cn_w. \tag{A.20}$$

Finally, at $T = 0K$, Weiss model has the solution of $M = M_0$, which makes sense because all atomic states are in the ground state to minimize the total energy of the system.

Appendix B

MATLAB Code for Calibrating High-Harmonic Spectra

In this appendix, I present a simple Matlab code for calibrating of high-harmonic spectra from diffraction patterns from CCD camera employed in the thesis. The code is useful in general for any spectrometry of the high harmonics. The code requires the exact knowledge of grating period, the sample-to-CCD distance and CCD pixel size, while rough ideas for angle of incident, photon-energy range.

```
%%%%%%%%%%%%%%%%%%%%%%%%%%%%%%%%%%%%%%%%%%%%%%%%

% load data and background

data1 = importdata('mean_even.txt');

data2 = importdata('mean_odd.txt');


% background subtraction

bg1 = mean(data1(484:496));

bg2 = mean(data2(484:496));

data1 = data1 - bg1;

data2 = data2 - bg2;


% calculate the asymmetry

asy = (data1-data2)./(data1+data2);
```

```
% plot two spectra
figure(22),plot(data1,'red');
hold on
figure(22), plot(data2,'blue');
hold off

% parameters
% grating period in m
d = 4E-6;
% CCD size in m
D= 26E-6;
% Plank's constant
h= 6.6256E-34;
% speed of light in m/s
c= 299792458;
% electron charge in Coulomb
e = 1.602E-19;
% zeroth order pixel number
center = 606;
% the angle of incidence in radian
alpha = 45*180/pi;
% sample to CCD distance in m
z = 0.3;
% diffracted distance along the CCD chip of harmonics in pixel
n = abs(center-[408 402 395 386 377 365]);
```

```
% Then define then harmonic order N corresponding to the above harmonics
% The number shown below are good for HHG from Ne with energy around % 70
eV.
% Use N = [21 23 25 27 29 31] for HHG from Ar for energy around % 42 eV
% If these set of number does not give a good fit, try changing % N by ±
2.
N = [23 25 27 29 31 33 35 37 39 41 43];

lamb_bar = (h*c/e./N)';

% fit x=lamb_bar y=n with a Matlab function for E_0
% define fitting function in the form of (arcsin(x/(E_0*d) - sin(alpha)) + alpha)*z/D
% and set d, D, alpha, and z as constants.
% then, determine 'x' as the only independent variable while E_0 % is the
only free parameter.
fit_equation = sprintf('(asin(x./E_0/%f-sin(%f))+%f)*%f/D' ...
d,alpha,alpha,z,D);
fit_fn= fittype(fit_equation,'independent','x','coefficient','E_0');

% setup the upper and lower bound together with the starting value % to the
fit
fit_options = fitoptions(fit_fn);
fit_options.StartPoint = [1.5];
fit_options.Upper = [3];
fit_options.Lower = [0];

% start the fit and show the fit result (with the error value)
```

```
fit_result = fit(lamb_bar,n,fit_fn,fit_options)


% plot the fit result

figure(55), plot(lamb_bar,n,'.');

hold on

figure(55), plot(fit_result);

hold off


% extract the fit value

E_0 = fit_result.E_0;


% label the harmonics with energy to check the quality of the fit


%plot spectrum with energy labels for first order pattern

all_order = [21:2:43];

     for harmonics=1:size(all_order,2)

     label = sprintf('\\leftarrow %.2f eV',all_order(harmonics)*E_0);

     pixel = round(center-(asin(2*h*c/e/all_order(harmonics)/E_0/d...

     -sin(alpha))+alpha)*z/D);

     if pixel > 0 & pixel<1024

     figure(22),text(pixel,data2(pixel)+100,label,'horizontalalignment'...

     ,'left','rotation',90,'color','green')

     end

     end


% export the spectra with x-axis as the photon energy

pix = [293:476];
```

```
photon_energy = h*c/e./(d*(sin(D/z*(center-pix)-alpha)+sin(alpha)));
dlmwrite('data1.txt',[photon_energy' data1(pix)],'delimiter','')
dlmwrite('data2.txt',[photon_energy' data2(pix)],'delimiter','')
dlmwrite('asymmetry.txt',[photon_energy' asy(pix)],'delimiter','')

%%%%%%%%%%%%%%%%%%%%%%%%%%%%%%%%%%%%%%%%%%%%%%%%
```

The outputs from this simple code are shown in Figure B.1 and B.2. I can determine the photon energies of harmonics, although the quality of the spectrum is bad, as in Figure B.2).

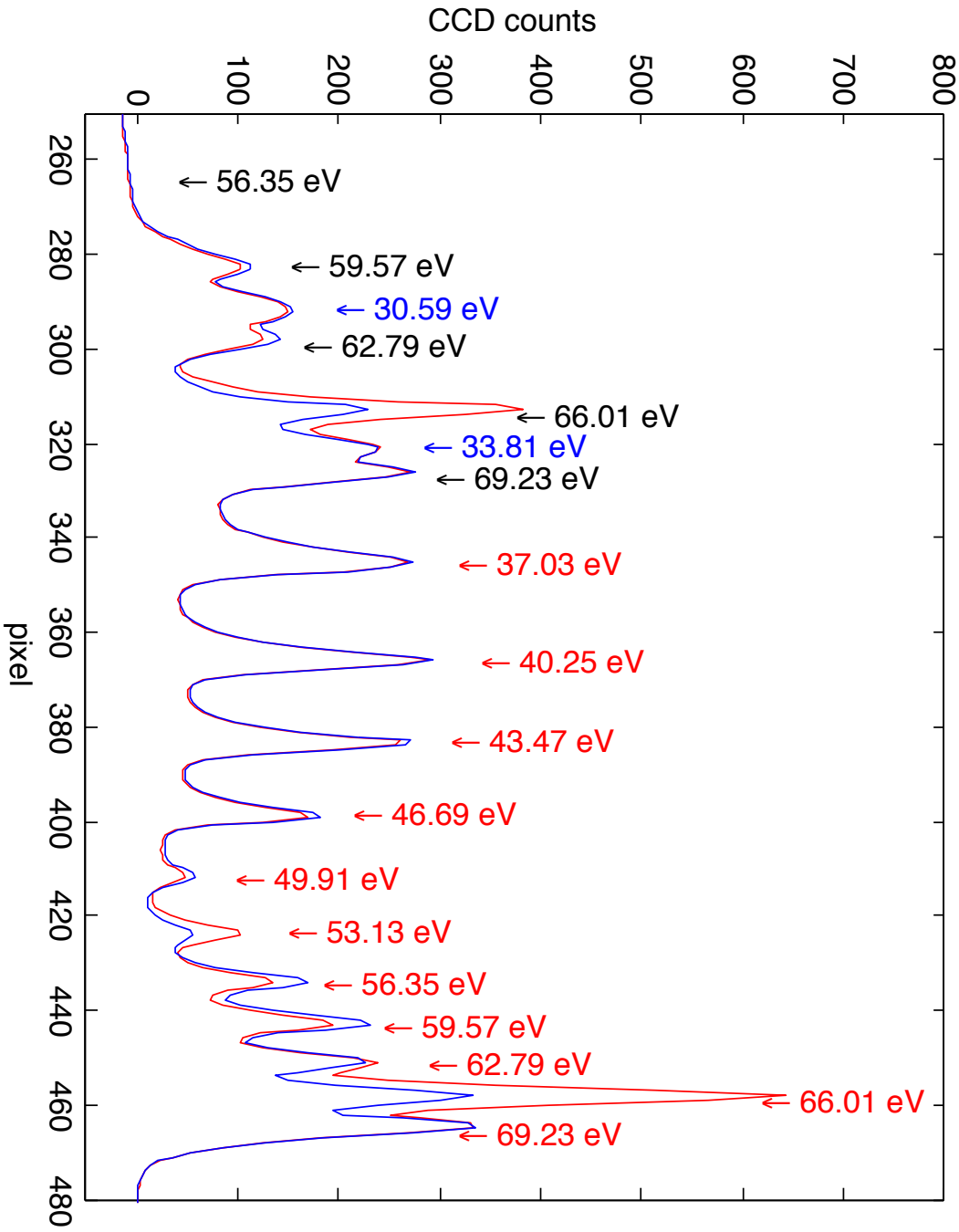

Figure B.1: Output from the code. The raw diffraction patterns (red and blue for two signs of magnetic field) from Permalloy grating at 45° are plot with the calibrated photon energy from the fit indicated on the top. The harmonics used as an input for the fitting are in red. With the optimized value of the fundamental energy, the code extrapolates to lower energy harmonics (blue), the second order diffraction pattern (black) and the negative diffraction order (Figure B.2).

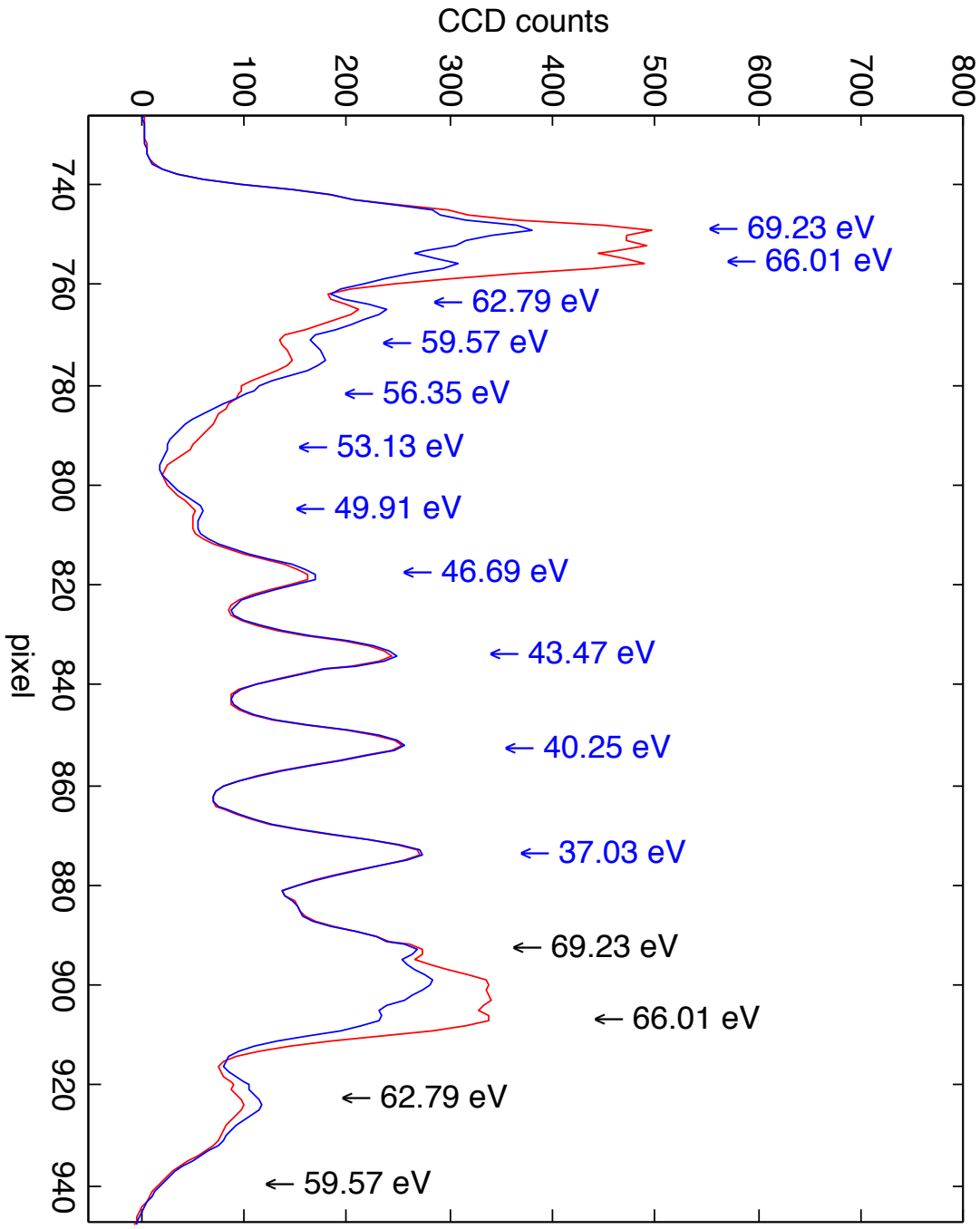

Figure B.2: Extrapolation of the fit results from the fitting code shown in Figure B.1 for the negative first (blue) and second (black) orders

Appendix C

Electronic Diagrams

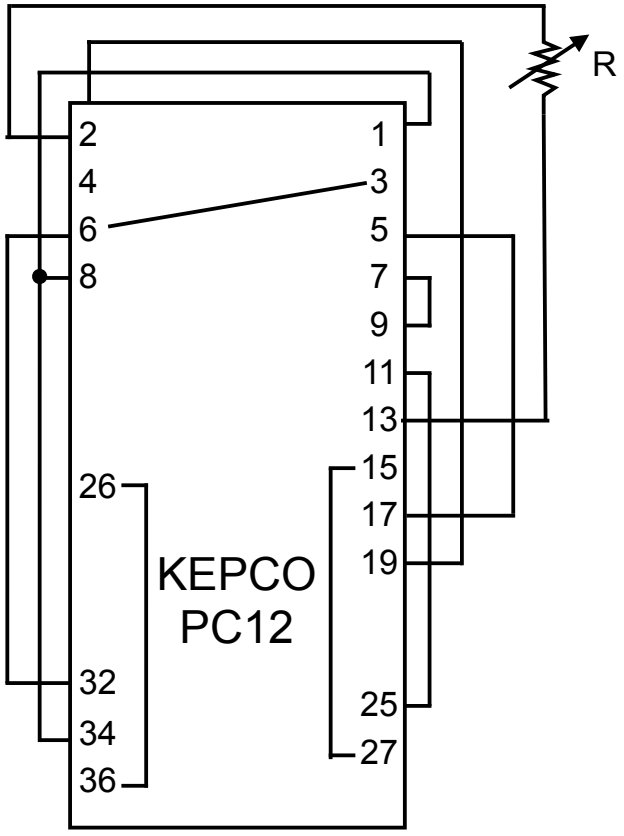

Figure C.1: KEPCO PC12 (located at the back of the power supply) connection diagram

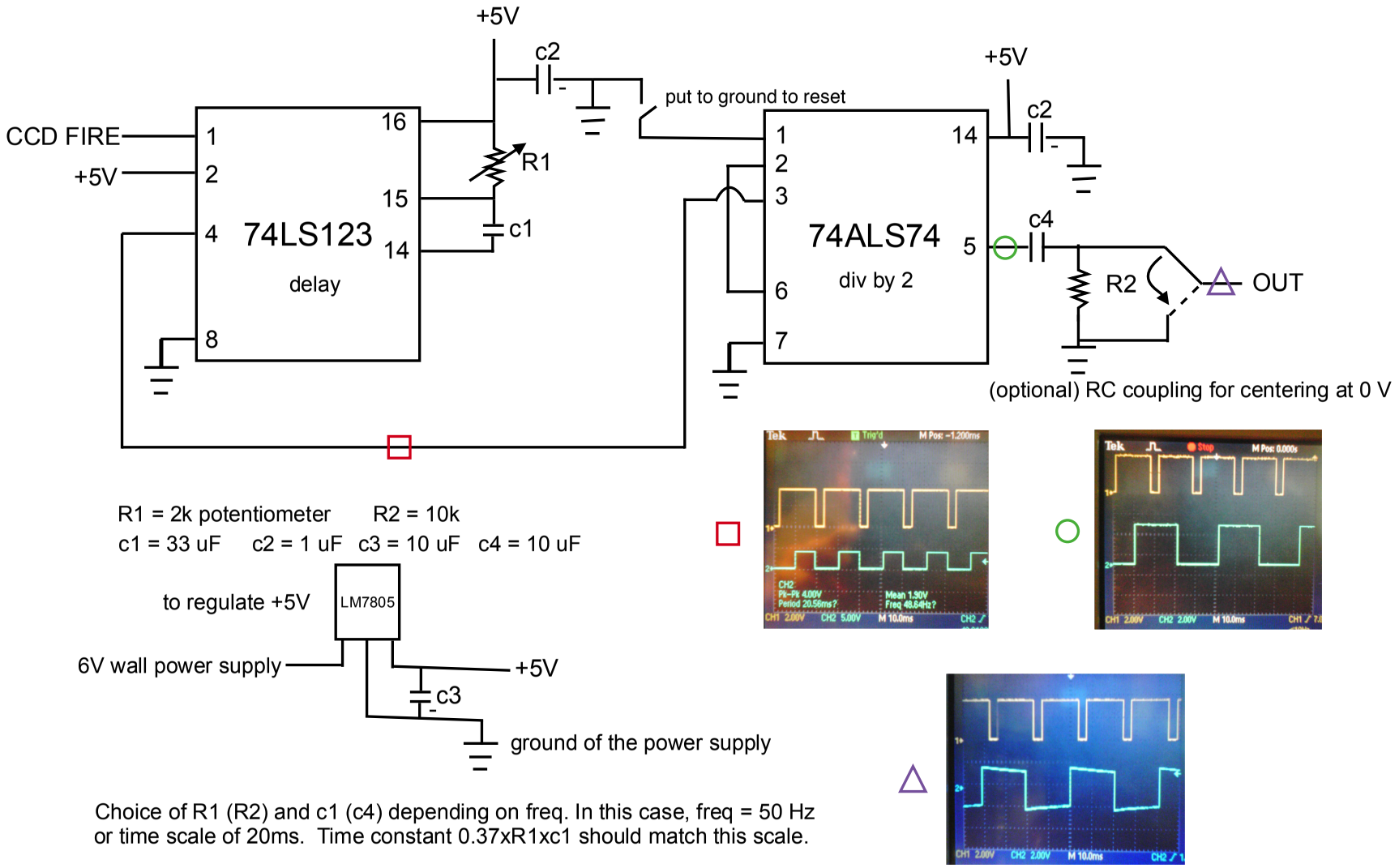

Figure C.2: a control circuit to synchronize the CCD camera (fire Signal) to KEPCO BOP power supply

s